12-2013

Investigation of the One-Probe and Two-Probe Calibration Integral Equation Methods using Experimental Data

Abhay Sanjeev Pande
University of Tennessee - Knoxville, apande@utk.edu

To the Graduate Council:

I am submitting herewith a thesis written by Abhay Sanjeev Pande entitled "Investigation of the One-Probe and Two-Probe Calibration Integral Equation Methods using Experimental Data." I have examined the final electronic copy of this thesis for form and content and recommend that it be accepted in partial fulfillment of the requirements for the degree of Master of Science, with a major in Mechanical Engineering.

Majid Keyhani, Major Professor

We have read this thesis and recommend its acceptance:

Jay I. Frankel, Rao V. Arimilli

Accepted for the Council:
Carolyn R. Hodges

Vice Provost and Dean of the Graduate School

(Original signatures are on file with official student records.)

Investigation of the One-Probe and Two-Probe Calibration Integral Equation Methods using Experimental Data

A Thesis Presented for the

Master of Science

Degree

The University of Tennessee, Knoxville

Abhay Sanjeev Pande

December 2013

ACKNOWLEDGEMENTS

The contributions of several persons have significantly impacted my graduate education. This thesis marks the culmination of all the hard work and unconditional support offered to me by three professors, without whom the last couple of years of my life would not be the same. It is only fitting that Prof. Majid Keyhani, Prof. Jay Frankel and Prof. Rao Arimilli should serve on my committee.

I would first like to thank my thesis advisor, Dr. Keyhani, for his constant encouragement, patience and mentoring. By working under him I learned the valuable lesson that to think 10 minutes before doing for 5 minutes ultimately gets you to your goal faster – slow is fast. He inculcated in me the thinking of a practical experimentalist and a detective who rigorously interrogates experimental data for all possible clues and to gain physical insight. I can confidently say I am a better thinker because of him. I would like to thank my co-advisor, Dr. Frankel, for imparting to me his vast mathematical knowledge and offering help whenever needed. My grasp of graduate level engineering mathematics would be fairly average if not for his creative ideas, tricks and well-designed courses. He taught me it is perfectly okay to think out-of-the-box and to challenge yourself. It is a fact that without the efforts of Dr. Arimilli, I would not have been offered a research assistantship position in the heat transfer laboratory. It was through his courses that my knowledge of thermal sciences was enhanced. I would like to thank him for his valuable advice and constant help that enabled me to proceed with ease in my first year of graduate study.

The success of my experimental work can be largely attributed to the efforts of Mr. Dennis Higdon and Mr. Danny Graham. Without them, experiments would come to a standstill. I would like to thank Dennis for helping with equipment maintenance and troubleshooting. He had an answer for practically anything. I would like to thank Danny for his excellent fabrication skills, generous loans of tools and for his prompt advice and help. I would also like to thank my fellow graduate students, past and present, for their assistance in my work and their friendship. Every day at work was enriched by the company of Jake Plewa, Alex Hashemian, Dominik Bottlaender, Kelsey Winstead, Yinyuan Chen and Hongchu Chen. Sharing thoughts and exchanging ideas with them created a healthy learning atmosphere.

Finally, I would once again like to thank my advisors for funding my work and education via the NASA Co-operative Agreement (EPSCoR-NNX10AN35A) and a GTA position in the final semester of my graduate study.

ABSTRACT

This work aims to expand the applicability of the recently devised physics-based Calibration Integral Equation Method (CIEM) at the University of Tennessee Knoxville, for solving the Inverse Heat Conduction Problem (IHCP) as applied to a one-dimensional domain. Contrary to conventional schemes of solving the IHCP, the CIEM does not require the knowledge of the thermo-physical properties of the domain, sensor characterization and sensor probe locations. The pertinent information is implicitly accounted for via an experimental run. The experimental run 'calibrates' the physics of the domain and is called the 'calibration run'. The net surface heat flux during a real 'unknown' run can then be reconstructed using measured in-depth real run temperature histories in conjunction with the calibration run data. The calibration integral equation(s) is identified as a Volterra integral equation of the first kind, which is well known to be ill-posed. Hence, some form of regularization is required to facilitate a stable resolution. This thesis will explore the operation of the CIEM in two parts, both using experimentally gathered data. The first part will revisit the one-probe CIEM in the light of suggesting an alternate scheme for the selection of the optimum regularization parameter and also extend its applicability to two-layer domains. The proposed scheme requires solely the calibration run temperature history for establishing an optimal band for the selection of the regularization parameter. The one-probe CIEM demands identical back boundary conditions during the calibration and 'real' run stages. This restriction is lifted by means of the two-probe CIEM, which will constitute the second part of this thesis. The two-probe CIEM implicitly registers the effect of the back-boundary condition via a second temperature measurement at a different probe location. This enables the reconstruction of the net surface heat flux during the 'real' run, independent of the 'real' run back-boundary condition. The considerable difficulty of simulating in the laboratory, the actual boundary conditions prevalent in a space vehicle is thus avoided. The two-probe CIEM is also applicable to multi-layer domains. Highly favorable results are presented for both one and two-probe CIEMs applied to single and two-layer domains.

TABLE OF CONTENTS

LIST OF TABLES

LIST OF FIGURES

NOMENCLATURE

a width of first layer, mm

A arbitrary matrix

$A(s)$ coefficient term, ^{o}C

A_H area of nichrome heater, m^2

b thermocouple probe depth, mm

B coefficient term $B(s)$, ^{o}C

C coefficient term $C(s)$, ^{o}C

C_γ denominator term of Eq. (2.13b), ^{o}Cs

D signal $D(\gamma)$, ^{o}C

$D(s)$ coefficient term $D(s)$, ^{o}C

E total energy input, J/cm^2

E_γ predicted total energy input, J/cm^2

E_p predicted total energy input, J/cm^2

f function, $f(t)$

f_s sampling frequency, Hz

$\bar{f}$ vector notation of function $f(t)$

$\hat{f}$ transform of function $f(t)$

g function, $g(t)$

$\hat{g}$ transform of function $g(t)$

h heat transfer coefficient, W/(m^{2}K)

$h(t)$ function

$\hat{h}$ transform of function $h(t)$

j index

k thermal conductivity, W/(mK)

k_1 thermal conductivity of first layer, W/(mK)

k_2 thermal conductivity of second layer, W/(mK)

K kernel function $K(b,t)$, ^{o}C

K kernel function $K(b,w,t)$, ^{o}C^{2}s

K_1 first component of kernel function $K(b,w,t)$, ^{o}C^{2}s

K_2 second component of kernel function $K(b,w,t)$, ^{o}C^{2}s

$\mathcal{K}$ kernel matrix

L width of domain, mm

$\mathcal{L}$ Laplace Transform operator

m number of rows in a matrix

M kernel function, s^{-1}

$\widehat{M}$ transformed kernel function $\widehat{M}(k,\alpha,x,s)$, ^{o}Ccm^2/W

$\widehat{M}$ transformed kernel function $\widehat{M}(x,w,\alpha,k,s)$, s^{-1}

$\widehat{M}$ transformed kernel function $\widehat{M}(k_1,k_2,\alpha_1,\alpha_2,a,b,w;s)$, W/(^{o}Ccm^2)

n number of columns in a matrix

N total number of sample points

N kernel function $N(x,w,k,\alpha,t-u)$, ^{o}Ccm^2/J

$\widehat{N}$ transformed kernel function $\widehat{N}(x,w,\alpha,k,s)$, ^{o}Ccm^2/W

$\widehat{N}$ transformed kernel function $\widehat{N}(k_1,k_2,\alpha_1,\alpha_2,a,b,w;s)$, W/(^{o}Ccm^2)

$\widehat{N}^*$ consolidated transformed kernel function

p truncation index

$q^{"}$ net surface heat flux, W/cm^2

$q_1^{"}$ net surface heat flux into first layer, W/cm^2

$q_2^{"}$ net surface heat flux into second layer, W/cm^2

$q_{cal}^{"}$ measured net surface heat flux during 'calibration' run, W/cm^2

$q_{cal1}^{"}$ measured net surface heat flux during 'calibration' run 1, W/cm^2

$q_{cal2}^{"}$ measured net surface heat flux during 'calibration' run 2, W/cm^2

$q_{max}^{"}$ maximum value of measured net surface heat flux, W/cm^2

$q_{pk1}^{"}$ value at first peak of measured net surface heat flux, W/cm^2

$q_{pk1,p}^{"}$ value at first peak of predicted net surface heat flux, W/cm^2

$q_{pk1,\gamma}^{"}$ value at first peak of predicted net surface heat flux, W/cm^2

$q_{pk2}^{"}$ value at second peak of measured net surface heat flux, W/cm^2

$q_{pk2,p}^{"}$ value at second peak of predicted net surface heat flux, W/cm^2

$q_{pk2,\gamma}^{"}$ value at second peak of predicted net surface heat flux, W/cm^2

$q_{run}^{"}$ measured net surface heat flux during 'real' run, W/cm^2

$q_{run,p}^{"}$ predicted net surface heat flux during 'real' run, W/cm^2

$q_{run,\gamma}^{"}$ predicted net surface heat flux during 'real' run, W/cm^2

$q_s^{"}$ source heat flux, W/cm^2

$\hat{q}^{"}$ transformed net surface heat flux, W/cm^2

$\hat{q}_1^{"}$ transformed net surface heat flux into first layer, W/cm^2

$\hat{q}_2^{"}$ transformed net surface heat flux into second layer, W/cm^2

$\hat{q}''_{cal}$ transformed net surface heat flux during 'calibration' run, W/cm^2

$\hat{q}''_{cal1}$ transformed net surface heat flux during 'calibration' run 1, W/cm^2

$\hat{q}''_{cal2}$ transformed net surface heat flux during 'calibration' run 2, W/cm^2

$\hat{q}''_{run}$ transformed net surface heat flux during 'real' run, W/cm^2

$\bar{q}$ vector notation of net surface heat flux during 'real' run

$\bar{q}_p$ vector notation of predicted net surface heat flux during 'real' run

r dummy time variable, s

$r(t)$ base residual function, J^{o}C/cm^2

r_p local residual function $r_p(t)$, J^{o}C^{2}s/cm^2

R resistance of nichrome heater, Ω

s frequency domain variable, s^{-1}

S diagonal matrix in the SVD of A

S_{new} truncated S matrix

t time, s

t_e effective elliptic time, s

t_{max} maximum data collection time, s

t_{ON} heat activation time, s

t_{OFF} heat deactivation time, s

t_p experimental penetration time, s

t_β time beyond which $d\beta(b,t)/dt > 0 \; \forall \; t$, s

T positional temperature, ^{o}C

T_1 positional temperature in first layer, ^{o}C

T_2 positional temperature in second layer, ^{o}C

T_b measured thermocouple temperature at x=b location, ^{o}C

T_{cal} measured shifted temperature (rise above initial value) during 'calibration' run, ^{o}C

T_{cal1} measured shifted temperature (rise above initial value) during 'calibration' run 1, ^{o}C

T_{cal2} measured shifted temperature (rise above initial value) during 'calibration' run 2, ^{o}C

T_{run} measured shifted temperature (rise above initial value) during 'real' run, ^{o}C

T_{tc} measured thermocouple temperature, ^{o}C

$T_{tc,avg}$ running average of measured thermocouple temperature, ^{o}C

T_o initial temperature, ^{o}C

T_w measured thermocouple temperature at x=w location, ^{o}C

T_∞ ambient temperature, ^{o}C

$\hat{T}$ transformed positional temperature, ^{o}C

$\hat{T}_1$ transformed positional temperature in first layer, ^{o}C

$\hat{T}_2$ transformed positional temperature in second layer, ^{o}C

$\hat{T}_{cal}$ transformed 'calibration' run temperature, ^{o}C

$\hat{T}_{cal1}$ transformed 'calibration' run 1 temperature, ^{o}C

$\hat{T}_{cal2}$ transformed 'calibration' run 2 temperature, ^{o}C

$\hat{T}_{run}$ transformed 'real' run temperature, ^{o}C

u dummy time variable, s

U orthonormal matrix in the SVD of A

U_{new} truncated U matrix

v time variable, s

V orthonormal matrix in the SVD of A

V_{new} truncated V matrix

V_{rms} root mean square voltage, V

w thermocouple probe depth, mm

x spatial variable in the x-direction, mm

y spatial variable in the y-direction, mm

GREEK

α thermal diffusivity, m^2/s

α_1 thermal diffusivity of first layer, m^2/s

α_2 thermal diffusivity of second layer, m^2/s

β function $\beta(b,t)$, ^oCs

γ future-time parameter, s

γ_{max} maximum bound on future time parameter γ , s

γ_{min} minimum bound on future time parameter γ , s

ϵ_q error in prediction, W/cm^2

$\epsilon_{q,heat}$ error in prediction during heating period, W/cm^2

$\varepsilon_{q,p}$ error in prediction, W/cm^2

$\varepsilon_{q,p,heat}$ error in prediction during heating period, W/cm^2

Δt sampling time increment, s

$\Delta t_{pk1,p}$ difference in time of occurrence of first predicted peak and first measured peak, s

$\Delta t_{pk1,\gamma}$ difference in time of occurrence of first predicted peak and first measured peak, s

$\Delta t_{pk2,p}$ difference in time of occurrence of second predicted peak and second measured peak, s

$\Delta t_{pk2,\gamma}$ difference in time of occurrence of second predicted peak and second measured peak, s

λ singular value, s^{-2}

ψ metric $\psi(p)$

σ noise level in measured thermocouple temperature, ^{o}C

σ_b noise level in measured thermocouple temperature at x=b location, ^{o}C

σ_w noise level in measured thermocouple temperature at x=w location, ^{o}C

σ_r standard deviation of local residual function $r_p(t)$, $J^{o}C^{2}s/cm^{2}$

$\sigma_{\epsilon q}$ standard deviation of ϵ_q, W/cm^{2}

$\sigma_{\epsilon q,heat}$ standard deviation of $\epsilon_{q,heat}$, W/cm^{2}

μ arithmetic mean

CHAPTER 1. INTRODUCTION

1.1 PROBLEM STATEMENT

In a conventional (direct) heat conduction problem, the interior temperature distribution of a solid domain is determined with the help of known boundary and initial conditions. This process is well studied and well understood [1-3]. On the other hand, an inverse heat conduction problem (IHCP) utilizes in-depth temperature data to predict the surface (boundary) conditions [1,4]. In certain real-world applications, a harsh thermal environment at the surface renders installation of thermal sensors at the surface infeasible. This necessitates in-depth placement of the sensors. Such a scenario is often encountered in the study of hyper-sonics, where both internal and external flows can cause extreme surface thermal conditions.

The IHCP is inherently ill-posed in that relatively small errors in the measured in-depth data can produce substantial errors in the surface prediction. An ill-posed problem does not satisfy Hadamard's three conditions for well posedness [5]. In the past two years, a new methodology based on the integration of mathematical reasoning and experimental design has produced an alternative framework for studying inverse problems [6-10]. The novel physics-based calibration approach of solving the IHCP can be divided into two categories; 1) One-probe calibration and 2) Two-probe calibration. The one-probe calibration method is applicable exclusively to situations where the back-boundary conditions during the 'calibration run (known)' and the 'real run (unknown)' are identical. This method has been discussed and tested with both simulated and experimental data [6,7,9]. The two-probe calibration method is applicable to more general scenarios wherein no restrictions are imposed on the nature of the back-boundary condition during the 'real' run. The introduction to the two-probe calibration method, accompanied with test scenarios implementing simulated data is presented in an internal technical note [10], which is under development for eventual publication. Both the calibration methods (one-probe and two-probe) require some form of regularization to obtain a stable reconstruction of the surface heat flux.

1.2 SCOPE OF THESIS

The Inverse Heat Conduction Problem (IHCP) studied in this thesis will be posed for the domains shown in Figure 1.1.

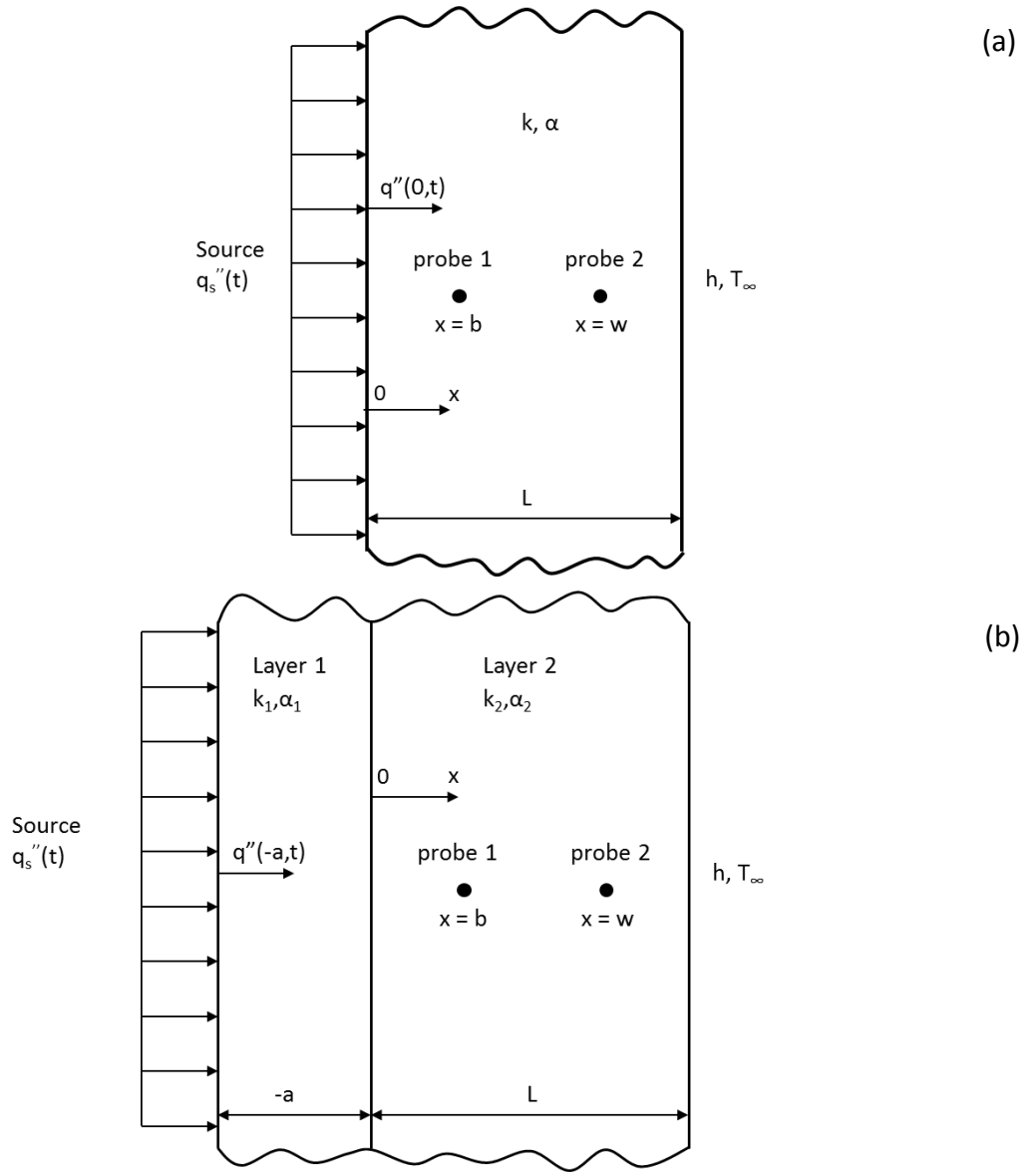

Figure 1.1. Schematic of a one-dimensional domain with in-depth thermocouples for (a) one layer, with the goal of acquiring q"(0,t) and (b) two layer, with the goal of acquiring q"(-a,t).

The analysis will be limited to one-dimensional heat transfer along the x- direction. The assumption of constant thermo-physical properties (k,α) is made. The front surface is subjected to a transient source heat flux $q_s^{"}(t)$ with a spatially uniform profile. A convective boundary condition is shown at the back surface where h is the convective heat transfer coefficient and T_∞ is the ambient temperature. Figure 1.1(a) shows a single layer domain. The objective is to reconstruct the net surface heat flux q"(0,t) entering the domain with the help of measured in-depth thermocouple data. For the two-layer domain shown in Figure 1.1(b) the net surface heat flux being sought enters the domain at the first layer, of thickness x = a, and is hence denoted as q"(-a,t). Each layer has its own set of thermo-physical properties. The reconstruction of the net surface heat flux is achieved via the Calibration Integral Equation Method (CIEM), developed by Frankel et al. [6,8,10], and will be shown to apply to both single layer and two-layer domains.

The One-probe Calibration Integral Equation Method utilizes temperature data from a single probe (at x=b) for surface projection. As mentioned before, this method has been demonstrated and analyzed using both simulated and experimental data [6,7,9]. The first goal of this thesis is to introduce a new regularization scheme, as an alternative to the schemes implemented in [6,7,9]. A modified approach will be suggested, where an optimum 'band' instead of an optimum 'value' for the regularization parameter is established. An important operating constraint of the one-probe method is that the back-boundary conditions during the calibration and real runs must be identical. This has practical limitations in that it would pose significant difficulty in reproducing in the laboratory, the actual back-boundary condition prevalent inside a space vehicle. This problem is resolved by the Two-probe Calibration Integral Equation Method. As the name suggests, this is achieved by the inclusion of the second thermocouple (at x=w) in the formulation. It will be explained that the w probe registers the effect of the back-boundary condition and makes the method independent of the real (unknown) run back boundary condition. The second goal of this thesis is to demonstrate the successful implementation of the two-probe calibration integral equation method using experimental data.

Chapter 2 will introduce the reader to the concept of the calibration integral equation method of resolving the IHCP. The governing equations and associated regularization schemes used will be explained. This chapter will review the pertinent background information and mathematical framework required for this thesis. The construction and working of the experimental setup utilized for data collection will be described in Chapter 3. The selected experimental data sets considered for analysis will also be presented in Chapter 3. Demonstration of the One-probe and Two-probe CIEMs using the selected experimental data will constitute Chapter 4. The

results obtained will be analyzed and discussed in detail. Finally, Chapter 5 will summarize the findings of Chapter 4 and offer recommendations and suggestions for future work in the physics-based calibration method of resolving the IHCP.

1.3 LITERATURE REVIEW

The discipline of the Inverse Heat Conduction Problem (IHCP) gained considerable importance nearly sixty years ago. In the first commercially published work on the topic [1], Beck credits the aerospace industry and mainly the space program that started about 1956, for giving impetus to the study of the inverse heat conduction problem. This yielded some of the earliest publications on the subject by Stolz [11] in 1960, Mirsepassi [12,13] in 1959 and a translation of a Russian paper by Shumakov [14] in 1957. Stolz's paper addressed the calculation of heat transfer rates during quenching of bodies of simple finite shapes. It involved the numerical solution of a first kind Volterra integral equation. However, the time-marching algorithm required relatively large time steps to maintain stability. For semi-infinite geometries Mirsepassi claimed the employment of the same technique both numerically [12] and graphically [13] for several years prior to 1960. Much of the work during this period had aerospace applications related to nose cones of missiles and probes, rocket nozzles and other devices.

Advancement in research dealing with the IHCP can be primarily attributed to the work of Beck and his colleagues. His landmark publication [15] in 1970 helped the development of many of the early computer programs for resolving the IHCP. His work strongly influenced the future time and function specification methods.

Contemporary research on the IHCP relies on numerous solution techniques. Explicit analytical methods are limited to simple geometries and have limited practical use. However, exact solutions can give considerable insight into the understanding of the basic properties and characteristics of IHCPs. They can also serve as benchmarks for evaluating the performance of approximate methods.

Monde [16] developed an analytical method for both one-dimensional and two-dimensional inverse heat conduction problems using the Laplace transform technique. For a 1-Dimensional boundary value inverse problem defined for a flat slab, sphere or cylinder, Burggraf [17] found an exact solution with the knowledge of the heat flux and the time dependent temperature response at one interior location. The solution is presented in the form of an infinite series. A special advantage of this method is that no initial condition is required to determine the solution. This follows from the assumption that the known interior heat flux and temperature histories are available for infinite time. On the downside, the method also requires higher time

derivatives of the heat flux and temperature histories. The number of derivatives needed is decided by the number of terms retained in the truncated series. Differentiation of noisy measured data invariably results in a highly unstable prediction.

Resolving the IHCP via numerical methods involves iterative schemes, sequential schemes or whole domain schemes wherein the entire time domain is solved for simultaneously. Sequential schemes are known to be computationally efficient whereas iterative and whole domain methods typically require substantial memory and processing power. Some of the important numerical methods will now be described in brief.

Perhaps the most common and well known of regularizing schemes is the classical Tikhonov regularization method. The method involves the minimization of a functional which takes the form of the sum of the original ill-posed problem with an additional 'penalty term'. The penalty term comprises of a "regularization parameter" with a semi-norm involving some function. Often this semi-norm involves the heat flux [18]. The regularization parameter does not have a clear physical interpretation which makes its determination difficult. The maximum likelihood method [19], Morozov's discrepancy principle [19,20] and estimation via the L-curve method [21,22] are some of the approaches used in the determination of the regularization parameter. However, finding the suitable Tikhonov regularization parameter is still under intensive research.

In the function specification method [1], the transient surface heat flux with time is assumed to be of a functional form. The regularization parameter in this approach involves specifying the number of future time steps required for stabilizing the approximation. The function specification method is computationally efficient since it is sequential in time. The difficulty of this method lies in defining the number of future time steps since it depends on the unknown surface heat flux.

One-dimensional space marching methods use either an implicit or explicit temporal formulation [1,23,24]. Space marching is essentially a finite difference scheme where one spatial node can be solved for directly using the known conditions. This node's solution is then used to solve the next node and so on. Two temperature sensors are commonly assumed as the known boundary data. The implicit finite difference scheme is sensitive to high frequency measurement error. Various schemes have been used to damp out any noise in the data, which involve the use of temperature data from future times [1].

The conjugate gradient method is a straightforward and powerful iterative technique for solving linear and non-linear inverse problems of parameter estimation. The conjugate gradient

method with the adjoint problem has also been widely used to resolve IHCP's. Zhou et al. [25] studied the one-sided inverse heat conduction problem where both the temperature and heat flux are specified at the back boundary. The temperature data are used as back surface boundary condition and the heat flux is adopted as the objective function to be minimized. The IHCP formulation was shown to possess good stability in the parameter range considered in that study. However, the conjugate gradient method is computationally expensive and requires a large amount of memory. The Levenberg Marquardt Method [4] is closely akin to the conjugate gradient method in that the first two steps (the direct problem and the inverse problem) in the solution procedure are common. This method was originally devised for application to non-linear parameter estimation problems but has also been successfully applied to the solution of linear ill-conditioned problems.

Elkins et al. [26] presented a global time and discrete space formulation of an IHCP. Instead of using a finite difference representation for the time derivatives of the measured temperature data, the heating rate and higher time derivatives are directly measured by a rate-based sensor. The rate-based sensor concept involves analog filtering where the filter cut-off frequency is the regularization parameter. A Gauss low-pass filter [27] with a physically based cut-off frequency is used for regularization in resolving the null point equation associate with arc-jet testing. The Gauss filter maintains smoothness in higher time derivatives unlike most low pass digital filters. The special feature of the global time method lies in its accuracy to predict the surface heat flux as the sampling rate increases, in contrast to many conventional inverse methods.

Singular-value decomposition is another approach used in resolving IHCP's based on matrix manipulations. The ill-conditioned matrix is decomposed into two orthonormal matrices and a diagonal matrix that contains its singular values in descending order. The rate of decrease in the singular values along the diagonal determines the level of ill-conditioning [28-30]. The singular values of negligible magnitude are set to zero in order to recondition the matrix. The action of reconditioning is analogous to digital filtering in the removal of noise. Shenefelt et al. [31] utilized the singular value decomposition approach for reconditioning the kernel matrix to ultimately find its pseudo inverse for solving a linear system of equations. The solution to these equations was the reconstruction of the surface heating condition.

Calibration is a novel approach to resolve the inverse heat conduction problems. The Non Integer System Identification (NISI) method [32,33] is a calibration method that requires an accurate extraction of the impulse function based on the fractional derivative formulation of the heat equation. A known net surface source is first used as a calibration source to get the relationship between net surface heat flux and temperature response at the sensor site. The

sensor characteristics, depth of sensor, and thermophysical properties of the host material are accounted in the calibration coefficients that are determined by a least squares method. The unknown surface heat flux can be estimated by the corresponding sensor response and the calibration coefficients. Nevertheless, the NISI method is limited to one-dimensional, semi-infinite cases involving isotropic materials with constant properties.

In all previous methods noted in this chapter, with exception to the NISI method, thermo-physical properties require specification and should be accurately known. Probe positioning and attachment to the host material must be accurately portrayed and quantified. The physics-based calibration methodology proposed by Frankel et al. [6,8,10], inherently contains sensor positioning, sensor characteristics and thermo-physical properties of the host material in the final mathematical expression that relates the in-depth measured temperature data to the surface heat flux. This thesis aims to improve on the previously published work on the one-probe calibration methodology and also to provide experimental validation of the new two-probe calibration method of resolving the IHCP.

CHAPTER 2. THE CALIBRATION INTEGRAL EQUATION METHOD

This chapter will serve to establish the necessary background needed to understand the concept of the Calibration Integral Equation Method (CIEM). The motivation behind the conception of this novel method will be explained. The concept of reconstructing the surface heat flux through 'physics-based calibration' originated with the exact solution to the heat equation in a half-space depicted in Figure 2.1.

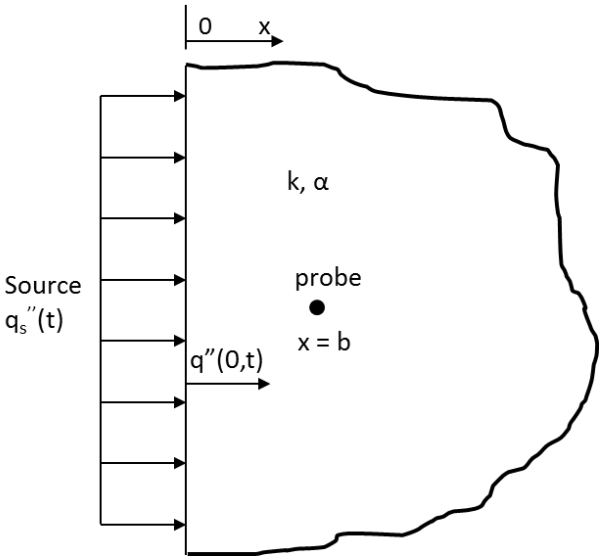

Figure 2.1. Schematic of a semi-infinite domain. A thermocouple (probe) is located at x = b. The net heat flux into the domain is given by q"(0,t).

The heat equation for one dimensional, linear transient conduction heat transfer for the domain shown in Figure 2.1 is

$$\frac{1}{\alpha}\frac{\partial T}{\partial t}(x,t) = \frac{\partial^2 T}{\partial x^2}(x,t), \quad (x,t) \geq 0, \tag{2.1}$$

subject to the boundary and initial conditions

$$q''(0,t) = -k\frac{\partial T}{\partial x}(0,t), \quad t > 0, \tag{2.2a}$$

$$\lim_{x\to\infty} T(x,t) = T_o, \quad t > 0, \tag{2.2b}$$

$$T(x,0) = T_o,\ x \geq 0, \tag{2.2c}$$

where k is the thermcal conductivity and α is the thermal diffusivity of the domain. Without loss of generality and for simplicity, we let $T_o = 0$. The exact solution can then be expressed as

$$T(x,t) = \sqrt{\frac{\alpha}{\pi k^2}} \int_{u=0}^{t} q^{"}(0,u) \frac{e^{-\frac{x^2}{4\alpha(t-u)}}}{\sqrt{t-u}} du, \qquad (x,t) \geq 0. \tag{2.3}$$

It was noticed in [6] that Eq. (2.3) contains a convolution kernel (t-u), suggesting the use of the Laplace Transform for gaining new insight into its behavior. The Laplace Transform $\mathcal{L}$ placed Eq. (2.3) in the frequency domain to take on a very simple form given by

$$\frac{\hat{T}(x,s)}{\hat{q}^{"}(0,s)} = \widehat{M}(k,\alpha,x,s), \qquad s \geq 0, \tag{2.4a}$$

where s is the frequency domain variable and $\hat{T}(x,s)$ and $\hat{q}^{"}(0,s)$ are the transformed positional temperature and net surface heat flux respectively. The kernel $\widehat{M}(k,\alpha,x,s)$ is given by

$$\widehat{M}(k,\alpha,x,s) = \sqrt{\frac{\alpha}{\pi k^2}} \mathcal{L}\left(\frac{e^{-\frac{x^2}{4\alpha(t)}}}{\sqrt{t}} \right), \qquad s \geq 0. \tag{2.4b}$$

Notice that the kernel has not been converted into its corresponding frequency domain expression, and is expressed by keeping the Laplace Transform operator $\mathcal{L}$ intact. Complex expressions in the frequency domain are often encountered wherein the inversion formula is not readily available in mathematical handbooks. However, thinking as a practical experimentalist, this difficulty can be bypassed with the realization that the kernel $\widehat{M}(k,\alpha,x,s)$ does not change for a fixed domain. This can be shown by evaluating Eq. (2.4a) at the probe location (x=b), where the net heat flux $q^{"}(0,t)$ and the in-depth temperature history are measured through an experimental run. Let us call this run as the 'calibration run' and denote the dependent variables with the subscript 'cal'. Doing so yields

$$\frac{\hat{T}_{cal}(b,s)}{\hat{q}^{"}_{cal}(0,s)} = \widehat{M}(k,\alpha,b,s), \qquad s \geq 0. \tag{2.5a}$$

Then a 'real' run is performed assuming that $q^{"}(0,t)$ needs to be resolved. Using subscript 'run' for the second run, we obtain

$$\frac{\hat{T}_{run}(b,s)}{\hat{q}^{"}_{run}(0,s)} = \widehat{M}(k,\alpha,b,s), \qquad s \geq 0. \tag{2.5b}$$

It is observed that the kernel $\widehat{M}(k,\alpha,b,s)$ remains unchanged and carries the heat equation physics, thermo-physical properties and the probe position. The result implicitly contains the heat equation that has been re-expressed in terms of the calibration run. In essence, the physics of the domain have been 'calibrated' by the calibration run. Therefore, the inversion of $\widehat{M}(k,\alpha,b,s)$ to the time domain can be bypassed by equating Eq. (2.5a) with Eq. (2.5b) to give

$$\frac{\hat{T}_{cal}(b,s)}{\hat{q}^{"}_{cal}(0,s)} = \frac{\hat{T}_{run}(b,s)}{\hat{q}^{"}_{run}(0,s)}, \qquad s \geq 0. \tag{2.6}$$

The only unknown in Eq. (2.6) is the desired net surface heat flux $\hat{q}^{"}_{run}(0,s)$ albeit in the frequency domain. Cross-multiplying Eq. (2.6) presents the final expression in the frequency domain, Eq. (2.7), in a format that can be readily inverted back to the time domain.

$$\hat{q}^{"}_{run}(0,s)\hat{T}_{cal}(b,s) = \hat{q}^{"}_{cal}(0,s)\hat{T}_{run}(b,s), \;\; s \geq 0. \tag{2.7}$$

Equation (2.7) is comprised of two terms, each being a product of two functions of the frequency variable 's'. Hence, by application of the inverse Laplace convolution theorem to Eq. (2.7) we arrive at the novel Volterra integral equation of the first kind [34] given as

$$\int_{u=0}^{t} q^{"}_{run}(0,u)T_{cal}(b,t-u)du = \int_{u=0}^{t} q^{"}_{cal}(0,u)T_{run}(b,t-u)du, \qquad t \geq 0, \tag{2.8a}$$

or in a more conventional form as

$$\int_{u=0}^{t} q^{"}_{run}(0,u)K(b,t-u)du = f(t), \qquad t \geq 0, \tag{2.8b}$$

where

$$f(t) = \int_{u=0}^{t} q''_{cal}(0,u)T_{run}(b,t-u)du, \qquad t \geq 0, \tag{2.8c}$$

and

$$K(b,t-u) = T_{cal}(b,t-u), \qquad t-u \geq 0. \tag{2.8d}$$

Equation (2.8a) presents the conventional linear one-probe calibration integral equation. It was derived through a rather unconventional approach in that the analysis started with an exact solution. However, derivation from first principles yields the same result as demonstrated in [9]. It is important to note that the temperatures in Eq. (2.8a) are assumed to be positional temperatures, which do not account for the delay and attenuation observed in thermocouple measurements. Using a first order thermocouple model for relating the positional temperature $T(b,t)$to the measured temperature $T_{tc}(b,t)$ [6], it was shown that the form of Eq. (2.8a) was maintained even when measured thermocouple temperature histories were used directly. Frankel et al. [6] demonstrated the working of the one-probe method using simulated data. It was also shown in [6] that Eq. (2.8a) was applicable to a two-layer semi-infinite domain but with a slight notational change as

$$\int_{u=0}^{t} q''_{run}(-a,u)T_{cal}(b,t-u)du = \int_{u=0}^{t} q''_{cal}(-a,u)T_{run}(b,t-u)du, \qquad t \geq 0, \tag{2.9}$$

where x = 0 is located at the interface of the two layers, and a is the thickness of the first layer which is subjected to the heat flux boundary condition (see Figure 1.1(b)). Equation (2.9) defaults to the conventional single-layer equation, as per Eq. (2.8a), when $a = 0$. In the companion work to [6], Elkins et al. [7] validated the conventional (single-layer) concept by using experimentally gathered data. Chen [9] demonstrated that Eq. (2.8a) was applicable even for a finite width domain subjected to a convection boundary condition at the back surface.

It is well known that Volterra integral equations of the first kind are ill-posed and need some form of regularization for their stable resolution [34]. In all of these past studies [6-9] on the one-probe calibration integral equation method, a simplified variation of Lamm's local future time regularization scheme [35] was utilized for inverse prediction of the net surface heat flux. Incorporation of the regularization model recast the original ill-posed Volterra integral equation of the first kind, Eq. (2.8a), into the well-posed second kind equation. This was achieved at the cost of alteration of the original physics by the regularization model. The steps taken in the regularization scheme will now be explained in brief. For complete details on the

implementation of the future time regularization scheme, the reader is directed to Refs. [6,7,9]. Regularization is carried out by advancing the time through $t \rightarrow t+\gamma$ where γ is the future time regularization parameter. Applying this to the compact form of the one-probe calibration integral equation given by Eq. (2.8b), yields

$$\int_{u=0}^{t+\gamma} q_{run}^{"}(0,u)K(b,t+\gamma-u)du = f(t+\gamma), \qquad t \in [0, t_{max}-\gamma], \tag{2.10}$$

where t_{max} is the maximum time period for data collection. Observe that the time domain has been reduced by γ seconds. This means that $q_{run}^{"}(0,t)$cannot be resolved for the final γ seconds. By splitting the limits of integration in Eq. (2.10) we arrive at

$$\int_{u=0}^{t} q_{run}^{"}(0,u)K(b,t+\gamma-u)du + \int_{u=t}^{t+\gamma} q_{run}^{"}(0,u)K(b,t+\gamma-u)du = f(t+\gamma), \tag{2.11}$$
$$t \in [0, t_{max}-\gamma].$$

For a sufficiently small value of γ, the unknown heat flux is approximated to be a constant depending on the value of γ. This allows the second term in the LHS of Eq. (2.11) to be re-expressed to get

$$\int_{u=0}^{t} q_{run,\gamma}^{"}(0,u)K(b,t+\gamma-u)du + q_{run,\gamma}^{"}(0,t)\int_{u=t}^{t+\gamma} K(b,t+\gamma-u)du = f(t+\gamma), \tag{2.12}$$
$$t \in [0, t_{max}-\gamma].$$

Notice that $q_{run,\gamma}^{"}(0,t)$ is an approximation to $q_{run}^{"}(0,t)$and allows the equality of Eq. (2.12) to hold. Introducing a change of variables by defining $v = t-u$, it is revealed that the integral in the second term in the LHS of Eq. (2.12) evaluates to a constant C_γ for the specified value of γ as per

$$\int_{u=0}^{t} q_{run,\gamma}^{"}(0,u)K(b,t+\gamma-u)du + q_{run,\gamma}^{"}(0,t)\,C_\gamma = f(t+\gamma), \qquad t \in [0, t_{max}-\gamma], \tag{2.13a}$$

where

$$C_\gamma = \int_{v=0}^{\gamma} K(b, \gamma - v)dv = \int_{v=0}^{\gamma} T_{cal}(b, \gamma - v)dv. \tag{2.13b}$$

Equation (2.13a) is now in the standard form of a Volterra integral equation of the second kind [44]. The influence of the regularization model is reflected in the notation $q^{"}_{run,\gamma}(0,t)$ which is an approximation to $q^{"}_{run}(0,t)$. The final expression for the unknown net surface heat flux $q^{"}_{run,\gamma}(0,t)$can be arrived at by re-arranging Eq. (2.13a) to get

$$q^{"}_{run,\gamma}(0,t) = \frac{1}{C_\gamma}\left[f(t+\gamma) - \int_{u=0}^{t} q^{"}_{run,\gamma}(0,u)T_{cal}(b, t+\gamma-u)du\right], \tag{2.14}$$

$$t \in [0, t_{max} - \gamma].$$

To improve clarity $K(b,\gamma - v)$ has been replaced by $T_{cal}(b,\gamma - v)$, as per Eq. (2.8d). It is important to note that all the terms appearing in Eq. (2.14) are, in practice, experimental data streams sampled at discrete instances in time. The discretization process imposes an additional approximation to $q^{"}_{run}(0,t)$. Assuming data are sampled for a total N instances in time at a sampling frequency f_s, $q^{"}_{run,\gamma}(0,t)$ is available only for the time set $\{t_j\}_{j=1}^{N-\gamma f_s}$ and is approximated as $q^{"}_{run,\gamma}(0,t_j)$. This notation carries relevance when a comparison is needed between discrete and continuous (if available) data. Throughout this presentation, analysis will be carried out using solely experimental data of a finite size. Therefore, for convenience in notation, the original notation as per Eq. (2.14) will be retained. Finally, the choice of the regularization parameter γ is made using various techniques, as discussed in [6,7,9]. A new modified scheme for choosing an 'optimal range' for γ will be suggested in Chapter 4 of this thesis.

The need for the two-probe calibration integral equation method arises due to a significant operating constraint imposed by the one-probe calibration integral equation method. This constraint is brought to light during the derivation from first principles of the one-probe calibration integral equation method, presented in [9]. From Ref. [9], consider Eq. (3.9b) on page 10 now restated as

$$\frac{\hat{q}^{"}(0,s)}{\hat{T}(b,s)} = \hat{N}(b,L,k,\alpha,h,s), \qquad s \geq 0. \tag{2.15}$$

Similar in format to the equivalent expression presented earlier in Eq. (2.4a), the kernel $\widehat{N}(b, L, k, \alpha, h, s)$ now carries extra information pertaining to the convective boundary condition specified at the back surface of the finite slab of width L. The central idea behind the formulation of the one-probe calibration integral equation methodology lies in the assumption that the kernel $\widehat{N}(b, L, k, \alpha, h, s)$ remain constant for a fixed domain. When derived for a half-space domain, this condition was automatically met, making its assumption moot. However, we can observe from Eq. (2.15) that for a finite width domain, in order to progress with the elimination of $\widehat{N}(b, L, k, \alpha, h, s)$ via a calibration run, it must be assumed that the heat transfer coefficient h remains identical during both the calibration and real run cases. Herein lies the important restriction imposed by the one-probe calibration method, that the back-boundary condition must not change between the calibration and real runs. The implications of this constraint become evident when the real run data (comprised of the measured temperature history $T_{run}(b, t)$) are affected by the boundary conditions prevalent inside the space vehicle, whereas the calibration run is performed in a laboratory environment. It is easy to appreciate the practical difficulties involved in reconciling the two back boundary conditions.

As a solution to this problem, the two-probe calibration integral equation method was developed [10]. As the name suggests, temperature measured by a second probe is included in the methodolgy. Consider a finite width domain instrumented with two temperature probes (thermocouples) located at x = b and x = w depths, as shown in Figure 2.2.

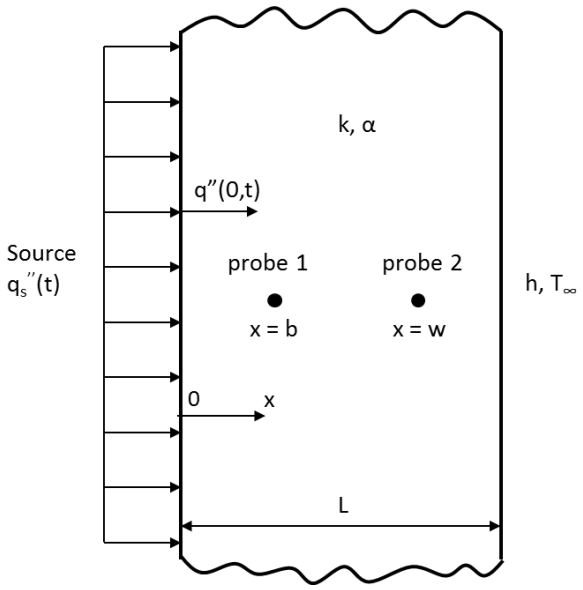

Figure 2.2. Schematic of a finite domain of width L. Thermocouple probes are located at depths x=b and x=w. The net heat flux into the domain is given by q"(0,t).

The linear transient heat conduction equation for this domain is given as

$$\frac{1}{\alpha}\frac{\partial T}{\partial t}(x,t) = \frac{\partial^2 T}{\partial x^2}(x,t), \quad x \in [0,L], t \geq 0, \tag{2.16a}$$

subject to the surface boundary condition

$$q^{"}(0,t) = -k\frac{\partial T}{\partial x}(0,t), \quad t > 0, \tag{2.16b}$$

the initial condition

$$T(x,0) = T_o, \qquad x \in [0,L], \tag{2.16c}$$

and known temperature measurements at the two in-depth locations

$$T(b,t) = T_b(t), \tag{2.16d}$$
$$T(w,t) = T_w(t), \qquad t \geq 0. \tag{2.16e}$$

Again, without the loss of generality and for simplicity, we let $T_o = 0$.

The exact solution to Eq. (2.16a) subjected to the boundary conditions Eq. (2.16b) and Eq. (2.16e), can be determined and is explicitly presented as Eq. (16b) on page 7 of Ref. [10]. The important expression to be considered is Eq. (17a), also on page 7 of Ref. [10], which is now restated as

$$T(x,t) = \int_{u=0}^{t} N(x,w,k,\alpha,t-u)q^{"}(0,u)du + \int_{u=0}^{t} M(x,w,k,\alpha,t-u)T(w,u)du, \qquad x \in [0,L], t \geq 0, \tag{2.17}$$

where the kernels $N(x,w,k,\alpha,t-u)$ and $M(x,w,k,\alpha,t-u)$ are defined by Eq. (17a) and Eq (17b) respectively in [10]. The compact form of Eq. (2.17) is arrived at by noticing a convolution time character in the exact solution, as with the one-probe derivation presented before, and after grouping of similar terms. Again, taking the Laplace Transform of Eq. (2.17) yields

$$\hat{T}(x,s) = \hat{N}(x,w,k,\alpha,s)\hat{q}^{"}(0,s) + \hat{M}(x,w,k,\alpha,s)\hat{T}(w,s), \qquad s \geq 0. \tag{2.18a}$$

Evaluating Eq. (2.18a) at the probe site x = b, we obtain

$$\hat{T}(b,s) = \hat{N}(b,w,k,\alpha,s)\hat{q}^{"}(0,s) + \hat{M}(b,w,k,\alpha,s)\hat{T}(w,s), \quad s \geq 0. \tag{2.18b}$$

Unlike the one-probe derivation, two kernel functions $\hat{N}(b,w,k,\alpha,s)$ and $\hat{M}(b,w,k,\alpha,s)$ now appear. This implies that two calibration runs will be needed to produce two equations for eliminating the two unknown kernel functions. The equations for the two calibrations runs denoted with subscripts 'cal1' and 'cal2' for calibration runs 1 and 2 are

$$\hat{T}_{cal1}(b,s) = \hat{N}(b,w,k,\alpha,s)\hat{q}^{"}_{cal1}(0,s) + \hat{M}(b,w,k,\alpha,s)\hat{T}_{cal1}(w,s), \tag{2.19b}$$

$$\hat{T}_{cal2}(b,s) = \hat{N}(b,w,k,\alpha,s)\hat{q}^{"}_{cal2}(0,s) + \hat{M}(b,w,k,\alpha,s)\hat{T}_{cal2}(w,s), \qquad s \geq 0. \tag{2.19a}$$

Again, the kernel functions implicitly carry the physics of diffusion, thermo-physical properties of the finite domain and the probe locations. Equations (2.19a,b) can be readily solved for the unknown kernel functions in terms of the measured calibration heat fluxes and probe temperatures as

$$\hat{N}(b,w,k,\alpha,s) = \frac{\hat{T}_{cal2}(b,s)\hat{T}_{cal1}(w,s) - \hat{T}_{cal1}(b,s)\hat{T}_{cal2}(w,s)}{\hat{q}^{"}_{cal2}(0,s)\hat{T}_{cal1}(w,s) - \hat{q}^{"}_{cal1}(0,s)\hat{T}_{cal2}(w,s)}, \tag{2.20a}$$

$$\hat{M}(b,w,k,\alpha,s) = \frac{\hat{T}_{cal1}(b,s)\hat{q}^{"}_{cal2}(0,s) - \hat{T}_{cal2}(b,s)\hat{q}^{"}_{cal1}(0,s)}{\hat{q}^{"}_{cal2}(0,s)\hat{T}_{cal1}(w,s) - \hat{q}^{"}_{cal1}(0,s)\hat{T}_{cal2}(w,s)}. \tag{2.20b}$$

The final expression in the frequency domain is arrived at by first restating Eq. (2.18b) for a third 'real' run denoted with subscript 'run', substituting for the kernel functions given by Eqs. (2.20a,b) and re-arranging the resulting terms to obtain

$$\begin{aligned} &\left[\hat{T}_{cal2}(b,s)\hat{T}_{cal1}(w,s) - \hat{T}_{cal1}(b,s)\hat{T}_{cal2}(w,s)\right]\hat{q}^{"}_{run}(0,s) \\ &= \left[\hat{q}^{"}_{cal2}(0,s)\hat{T}_{cal1}(w,s) - \hat{q}^{"}_{cal1}(0,s)\hat{T}_{cal2}(w,s)\right]\hat{T}_{run}(b,s) \\ &- \left[\hat{q}^{"}_{cal2}(0,s)\hat{T}_{cal1}(b,s) - \hat{q}^{"}_{cal1}(0,s)\hat{T}_{cal2}(b,s)\right]\hat{T}_{run}(w,s), \qquad s \geq 0. \end{aligned} \tag{2.21}$$

Equation (2.21) contains arrangements of three term convolution patterns and can be readily inverted to the time domain via the inverse Laplace three-term convolution theorem given by

Eq. (A.3c) in Appendix A. The final version of the two-probe calibration integral equation is presented as

$$\int_{u=0}^{t} q_{run}^{"}(0,u) \int_{r=0}^{t-u} [T_{cal1}(w,r)T_{cal2}(b,t-u-r) - T_{cal2}(w,r)T_{cal1}(b,t-u-r)]\, drdu$$

$$= \int_{u=0}^{t} T_{run}(b,u) \int_{r=0}^{t-u} \left[q_{cal2}^{"}(0,r)T_{cal1}(w,t-u-r) - q_{cal1}^{"}(0,r)T_{cal2}(w,t-u-r)\right] drdu$$

$$- \int_{u=0}^{t} T_{run}(w,u) \int_{r=0}^{t-u} \left[q_{cal2}^{"}(0,r)T_{cal1}(b,t-u-r) - q_{cal1}^{"}(0,r)T_{cal2}(b,t-u-r)\right] drdu,$$

$$t \geq 0. \tag{2.22}$$

Equation (2.22) states the novel two-probe calibration integral equation in its fully explicit form. It was developed as the result of a novel transformative inverse heat conduction methodology based on calibration and frequency domain analysis. In compact notation, it can expressed as

$$\int_{u=0}^{t} q_{run}^{"}(0,u)\, K(b,w,t-u)du = f(t), \qquad t \geq 0, \tag{2.23a}$$

where

$$K(b,w,t-u) = \int_{r=0}^{t-u} [T_{cal1}(w,r)T_{cal2}(b,t-u-r) - T_{cal2}(w,r)T_{cal1}(b,t-u-r)]\, dr, \tag{2.23b}$$

and

$$f(t) = \int_{u=0}^{t} T_{run}(b,u) \int_{r=0}^{t-u} \left[q_{cal2}^{"}(0,r)T_{cal1}(w,t-u-r) - q_{cal1}^{"}(0,r)T_{cal2}(w,t-u-r)\right] drdu$$

$$- \int_{u=0}^{t} T_{run}(w,u) \int_{r=0}^{t-u} \left[q_{cal2}^{"}(0,r)T_{cal1}(b,t-u-r) - q_{cal1}^{"}(0,r)T_{cal2}(b,t-u-r)\right] drdu,$$

$$t \geq 0. \tag{2.23c}$$

Equation (2.23a) again can be identified as a Volterra integral equation of the first kind and requires regularization for a stable resolution of the net surface heat flux.

The two-probe calibration integral equation can be readily extended to a two-layer domain. The final form of the equation is maintained with a slight change in notation wherein the net surface heat flux being sought is denoted by $q''_{run}(-a,t)$, where a is the thickness of the first layer subjected to surface heating. A full detailed derivation of the two-probe two-layer calibration integral equation is presented in Appendix A.

Recall that the motive behind the development of the two-probe calibration integral equation was to address the issue of different back-boundary conditions during the calibration and real run stages. This objective is fulfilled by means of a new operating constraint imposed by the two-probe method. The new constraint requires the two calibration runs to be designed such that the back-boundary conditions between the two runs are dissimilar. If not, the kernel $K(b,w,t-u)$, as per Eq. (2.23b), will identically be equal to zero and no solution will be possible. In fact, it will be explained later in Chapter 4 that the larger the difference between back-boundary conditions, the more favorable is the outcome. The requirement that the back-boundary conditions be different during the calibration process, automatically makes the method independent of the back-boundary condition during the real run. The concept of the 'effective elliptic time t_e' will be introduced and will serve as a good measure of assessing the strength of the kernel. Detailed analysis of kernel strength along with a physical explanation of its behavior will be reserved for Chapter 4. It will also be shown that due to the typical value obtained for t_e, the nature of the resulting kernel precludes the use of the future-time regularization method. Hence, an alternative method is now proposed.

From Eqs. (2.23a-c) we can observe that $f(t)$ and $K(b,w,t-u)$are comprised solely of known experimental data, and hence, can be pre-calculated at 'n' discrete instances in time that depends on the data collection sampling rate and maximum analysis time.

Using the simple left-handed rectangular rule of quadrature, Eq. (2.23a) can be arranged in matrix format as

$$\mathcal{K}\bar{q} = \bar{f}, \tag{2.24a}$$

where $\mathcal{K}$ is a lower triangular matrix of size (n-1 x n-1) and $\bar{q}$ and $\bar{f}$ are both column vectors of size (n-1 x 1) each. For visualization, Eq. (2.24a) is explicitly displayed as

$$\begin{bmatrix} K(\Delta t) & 0 & \dots & 0 \\ K(2\Delta t) & K(\Delta t) & & \vdots \\ \vdots & & \ddots & 0 \\ K(n\Delta t) & K((n-1)\Delta t) & \dots & K(\Delta t) \end{bmatrix} \begin{bmatrix} q''_{run}(0,0) \\ q''_{run}(0,\Delta t) \\ \vdots \\ q''_{run}(0,(n-1)\Delta t) \end{bmatrix} = \begin{bmatrix} f(\Delta t) \\ f(2\Delta t) \\ \vdots \\ f(n\Delta t) \end{bmatrix}, \qquad (2.24b)$$

(n-1 x n-1) (n-1 x 1) (n-1 x 1)

where Δt is the sampling time step.

Equation (2.24b) presents us with a system of n-1 equations for solving n-1 unknowns, namely, the values of $q''_{run}(0,t)$ at n-1 discrete instances in time. The values of the kernel $K(b,w,t-u)$ for initial time t < t_e are very close to zero. However, owing to the presence of experimental noise, the kernel does not become identically equal to zero. The important point to appreciate is that the kernel has not reached a meaningful value yet, or in other words, has not come out of the 'uncertainty band' since the 'w' probe still has to feel the effect of the differences in the back-face conditions of the two calibration runs in a meaningful way. This implies that the initial rows of $\mathcal{K}$ are populated exclusively by a combination of zeros and extremely small numbers tending to zero. For all practical purposes, the initial rows cannot be considered linearly independent and as a result, render the matrix $\mathcal{K}$ singular (to working precision) and hence ill-conditioned. The presence of noise in the RHS $\bar{f}$ and the singular nature of the kernel matrix $\mathcal{K}$ preclude the use of direct inversion ($\bar{q} = \mathcal{K}^{-1}\bar{f}$) to solve for $\bar{q}$.

A method for reconditioning $\mathcal{K}$ in order to find its pseudo-inverse is required. The singular value decomposition (SVD) of $\mathcal{K}$ has proven to be an excellent candidate to fulfill this task.

The SVD of any matrix A of size (m x n) exists and is expressed as [28,29]

$$A = USV^T, \qquad (2.25a)$$

where U is an orthonormal matrix of size (m x m) whose columns span the row space of A, V is also an orthonormal matrix of size (n x n) but whose columns span the column space of A, and S is a diagonal matrix of size (m x n) where the diagonal contains the singular values 'λ' of A arranged in descending order.

Assuming A to be a rectangular matrix with m > n, the singular value decomposition of A is expressed explicitly in matrix format as

(m x n)

$$\begin{bmatrix} & & \\ & A & \\ & & \end{bmatrix} = \begin{bmatrix} | & | & | & & | \\ | & | & | & & | \\ u_1 & u_2 & u_3 & \cdots & u_m \\ | & | & | & & | \\ | & | & | & & | \end{bmatrix} \begin{bmatrix} \lambda_{11} & 0 & \cdots & 0 \\ 0 & \lambda_{22} & & \\ & & \lambda_{33} & \vdots \\ \vdots & & & 0 \\ & & & \lambda_{nn} \\ 0 & & \cdots & 0 \end{bmatrix} \begin{bmatrix} | & | & & | \\ | & | & & | \\ v_1 & v_2 & \cdots & v_n \\ | & | & & | \\ | & | & & | \end{bmatrix}^T, \quad (2.25b)$$

(m x m) (m x n) (n x n)

where $\{u_j\}_{j=1}^{m}$ and $\{v_j\}_{j=1}^{n}$ are the column vectors of U and V respectively. The matrix A is said to be ill-conditioned if for a certain index p < n, $\{\lambda_{jj}\}_{j=p}^{n} \ll \lambda_{11}$ holds true. The SVD offers an easy way of reconditioning A by eliminating the afore-mentioned set of singular values $\{\lambda_{jj}\}_{j=p}^{n}$. Now consider the linear system of equations presented by Eq. (2.24a) but with $\mathcal{K}$ replaced by its singular value decomposition as

$$(USV^T)\bar{q} = \bar{f}, \quad (2.26a)$$

or explicitly presented as

$$\begin{bmatrix} | & | & & | \\ u_1 & u_2 & \cdots & u_{n-1} \\ | & | & & | \\ | & | & & | \end{bmatrix} \begin{bmatrix} \lambda_{11} & 0 & \cdots & 0 \\ 0 & \lambda_{22} & & \vdots \\ \vdots & & \ddots & 0 \\ 0 & \cdots & 0 & \lambda_{n-1n-1} \end{bmatrix} \begin{bmatrix} | & | & & | \\ v_1 & v_2 & \cdots & v_{n-1} \\ | & | & & | \\ | & | & & | \end{bmatrix}^T \begin{bmatrix} q_{run}^{"}(0,0) \\ q_{run}^{"}(0,\Delta t) \\ \vdots \\ q_{run}^{"}(0,(n-1)\Delta t) \end{bmatrix} = \begin{bmatrix} f(\Delta t) \\ f(2\Delta t) \\ \vdots \\ f(n\Delta t) \end{bmatrix}. \quad (2.26b)$$

Since the parent matrix $\mathcal{K}$ is square, its U, S and V components each retain the dimensions (n-1 x n-1). To gain insight on the action of the singular values in Eq. (2.26b), it is expressed as an outer product expansion given by

$$\left(\lambda_{11}u_1v_1^T + \lambda_{22}u_2v_2^T + \cdots + \lambda_{pp}u_pv_p^T + \cdots + \lambda_{n-1n-1}u_{n-1}v_{n-1}^T\right)\bar{q} = \bar{f}. \quad (2.27a)$$

As mentioned before, for an ill-conditioned $\mathcal{K}$, there will be some index j = p, called the truncation index, for which $\{\lambda_{jj}\}_{j=p}^{n-1} \ll \lambda_{11}$ holds true. Therefore, we can now safely assume the following expression to hold.

$$\bar{f} - \left(\lambda_{pp} u_p v_p^T + \cdots + \lambda_{n-1n-1} u_{n-1} v_{n-1}^T\right)\bar{q} \approx \bar{f}. \tag{2.27b}$$

The elimination of the set of relatively negligible singular values $\{\lambda_{jj}\}_{j=p}^{n-1}$ helps recondition $\mathcal{K}$ without significantly altering the physics of the system.

The new truncated matrix S will now have dimensions (p x p). To maintain dimensional consistency, the U and V matrices are also truncated accordingly and have dimensions (n-1 x p). Let the new resized components of $\mathcal{K}$ be denoted as

$$U_{new} \triangleq \begin{bmatrix} | & | & & | \\ u_1 & u_2 & \dots & u_p \\ | & | & & | \\ | & | & & | \end{bmatrix}, \tag{2.28a}$$

$$V_{new} \triangleq \begin{bmatrix} | & | & & | \\ v_1 & v_2 & \dots & v_p \\ | & | & & | \\ | & | & & | \end{bmatrix}, \tag{2.28b}$$

$$S_{new} \triangleq \begin{bmatrix} \lambda_{11} & 0 & \dots & 0 \\ 0 & \lambda_{22} & & \vdots \\ \vdots & & \ddots & 0 \\ 0 & \dots & 0 & \lambda_{pp} \end{bmatrix}, \tag{2.28c}$$

which then gives us

$$\mathcal{K}_{new} \triangleq U_{new} S_{new} {V_{new}}^T. \tag{2.28d}$$

Replacing $\mathcal{K}$ with the reconditioned $\mathcal{K}_{new}$, Eq. (2.24a) now becomes

$$\mathcal{K}_{new}\bar{q} \approx \bar{f}. \tag{2.29a}$$

To maintain the equality sign, we introduce a new vector $\bar{q}_p$, which is an approximation to $\bar{q}$, where

$$\bar{q}_p \approx \bar{q}\,, \qquad (p < n-1),$$
$$\bar{q}_p = \bar{q}\,, \qquad (p = n-1).$$

Equation (2.29a) now becomes

$$\mathcal{K}_{new}\bar{q}_p = \bar{f}. \tag{2.29b}$$

The new vector $\bar{q}_p$ can now be easily solved for by multiplying both sides of Eq. (2.29b) by the left pseudo-inverse of $\mathcal{K}_{new}$. The left pseudo-inverse of $\mathcal{K}_{new}$ is given by

$$\mathcal{K}_{new}{}^{+} = \left(U_{new}S_{new}V_{new}{}^{T}\right)^{-1} = V_{new}{}^{T\,-1}S_{new}{}^{-1}U_{new}{}^{-1}. \tag{2.30a}$$

But since $U_{new}$and V_{new} are orthonormal matrices, their inverse is equal to their transpose [28,29], to give

$$U_{new}{}^{-1} = U_{new}{}^{T}, \tag{2.30b}$$

$$V_{new}{}^{-1} = V_{new}{}^{T}. \tag{2.30c}$$

The inverse of a diagonal matrix is merely the reciprocal of the diagonal elements [28,29]. Therefore, Eq. (2.30a) can be written as

$$\mathcal{K}_{new}{}^{+} = V_{new}S_{new}{}^{+}U_{new}{}^{T}. \tag{2.30d}$$

Pre-multiplying both sides of Eq. (2.29b) by $\mathcal{K}_{new}{}^{+}$as per Eq. (2.30d), we get

$$\mathcal{K}_{new}{}^{+}\left(\mathcal{K}_{new}\bar{q}_p\right) = \mathcal{K}_{new}{}^{+}\bar{f}. \tag{2.30e}$$

Substituting Eq. (2.30d) in Eq. (2.30e), we arrive at the final expression for the predicted surface heat flux $\bar{q}_p$ given by

$$\bar{q}_p = \left(V_{new}S_{new}{}^{+}U_{new}{}^{T}\right)\bar{f}. \tag{2.30f}$$

The truncation index p is the regularization parameter and its choice depends on the designer and the specific application. The application in this study is the solution of the IHCP and the determination of the optimum value or range of p is based on a statistical approach described in the Chapter 4.

CHAPTER SUMMARY

The one-probe and two-probe calibration integral equation methods were introduced. The thought process behind the derivation of these equations was explained. After the initial observation based on half space analysis, the broadening in applicability of the physics-based calibration approach was showcased for finite width two-layer domains. The underlying assumptions and operating constraints of the linear calibration integral equations can be stated as follows.

1) Constant thermo-physical properties.
2) One-Dimensional heat conduction.
3) Identical back-boundary conditions required for the one-probe calibration method.
4) Largely varying back-boundary conditions during the calibration tests one and two is required for the two-probe calibration method.

The regularization schemes considered for this thesis were introduced. The choice of solution scheme depends on the governing physics of the respective methods. The selection of optimum band for the regularization parameter(s) will be accomplished by use of certain metrics and will be discussed in Chapter 4. In this chapter the mathematical and conceptual framework that is required for the proper selection of the experimental test cases is established. The test data and its analysis will be presented in Chapters 3 and 4 respectively.

CHAPTER 3. EXPERIMENTAL SETUP AND TEST DATA

3.1 INTRODUCTION

A pre-existing experimental setup was utilized for a considerable portion of this work. The setup was inherited from a former graduate student, Mr. Jake Eric Plewa [36,37], and was in perfect operating condition. Necessary modifications and updates were made to enhance the capabilities of the setup. A detailed description of the original setup and subsequent modifications will be provided first. The test procedure followed in making an experimental run will be explained. The chapter will conclude with the presentation of the selected experimental runs considered for this work.

3.2 EXPERIMENTAL SETUP (REV 0)

The details and description of the setup have been adopted and suitably modified from a previous Master's thesis entitled "Heat Transfer Analysis via Rate Based Sensors" [37] by Jake Eric Plewa. Figure 3.1 shows a schematic diagram of an electrical heating experiment with embedded thermocouple sensors. The test samples were two identical stainless steel plates with a heater assembly sandwiched in between. The samples were coated with a thin layer of Omega Thermal Paste on their heated-side faces. Since the purpose of the paste was to reduce contact resistance, the thinnest layer possible was used. A thin layer of muscovite mica (0.08mm thick) was laid between the plates. The steel/paste/mica layers were then used to sandwich a 0.125 mm thick custom nichrome heater element. Figure C.1, in appendix C, shows a conceptual sketch of the custom nichrome heater designed by Dr. Majid Keyhani. This created a line of thermal symmetry across the centerline of the heater. Thermo-physical and electrical properties of these materials can be seen in Table C.1, while material thicknesses are summarized in Table C.2.

Multiple 1.19mm diameter holes were drilled into each stainless steel plate from the back surface (perpendicular to the heated surface). These holes were drilled to two different relative depths, the depth closer to the heated surface known as the "A" depth all of which are approximately 6.5mm from the heated surface. The second depth, "B" depth, had holes all about 12.9mm from the heated surface. The depth of each hole was rigorously measured using a Micro Val coordinate measuring machine; these depths are presented in Table C.3. Each hole follows a naming system that starts with which slab it is embedded in, S1 for Slab 1 and S2 for Slab 2. Next, the depth to the surface is indicated by A or B. And finally the horizontal distance from the slab centerline is indicated by the last number; the higher that number the farther the

hole will be from the center of the slab. Therefore S2A0 is on the centerline of Slab 2 and about 6.5mm from the heated surface. The horizontal distances from the centerline are also displayed in Table C.3.

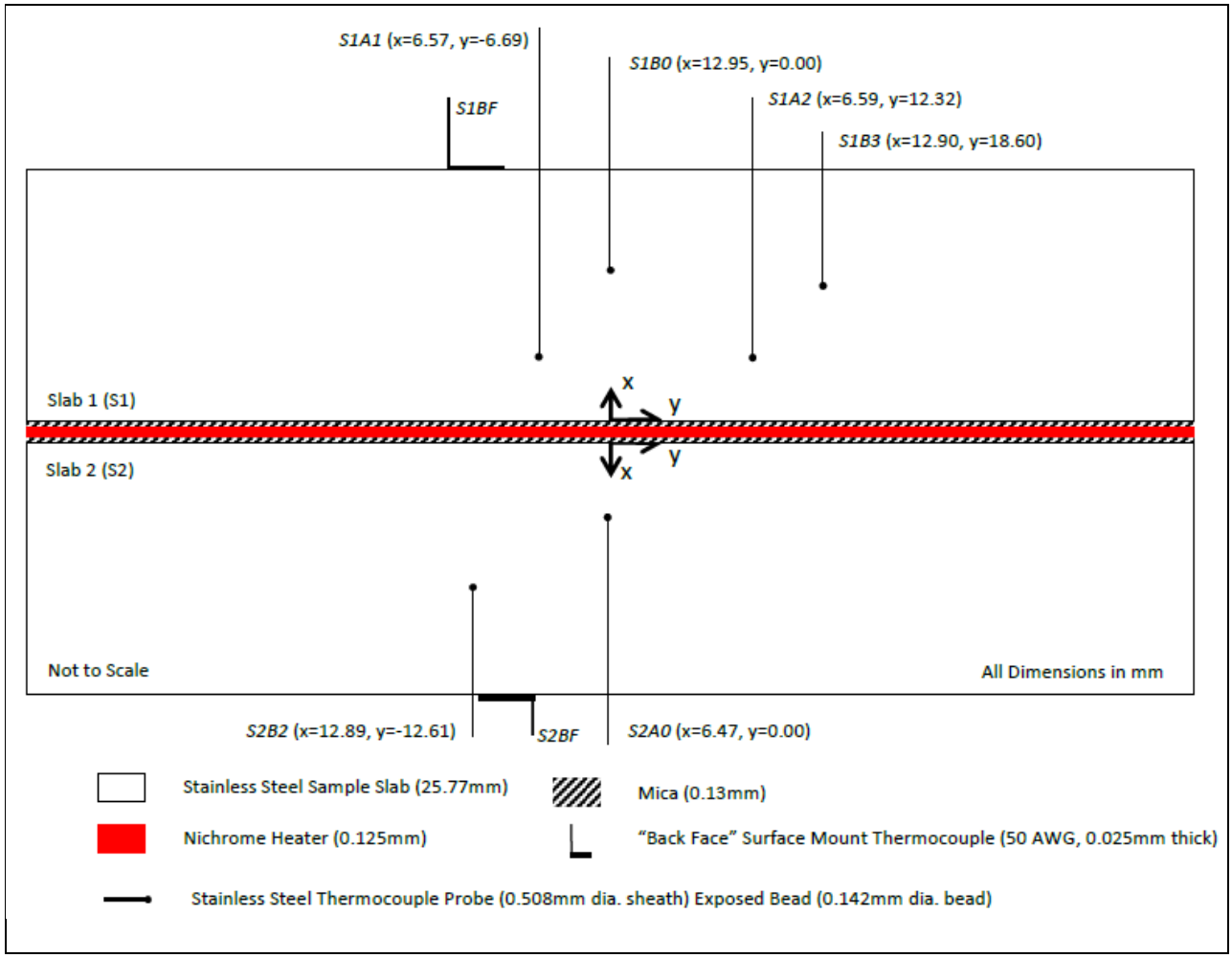

Figure 3.1. Electrical Heating Experimental Setup (Rev 0). A line of thermal symmetry exists along the centerline of the heater. Not to scale. [37]. The thickness of the Mica layer is now corrected to read 0.076mm instead of 0.13mm.

Type T Omega TMTSS transition junction style thermocouple (TC) probes with 38 AWG wires were used for temperature measurement. The probes had exposed beads with a diameter of 0.142mm and were sheathed with stainless steel tubes with a diameter of 0.508mm. The probes were potted in each hole using Cotronics 989F alumina paste (k=1.73 W/(mK)) as an

electrical insulator. Confirmation that each thermocouple bead was in contact with each slab was achieved by measuring the electrical resistance between the thermocouple's copper lead wire and the stainless steel slab. The measured resistances that are presented in Table C.3, verified good contact between thermocouple beads and the stainless steel slabs. Fine gage (50 AWG wire) surface mount thermocouples (Omega SA1XL-T) were affixed to the back (unheated) surface of each stainless steel plate.

The thermocouple's emf outputs were sampled at 100 Hz (modified from the original value of 200 Hz as in [17]) with a gain of 32 via a DT9824 data acquisition board (DAQ) – a 24 bit, ±10V Range, low noise, fully isolated DAQ with simultaneous channel measurement. The thermocouples were referenced to ice and the compensated voltages were converted to temperature via the NIST polynomial calibration curve for type T thermocouples [38]. Unregulated alternating current (60 Hz) was supplied to the heater via a voltage transformer (Variac) that allowed for variation of the input voltage to the heater. The voltage input of the Variac was line voltage (120VRMS, 50A). The output of the Variac was wired to an 80A solid state relay which was software triggered. The output of the relay was wired to the nichrome heater. The voltage across the heater was also connected to a 1/28.67 voltage divider which was sampled at 4800 Hz via another DT9824 data acquisition board. For a detailed list of equipment and material used in the sandwich experiment see [39]. Finally, the net heat flux $q''(0,t)$, that enters each slab at the surface is calculated by,

$$q''(0,t) = \frac{V_{rms}^2(t)}{2RA_H} \tag{3.1}$$

where $V_{rms}(t)$ is the measured RMS voltage in the heater, *R* is the resistance of the heater and A_H is the heated area. The heater resistance was measured with a Hewlett Packard Digital Voltmeter (HP3456A) with 6½ digit resolution, before and immediately after the test to ensure that it remained constant during the heating period.

3.2.1 Revision 1

The existing setup had no means of altering the back-face boundary condition as required by the two-probe calibration integral method. The back-faces of the stainless steel slabs were open to the surroundings and hence were restricted to a natural convection boundary condition. Necessary modifications to the setup were made to facilitate a forced convection boundary condition at the back-faces. The compressed air supply capability of the building was utilized to subject the back-faces to a high flow-rate air stream. The important design constraint was to ensure that the air supply to both the slabs was identical to maintain thermal symmetry

in the system. The main compressed air line was tapped in and split into two lines. Pressure regulators were installed in the two lines to ensure equal flow-rates. Flexible hoses of equal lengths were connected to the outputs of the regulators via flow-control valves. The free ends of the hoses were routed to the sides of the stainless steel slabs and held in place by fixtures at the desired height and angle with respect to the two back-faces. The angle and height from which the air flow hits the back-face was adjusted to maximize the heat transfer coefficient and preserve thermal symmetry. It would be important to remind the reader that precise knowledge of the value of the heat transfer coefficient is not required. The main objective is to maintain thermal symmetry by having air at equal flow-rates hit the two back-faces at the same angle and from the same height.

Figures C.2 to C.4 show pictures of the modified experimental setup. The arrangement for producing a forced-convection boundary condition at the back-faces will be clearly seen and understood from these figures.

3.2.2 Revision 2

The mica sheets were rated to provide good electrical resistance up to a maximum operating temperature of 300^{o}C. Beyond this temperature the mica sheets would permit the flow of electricity across them, rendering the nichrome heater and the stainless-steel slabs electrically connected. For this reason, the mica sheets were each replaced with Alumina sheets (CoorsTek ADS-96R, k=26 W/(mK)) of dimensions 128 mm x 138 mm x 0.38 mm. Alumina has a maximum use temperature of 1700^{o}C. This allowed for higher levels of heating and for longer durations. In addition, the extra thickness of the Alumina sheets (0.38 mm as compared to 0.076 mm for Mica) justified the treatment of the domain as a two-layer domain. The functionality of the two-layer calibration integral equation methods (one-probe & two-probe) could now be explored. Figure 3.2 shows the schematic of the revised sandwich setup with the Alumina sheets. While assembling the sandwich setup, the orientation was reversed in that Slab 2 (S2) was now at the top and Slab 1 (S1) was at the bottom. This inverted positioning is reflected in Figure 3.2. The intended ‘A’ and ‘B’ depths of thermocouple locations are also marked. The assembled sandwich setup is clearly seen in the close-up photograph in Figure C.4.

The test procedure followed in performing an experimental run will now be explained.

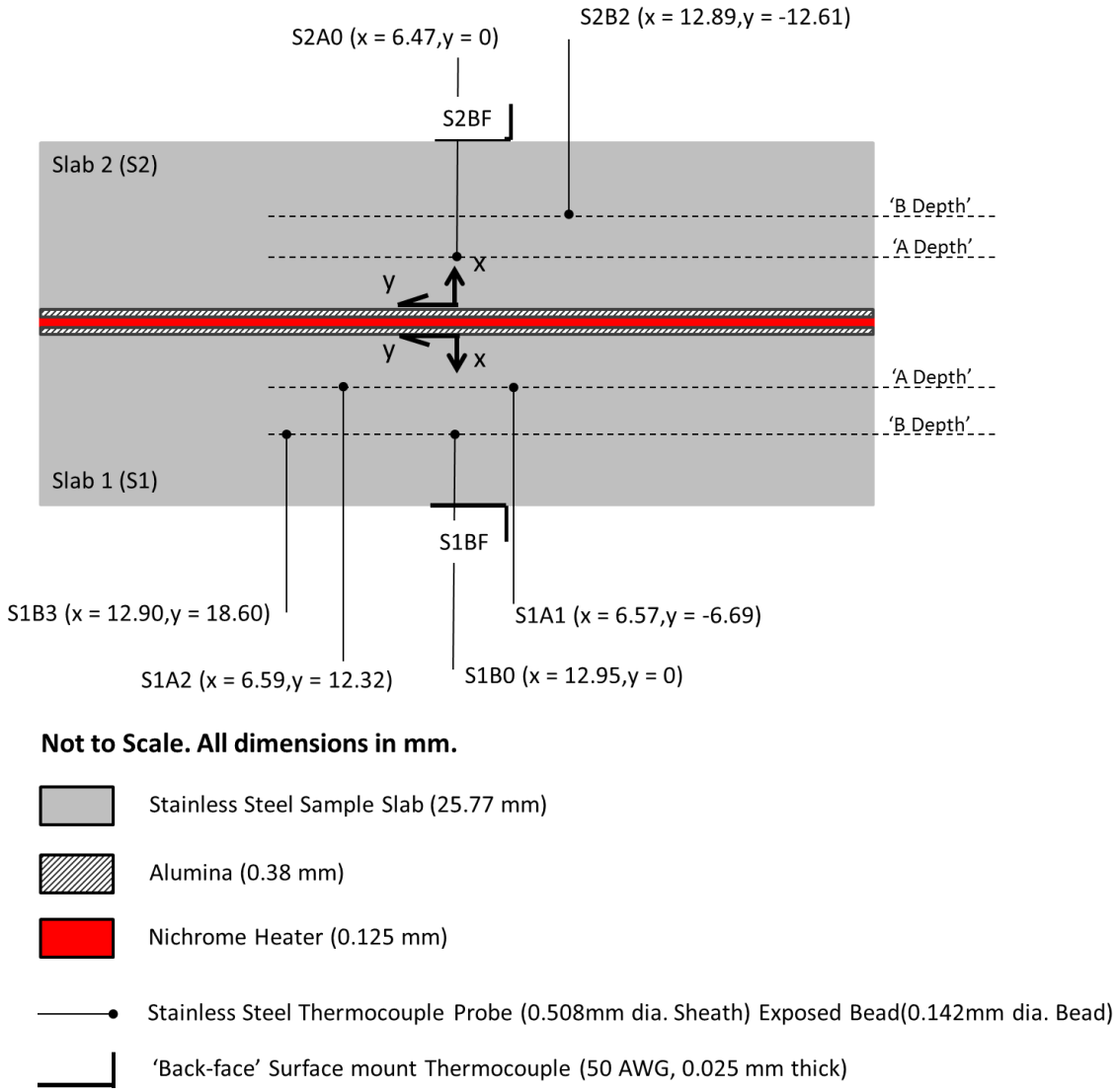

Figure 3.2. Electrical Heating Experimental Setup (Rev 2). A line of thermal symmetry exists along the centerline of the heater. The 'back-face' thermocouples were placed near the center. Not to scale.

3.3 TEST PROCEDURE

The following procedural steps were followed to conduct each test. All instruments were allowed their proper warm-up times, the longest being 1hr. First the resistance of the heater was recorded for later use in determining exact heat flux input and to ensure that its value had not changed. Next the resistance between each slab and the heater was measured to ensure that electrical insulation between Mica (or Alumina) has not been lost. Any reading besides

overload would indicate that the Mica has been damaged and the heater is electrically connected to the slab. Next all connections between heater, power source, and the voltage bridge were made and double checked. The final steps take place in the Matlab data collection program. After entering all the required program settings, a test run with no input power was conducted to ensure proper test execution and record base TC noise level. Unacceptable base TC noise, quantified by the standard deviation of the measurements during this 'dry' run, would result in repeating this step or waiting until noise conditions were optimal. This run also had the function of confirming that uniform initial temperature exists throughout each slab. With all pre-tests steps completed, the wall power source was turned on and the actual test was conducted. During each calibration tests (constant input voltage) the input voltage was measured using a Fluke 117 (true RMS Multimeter, with 1mV resolution) and input current was measured using a Fluke 378 (true RMS Clamp Meter, with 0.1A resolution) to verify the DAQ system readings. The measured current range was 40 to 50A.

Additional Steps for Performing a Forced Convection Run:

While the DAQ boards were warming up, the compressed air flow was started at a low level to stabilize the air steam temperature. The stabilized airstream temperature and the surrounding ambient air temperature were measured with a hand-held thermocouple meter. As explained later, for the two-probe analysis, the back-face thermocouple (S2BF) was used for the 'w' location temperature response. Since S2BF lies on the back-face of the slab 2, it is highly sensitive to any difference between the airstream and ambient room temperatures. This difference results in a 'bias' in the measured temperature response. However, the bias is not registered by the 'b' location probe (S2A0) since it lies about 21mm from the back-surface. Furthermore, any prolonged exposure to an airstream whose temperature is different from the room temperature would alter the required uniform slab initial temperature. When a pair of such temperature response data is used in the two-probe calibration integral equation, it senses the discrepancy as a difference in the initial temperatures and results in an unacceptable prediction. It is therefore vital to have a minimum difference between the airstream and ambient air temperatures. Accordingly, the two temperatures were monitored and any difference was minimized by adjusting the room (ambient) temperature. Adequate time was allowed for the room temperature to stabilize. The experiment was performed only after a difference of 1^{o}C or lower was attained. The values of the airstream temperature and the ambient temperature were recorded and the forced air flow was stopped. From this point onwards the steps explained previously in the Test Procedure were followed. After the heating started, roughly 10 seconds were allowed to elapse before the compressed air flow was turned on and gradually increased to the maximum level. This ensured that the heat front had

penetrated the back-face (observed penetration time ≈ 9s) and the occurrence of any bias in the measured temperature response is prevented. The air flow was maintained at the maximum level and only turned off after the data collection had finished.

3.4 ROSTER OF EXPERIMENTAL RUNS

The experimental runs considered for this thesis will now be presented. The runs performed with Mica as the electrical insulator (Mica Runs) will be considered for the single-layer analysis whereas the runs with Alumina as the electrical insulator (Alumina Runs) will be used for the two-layer analysis. The specific calibration and 'real' run data will be selected from these tests as desired.

3.4.1 Mica Runs (for Single-layer Analysis)

Four experimental runs will be presented as the Mica Runs. Using 'Mc' as the prefix for 'Mica', individual runs will be referred to as 'McRun1' for the first Mica Run, 'McRun2' for the second Mica Run and so on and so forth. Data for each run were collected for duration of 59.99 seconds (t_{max}) including at least 5 seconds of lead time. Table 3.1 gives an overview of the four Mica runs.

In Table 3.1, the heat start time 't_{ON}' marks the time at which the solid state relay closes and the heating starts. It also indicates the amount of lead time available. Similarly, 't_{OFF}' indicates the time at which the relay opens and the heating stops. The lead data, which is the data collected during the lead time, serves two important purposes. The arithmetic mean of the lead data provides the value of the initial temperature T_o which is subtracted from the corresponding measured thermocouple temperature response. The 'rise-above-initial' temperature history is thus obtained as required by the calibration integral equation method. The standard deviation σ of the lead data quantifies the level of noise in the measured thermocouple temperature response. Accordingly, σ_b and σ_w represent the noise levels in the temperature responses recorded by the 'b' and 'w' depth probes. The choice of thermocouples S2A0 and S2BF as the 'b' and 'w' depth probes respectively is explained later on in the Results & Discussion chapter. The symbol q''_{max} represents the maximum level of heat flux attained during the runs. For McRuns 1 and 2, q''_{max} is the mean value of the constant pulse heat flux whereas for the flight runs (McRuns 3 and 4) q''_{max} represents the peak value of the heat flux. The symbol E represents the total energy input to the slab during a run and is obtained by integrating the heat flux with respect to time and is given as

$$E = \int_{t=0}^{t_{max}} q''(0,t)dt \ , \ t \in [0, t_{max}]. \quad (3.2)$$

Table 3.1. Overview of Mica Runs. t_{max} = 59.99 s.

Name	Type	t_{ON} (s)	t_{OFF} (s)	q''_{max} (W/cm^2)	Back Boundary Condition	T_o (^{o}C)	σ_b (^{o}C)	σ_w (^{o}C)	E (J/cm^2)
McRun1	Pulse	5.01	50.07	10.41	Natural Convection	22.1	0.035	0.022	468.44
McRun2	Pulse	5.01	45.03	9.26	Forced Convection	22.4	0.031	0.023	368.29
McRun3	Flight	6.52	45.02	10.25	Natural Convection	22.4	0.030	0.023	204.03
McRun4	Flight	5.93	40.86	10.06	Natural Convection	22.7	0.030	0.022	128.39

Figures 3.3(a-d) to 3.6(a-d) present the data for McRun1 to Mcrun4 tests. Each figure presents: (a) the measured heat flux, (b) the 'A depth' thermocouple response, (c) the 'B depth' thermocouple response, and (d) the back-face thermocouple response.

By comparing the 'A depth' and 'B depth' temperature data shown in Figures 3.3(b,c) to 3.6(b,c), we can observe that the temperature responses of the probes at similar depths are very close to each other. The loss of heat through the side walls of the slabs is apparent but not dominant. It is thus safe to claim that the one-dimensional heat transfer assumption has not been grossly violated. The back-face temperature data presented in Figures 3.3(d) to 3.6(d) display excellent thermal symmetry between the two stainless steel slabs which proves that each plate must be subjected to one-half of the total heat supplied by the sandwiched Nichrome heater.

During McRun2, compressed air was blown on the back-faces of the stainless steel slabs to produce a forced convection boundary condition. The initial fluctuations in the back-face thermocouple temperatures shown in Figure 3.4(d) can be attributed to a slight difference in the compressed air and the ambient room temperatures. The influence of this difference on the back-face temperature response, as discussed in the test procedure, is clearly seen in Figure 3.4(d).

McRun1:

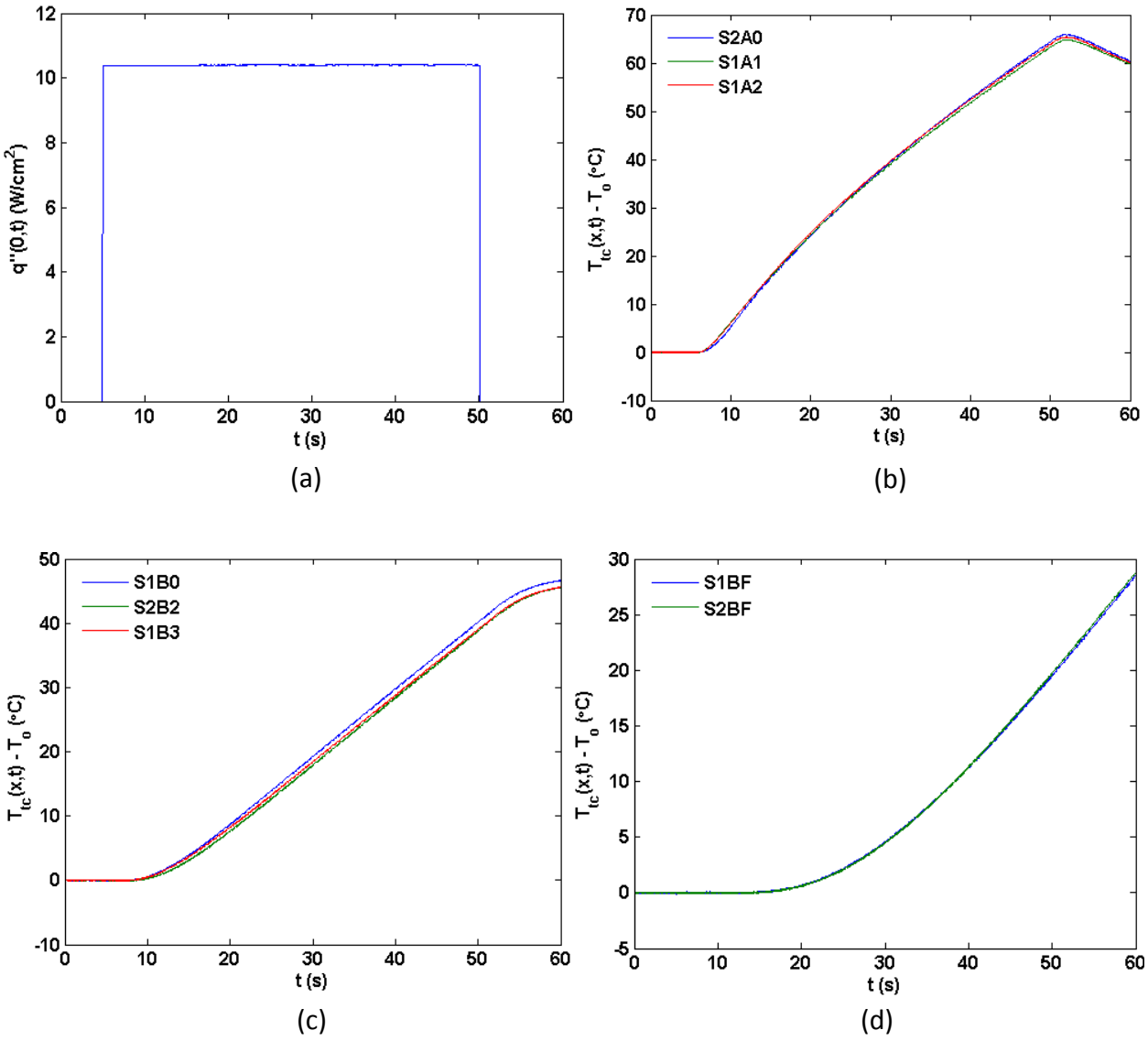

Figure 3.3. McRun1 data - (a) Measured heat flux, (b) A-depth thermocouple temperature histories, (c) B-depth thermocouple temperature histories and (d) Back-face thermocouple temperature histories. The probe locations (x,y) are listed in Table C.3 in Appendix C.

McRun2:

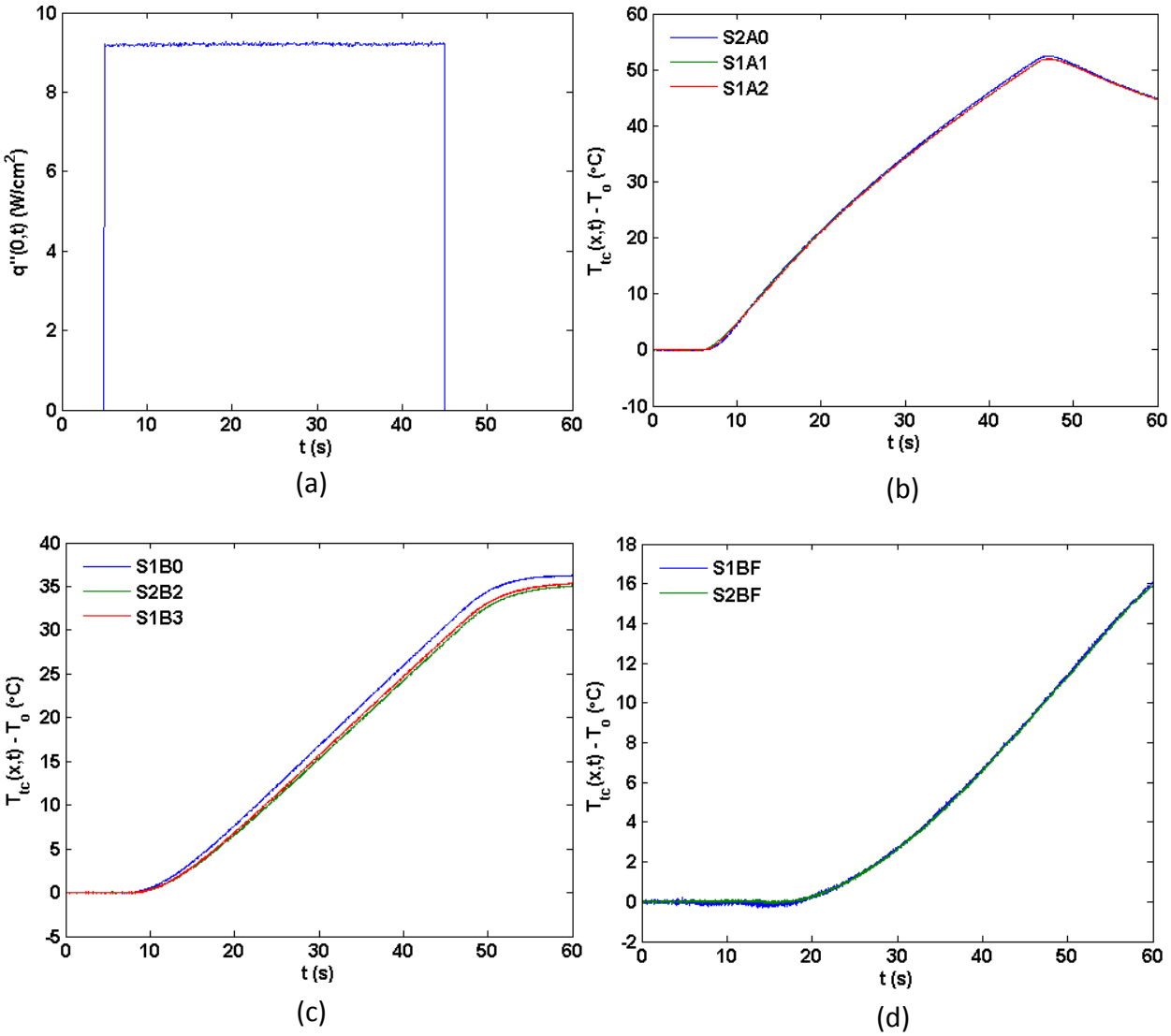

Figure 3.4. McRun2 data - (a) Measured heat flux, (b) A-depth thermocouple temperature histories, (c) B-depth thermocouple temperature histories and (d) Back-face thermocouple temperature histories. The probe locations (x,y) are listed in Table C.3 in Appendix C.

McRun3:

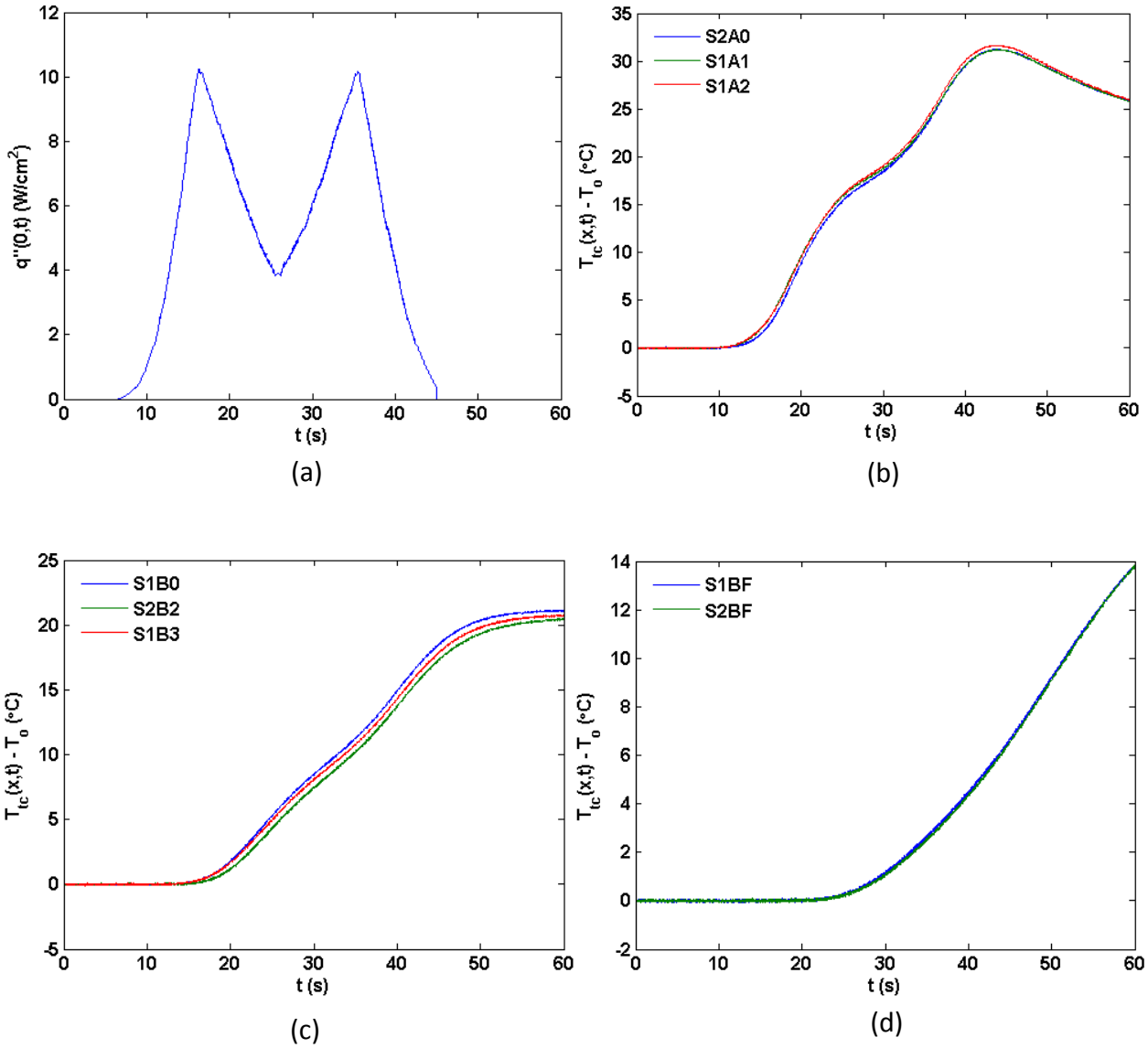

Figure 3.5. McRun3 data - (a) Measured heat flux, (b) A-depth thermocouple temperature histories, (c) B-depth thermocouple temperature histories and (d) Back-face thermocouple temperature histories. The probe locations (x,y) are listed in Table C.3 in Appendix C.

McRun4:

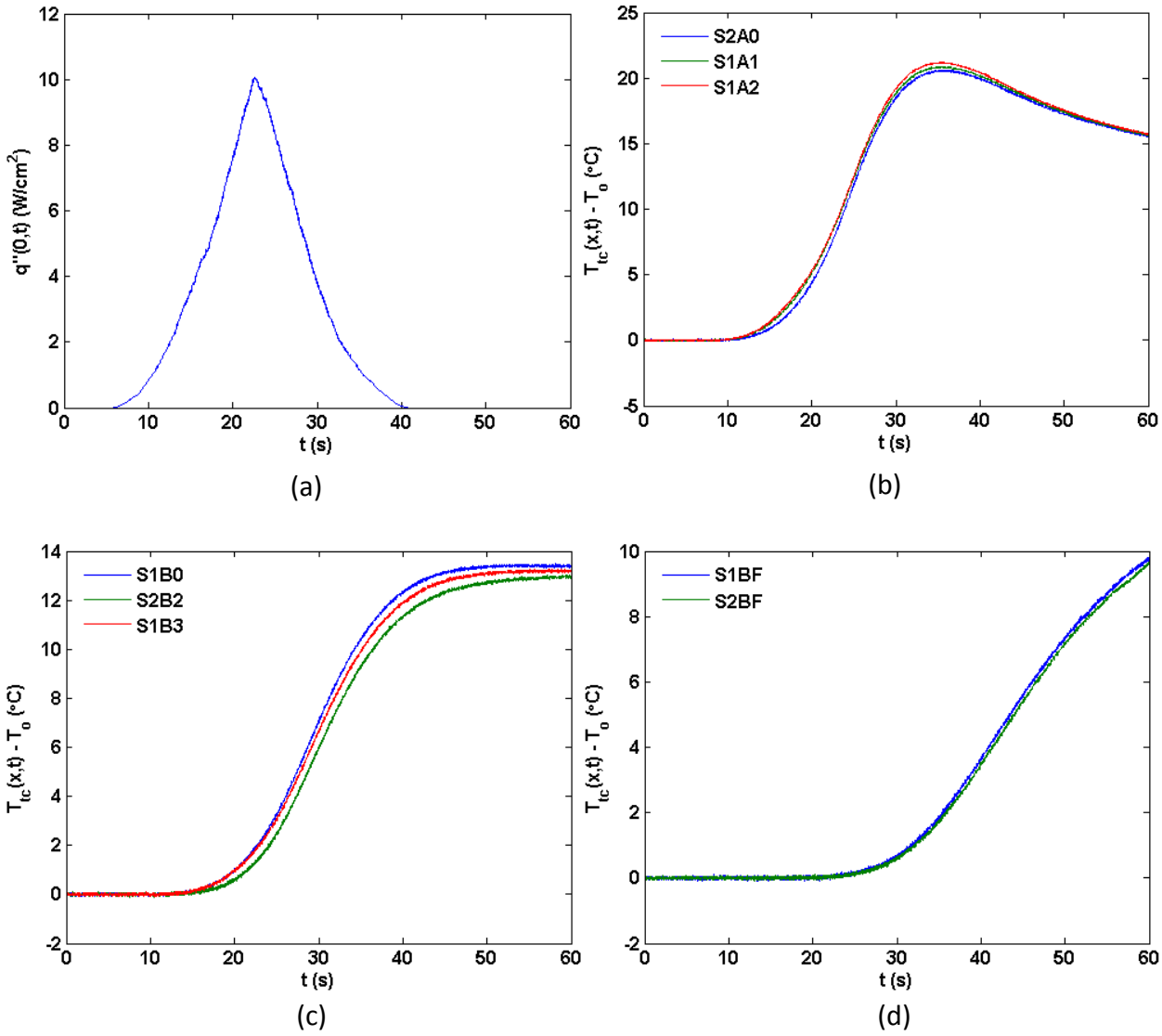

Figure 3.6. McRun4 data - (a) Measured heat flux, (b) A-depth thermocouple temperature histories, (c) B-depth thermocouple temperature histories and (d) Back-face thermocouple temperature histories. The probe locations (x,y) are listed in Table C.3 in Appendix C.

Assuming the maximum surface temperature to be roughly 30K hotter than that at the A depth position, the temperature range of interest can be considered to be from 300K to 400K. Figures C.5 and C.6 show the temperature dependence of thermal conductivity and thermal diffusivity of AISI 304 stainless steel [40]. Within this temperature range, the thermal conductivity increases by about 11% while thermal diffusivity increases by about 5%. The assumption of constant thermo-physical properties is therefore not far-fetched. It can be inferred that the collected experimental data for the Mica Runs is in good agreement with all the underlying assumptions of the calibration integral equation method.

3.4.2 Alumina Runs (for Two-layer Analysis)

Four experimental runs will be presented as the Alumina Runs. Using 'Al' as the prefix for 'Alumina', individual runs will be referred to as 'AlRun1' for the first Alumina Run, 'AlRun2' for the second Alumina Run and so on and so forth. For each run data was collected for 99.98 seconds including at least 5 seconds of lead data. Similar to the Mica Runs, the thermocouple responses were sampled at 100 Hz and the stepped-down heater voltage (across the voltage divider) was sampled at 4800 Hz. The actual voltage across the heater was obtained by multiplying the measured voltage by the voltage divider ratio. The RMS voltage was then calculated. Finally, owing to the longer duration of the Alumina Runs, the RMS voltage was down-sampled to 50 Hz to save memory and computation time. Accordingly, the thermocouple responses were also down-sampled to 50 Hz. Table 3.2 provides an overview of the 4 Alumina Runs considered for this study. Figures 3.7(a-d) to 3.10(a-d) present the measured heat fluxes, the 'A depth' thermocouple responses, the 'B depth' thermocouple responses and the back-face thermocouple responses obtained for the four Alumina Runs.

Table 3.2. Overview of Alumina Runs. t_{max} = 99.98 s.

Name	Type	t_{ON} (s)	t_{OFF} (s)	q''_{max} (W/cm^2)	Back Boundary Condition	T_o (^{o}C)	σ_b (^{o}C)	σ_w (^{o}C)	E (J/cm^2)
AlRun1	Pulse	5.03	95.05	10.94	Natural Convection	22.4	0.033	0.023	984.86
AlRun2	Pulse	5.03	95.06	9.89	Natural Convection	22.6	0.026	0.024	890.02
AlRun3	Pulse	5.03	95.06	9.87	Forced Convection	22.6	0.028	0.023	888.86
AlRun4	Flight	6.7	84.85	10.80	Natural Convection	22.4	0.028	0.025	404.91

AlRun1:

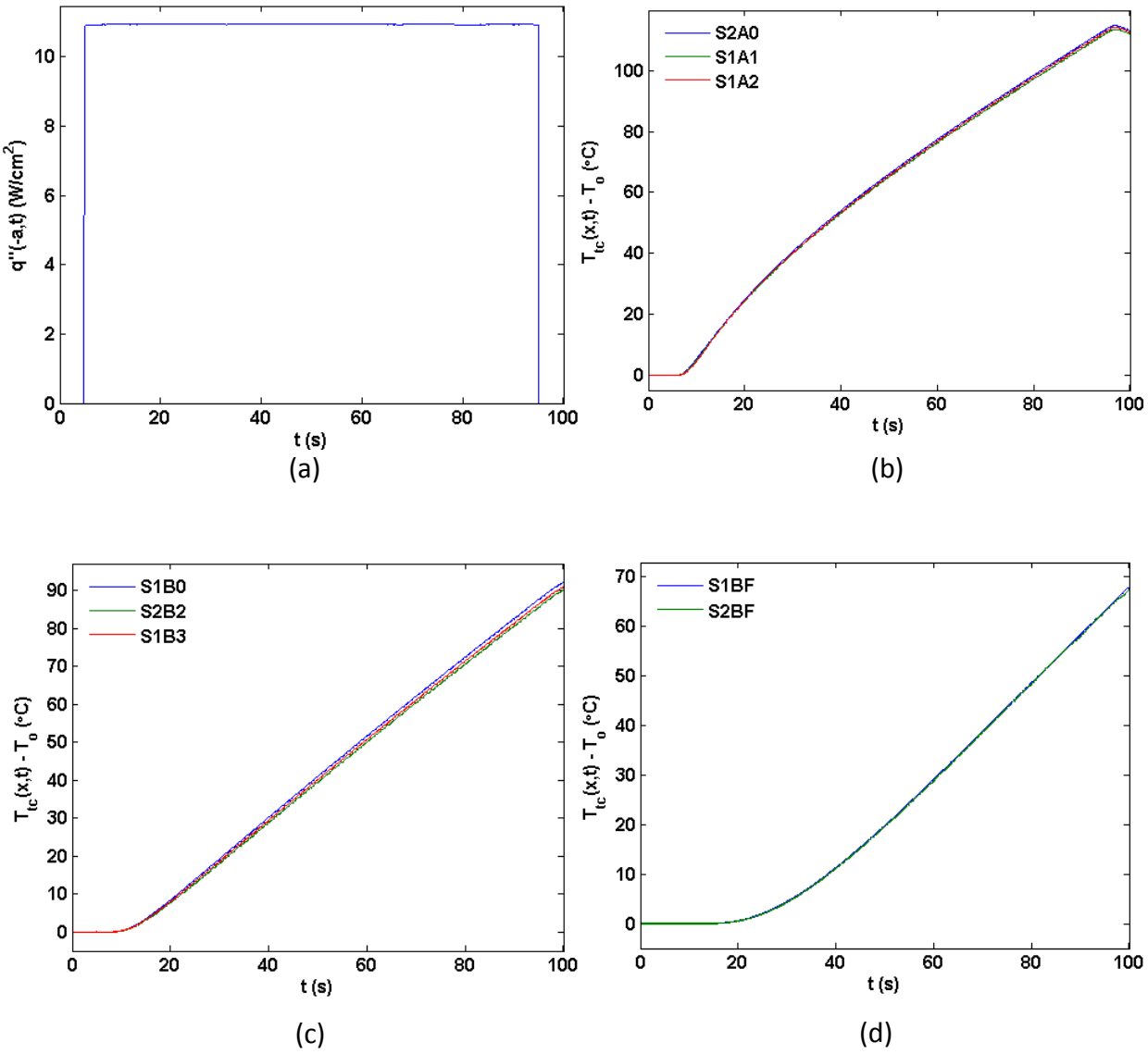

Figure 3.7. AlRun1 data - (a) Measured heat flux, (b) A-depth thermocouple temperature histories, (c) B-depth thermocouple temperature histories and (d) Back-face thermocouple temperature histories. The probe locations (x,y) are listed in Table C.3 in Appendix C.

AlRun2:

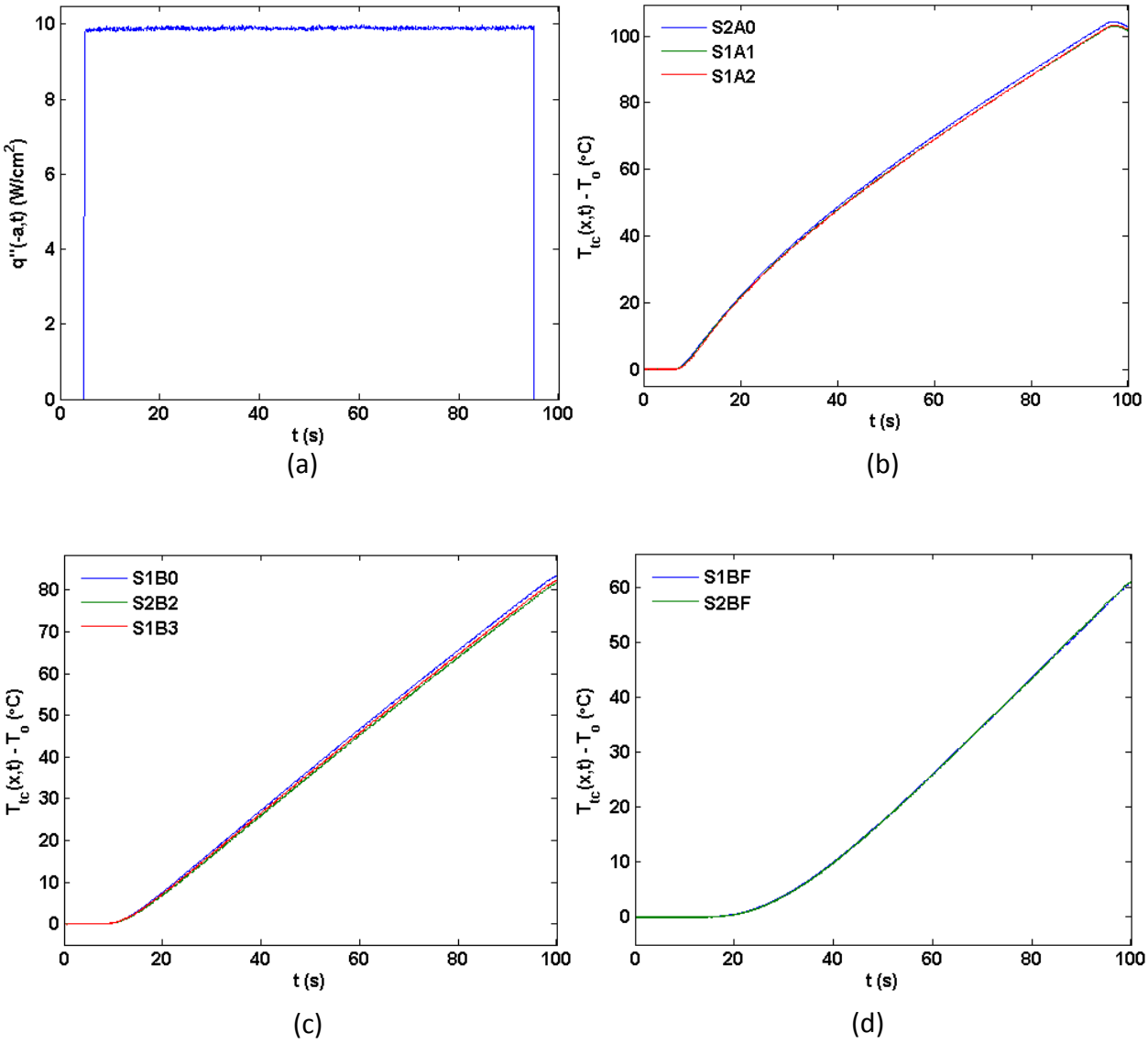

Figure 3.8. AlRun2 data - (a) Measured heat flux, (b) A-depth thermocouple temperature histories, (c) B-depth thermocouple temperature histories and (d) Back-face thermocouple temperature histories. The probe locations (x,y) are listed in Table C.3 in Appendix C.

AlRun3:

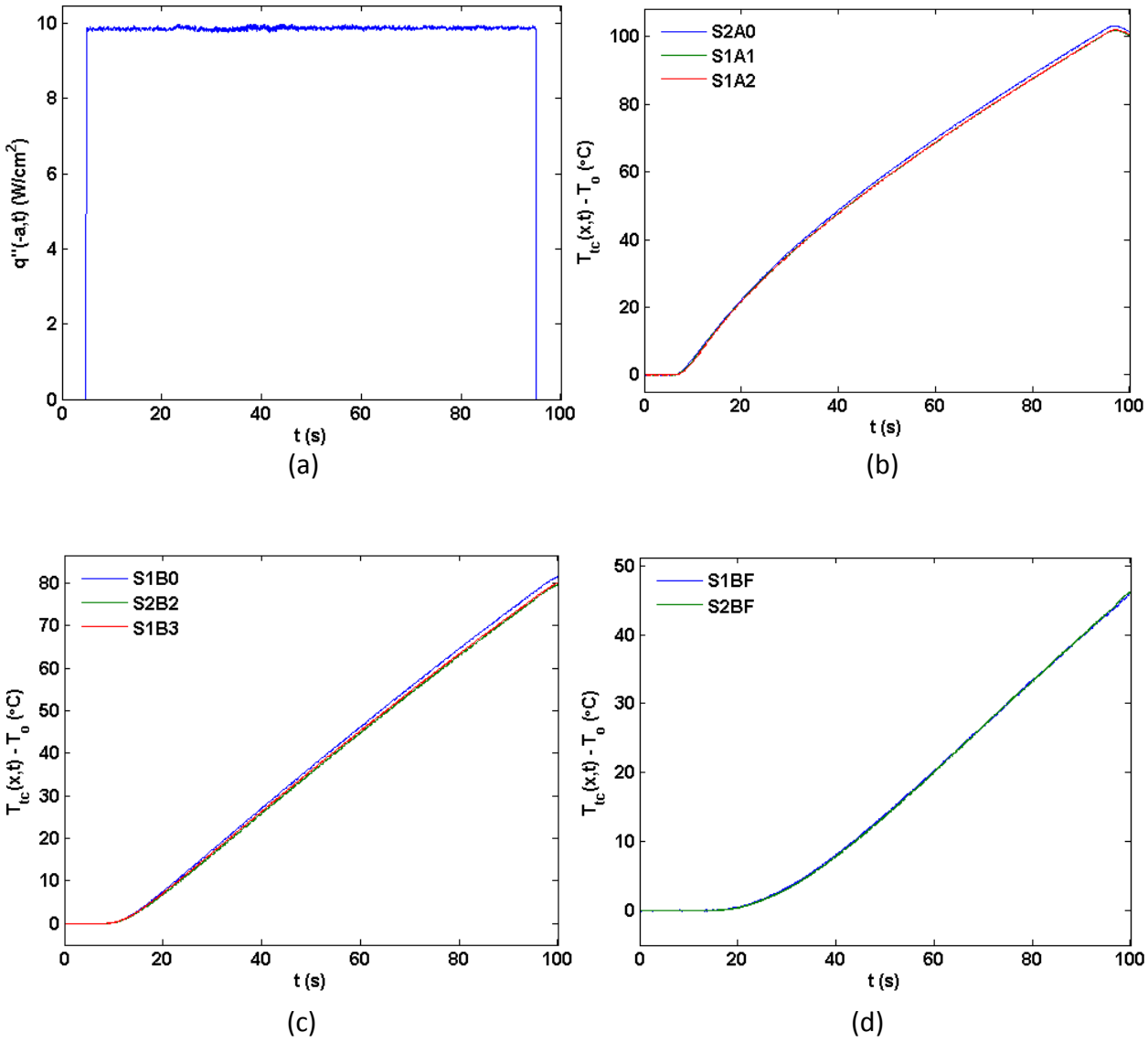

Figure 3.9. AlRun3 data - (a) Measured heat flux, (b) A-depth thermocouple temperature histories, (c) B-depth thermocouple temperature histories and (d) Back-face thermocouple temperature histories. The probe locations (x,y) are listed in Table C.3 in Appendix C.

AlRun4:

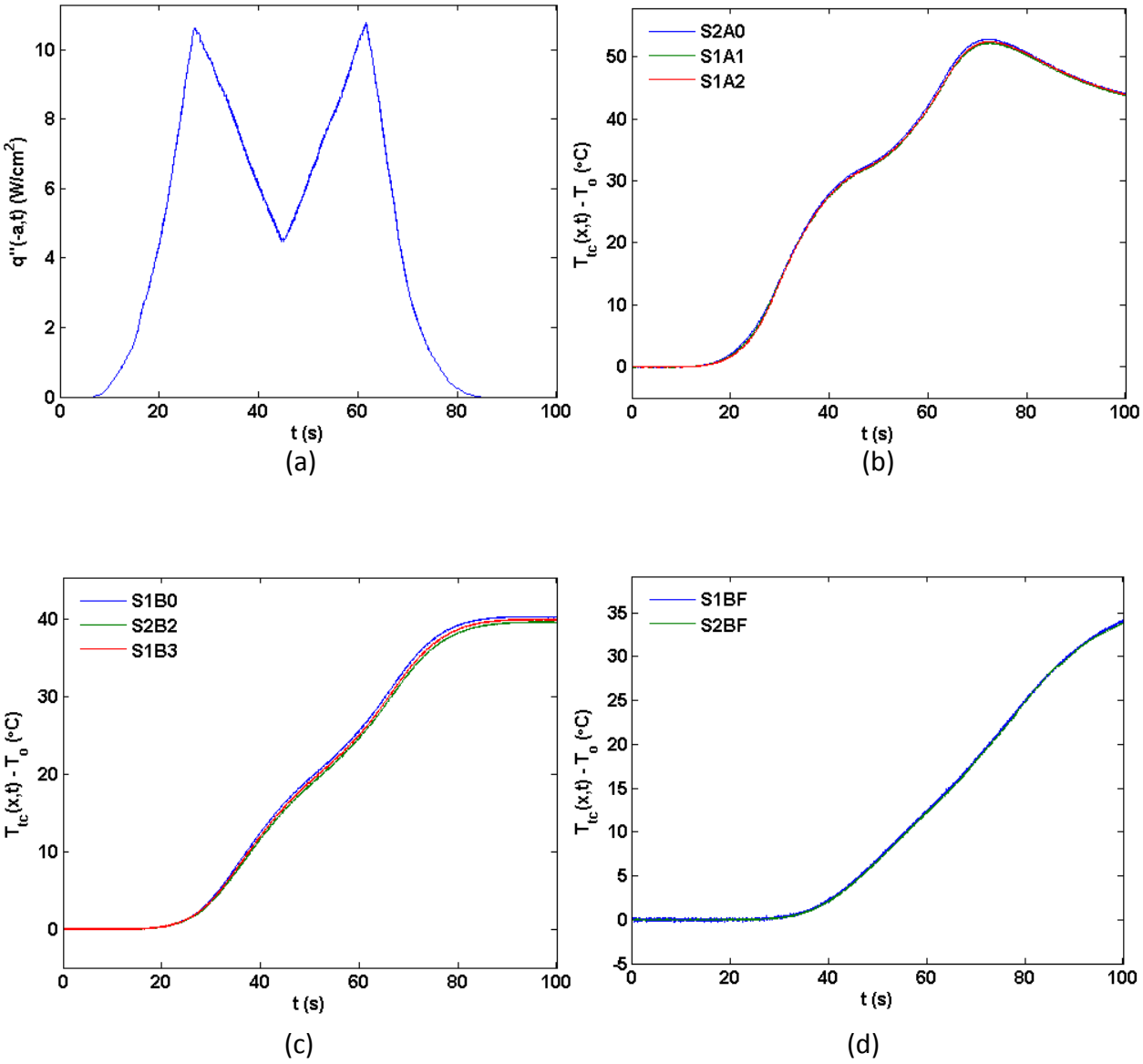

Figure 3.10. AlRun4 data - (a) Measured heat flux, (b) A-depth thermocouple temperature histories, (c) B-depth thermocouple temperature histories and (d) Back-face thermocouple temperature histories. The probe locations (x,y) are listed in Table C.3 in Appendix C.

From Figures 3.7 to 3.10 one can observe further improvements in the closeness of temperature responses at similar depths. A large improvement in performance can be seen especially at the S2A0 probe location. The S2A0 responses clearly show a faster take-off than the Mica Runs and are the highest recorded temperatures. This can be attributed to the uniform spreading effect of the Alumina layer. The higher thermal conductivity of Alumina allows the incident heat flux to spread relatively easier resulting in a more uniformly distributed heat flux in space entering the slab surfaces. Another potential contributor for the more physically consistent performance of S2A0 can be the minute readjustment in positioning of the nichrome heater during reassembly. It is possible that S2A0 happened to lie beneath the small gaps between the heater strips during the Mica runs. A slight shifting in the positioning of the heater would have caused S2A0 to align directly underneath one of the strips of the heater, thus producing a higher temperature response during the Alumina runs. The back-face symmetry continues to be highly favorable and once again, safely permits the halving of the total supplied power to determine the power input to each slab.

3.5 CHAPTER SUMMARY

The construction and working of the experimental setup utilized for data collection was explained. The need for making revisions to the setup was justified. The procedure followed for conducting experimental runs was described. The collected experimental data were shown to adhere very well to the underlying assumptions of the calibration integral equation method. Having established the pedigree of the experimental data, we can now proceed to demonstrate the working of the one-probe and two-probe calibration integral equation methods for resolving the IHCP.

CHAPTER 4. RESULTS AND DISCUSSION

4.1 ONE-PROBE CALIBRATION INTEGRAL METHOD

To recap, the work published by Elkins et al. in [7] details a treatment of the one-probe calibration method as applied to a semi-infinite domain. The subsequent studies conducted by Chen [9] extend the generality of the concept to a finite-width domain with a constant convection boundary condition at the back surface (same heat transfer coefficient for all runs). In [9], the optimal regularization parameter γ was determined via residual analysis by calculating the normalized square-root of the time running variance of the local residual function. The optimal regularization parameter was determined a posteriori since residual analysis is possible only after the inverse prediction of the surface heat flux. This meant that the optimal value could possibly vary with different real (unknown) runs. In this work, akin to the methods in described in [7], an alternate methodology is proposed based on the technique of calculating the signal-to-noise ratio of the calibration temperature data to establish an optimal band for the choice of γ.

4.1.1 Data Interrogation and Pre-processing

Assessment of Signal Strength – The success of the physics-based calibration methodology to resolve the IHCP relies exclusively on the calibration run stage. The calibration run(s) must be chosen so as to ensure the best possible inverse prediction. The eight experimental runs considered for this study require examination to identify those qualified for allocation as potential calibration runs. This determination plays a decisive role in the regularization scheme being implemented. Since the future-time regularization scheme will be used for the one-probe calibration method, gauging the strength of the 'signal' offered by each run provides a good basis for this examination. Before introducing the concept of the signal, pertinent background information is provided for ease of understanding. Borrowing from Chapter 2, we start by re-stating as Eq. (4.1), the conventional one-probe calibration integral equation after the incorporation of the future-time regularization scheme given by Eq. (2.14).

$$q''_{run,\gamma}(0,t) = \frac{1}{C_\gamma}\left[f(t+\gamma) - \int_{u=0}^{t} q''_{run,\gamma}(0,u)T_{cal}(b,t+\gamma-u)du\right], \quad t \in [0, t_{max}-\gamma]. \tag{4.1}$$

It must be emphasized again that all the temperatures appearing in the calibration integral equations represent 'rise' above the initial temperature value. As a reminder, Eq (4.1) can be applied to a two-layer domain by replacing $q''_{run,\gamma}(0,t)$ with $q''_{run,\gamma}(-a,t)$, where a is the thickness of the first layer [6]. The driver in Eq. (4.1) is the denominator term C_γ which is merely the integral w.r.t. time of the calibration temperature up to the specified value of γ, as shown in Eq. (2.13b). It is a constant which is directly proportional to the value γ, and its action is to scale the value of the bracketed terms in Eq. (4.1). Equation (4.1) is analogous to forward time differentiation (time rate of change). A small denominator would amplify the difference in the two terms of the numerator to produce large oscillations and an unstable prediction. Stability is attained by allowing the denominator to reach a sufficiently large value that damps out the oscillations. With any further increase in C_γ, the influence of the regularization model starts to dominate the solution, resulting in a loss of physics. It follows that the choice of γ should be such that maximum retention of physics is ensured along with stability.

In the work previously published by Elkins et al. [7], the denominator C_γ of Eq. (4.1) was considered as the signal and $\sigma\gamma$ was treated as the noise, where σ is the standard deviation of the lead calibration temperature data. The signal-to-noise ratio was then evaluated. With this definition of the signal-to-noise ratio, it is observed that the 'ratio' increases with increasing γ. A slight modification to this approach lends better insight into understanding the role of the signal-to-noise ratio in assessing the signal strength. The signal is now redefined as the running mean of the calibration temperature, denoted by $D(\gamma)$ per Eq. (4.2).

$$D(\gamma) = \frac{1}{\gamma}\int_{u=0}^{\gamma} T_{cal}(b,\gamma-u)du = \frac{C_\gamma}{\gamma}, \quad \gamma \in (0, t_{max}-t_{ON}]. \tag{4.2}$$

The noise is now denoted merely by σ, lending more physical meaning based on the fact that the noise level in a thermocouple temperature response practically stays constant. As observed previously in [7], the time at which a unity signal-to-noise ratio was achieved provided a lower bound γ_{min}on the choice of γ. To minimize the influence of the regularization model, γ_{min} should be as small as possible. This implies that: (i) the calibration test run must result in the

quickest and strongest temperature response at 'A depth' TC probes; and (ii) the TC probe with the strongest temperature response among 'A depth' probes must be selected as the calibration TC data.

As seen from Figures 3.3(b) – 3.10(b), thermocouple S2A0 (x=b=6.47mm) consistently outperforms the other A-Depth thermocouples, in terms of take-off and more so the maximum temperature recorded. Therefore, throughout the analyses presented in this chapter, the response of thermocouple S2A0 is considered as the x=b probe temperature. Before the calculation of the signal $D(\gamma)$, it is important to clarify that the S2A0 temperature data were first clipped up to the corresponding heat activation time t_{ON}. The t_{ON} values are listed in Table 3.1 for the Mica runs and in Table 3.2 for the Alumina runs. The shifted data were used in the calculation of the signal $D(\gamma)$. The strength of the signals obtained for each run can be judged with the aid of Figures 4.1(a-d) for the Mica runs and Figures 4.2(a-d) for the Alumina runs. The time at which the signal crosses the σ line marks a unity signal-to-noise ratio.

From Figures 4.1(a-d) we can see that for the Mica runs, McRun1 reaches a unity signal-to-noise ratio the fastest. This is to be expected since for McRun1 the imposed heat flux was held constant with the highest level. The heat flux reached its maximum value instantaneously, producing the strongest and quickest temperature responses. During McRun3 and 4, the heat flux was gradually ramped up to the peak value. This led to the propagation of a weak thermal front causing a relatively sluggish rise in the signal level as seen in Figure 4.1(b,c). The choice of McRun1 as the calibration run for the single-layer analysis is now justified. The remaining two natural convection runs McRun3 and McRun4 will be treated as the real (unknown) runs for inverse prediction.

For the Alumina runs, the fastest signal-to-noise ratio is attained in AlRun2 as seen in Figure 4.2(b). Despite AlRun1 having the highest level pulse heat flux, the higher level of noise delays the signal-to-noise ratio from reaching unity. AlRun2 will be considered as the calibration run for the two-layer analysis. As mentioned in Chapter 2, Alumina allows for high temperature operation which allows for longer duration heating. The higher temperature regime causes larger change in the thermal conductivity and specific heat values of the layers; and hence eroding the accuracy of the constant properties assumption. Apart from testing the one-probe calibration integral method for longer duration runs, the second motive is to test its performance for the inevitable scenario when the calibration and real runs have different back boundary conditions. The level of error in the inverse prediction is expected to increase with time as the effect of the difference in the back boundary conditions becomes more pronounced at the probe site and also due to the sequential nature of the future-time regularization

scheme. Accordingly, for the real run case, AlRun4 (natural convection) will be chosen for the first motive and AlRun3 (forced convection) for satisfying the second motive of the two-layer calibration analysis.

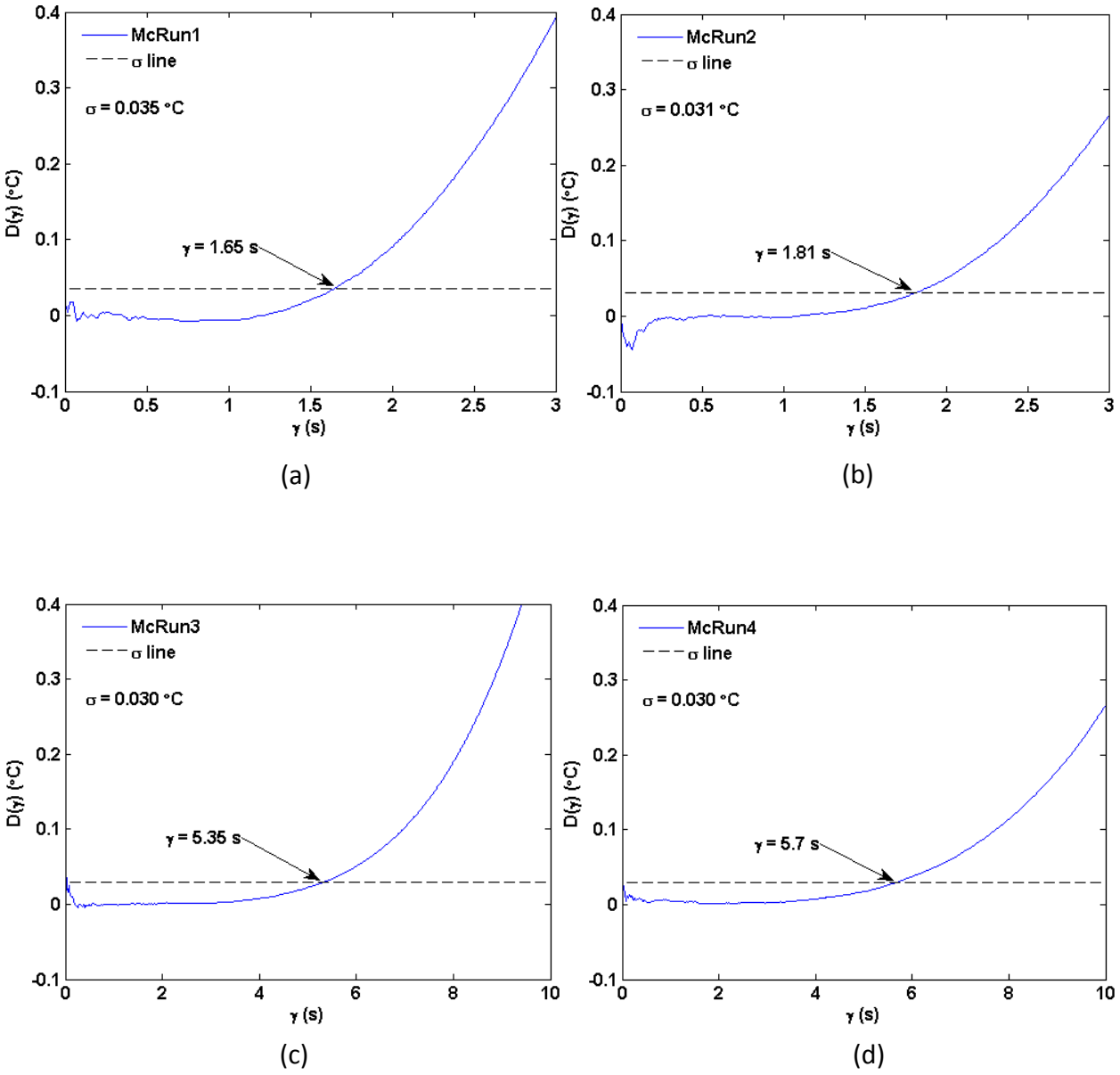

Figure 4.1. Plot of signal $D(\gamma)$ versus γ for, (a): McRun1, (b): McRun2, (c): McRun3 and (d): McRun4.

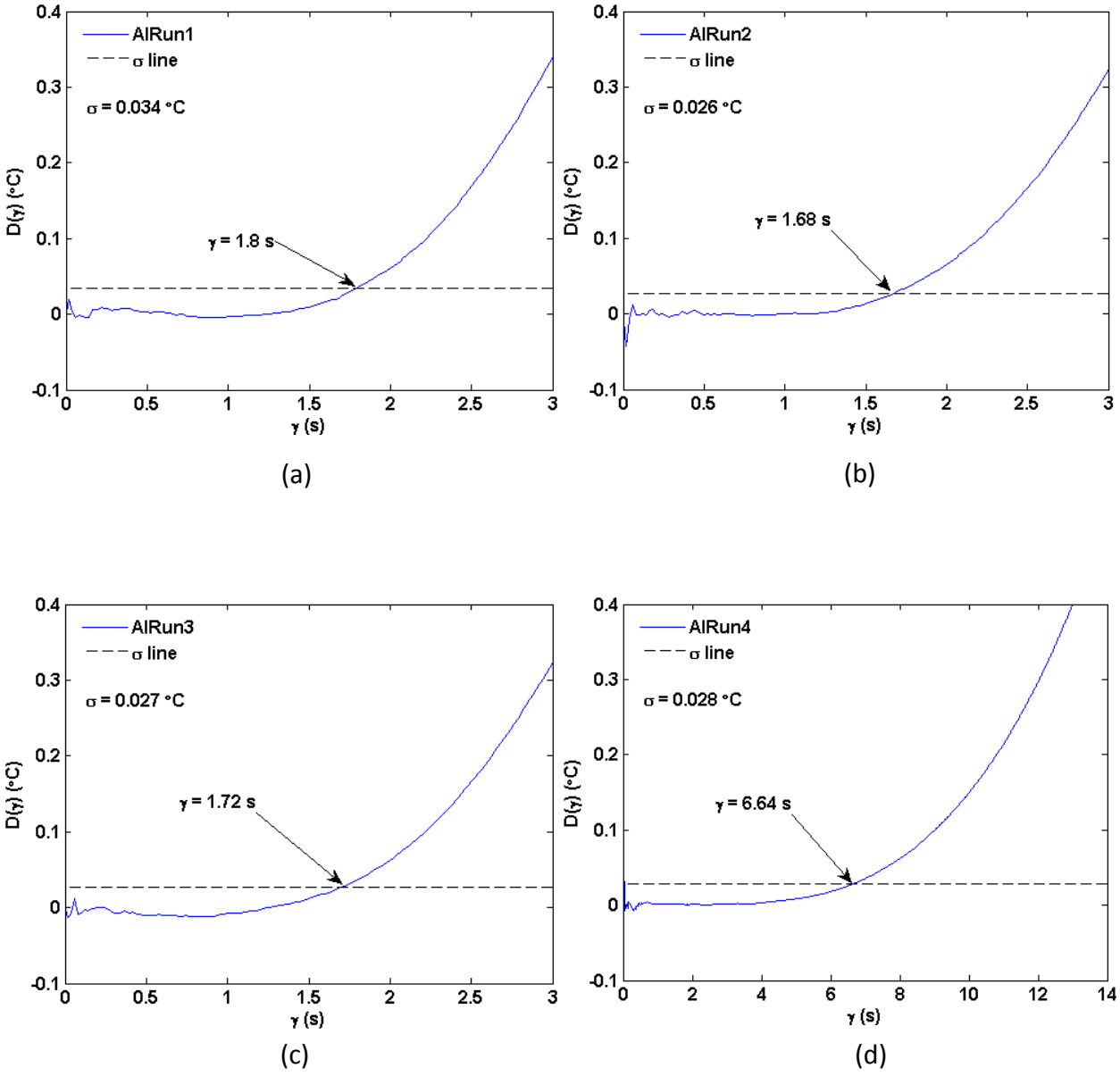

Figure 4.2. Plot of signal $D(\gamma)$ versus γ for, (a): AlRun1, (b): AlRun2, (c): AlRun3 and (d): AlRun4.

Test Case Nomenclature - Test cases will be referred to using the nomenclature 'yPTCz', where 'y' stands for the no. of probes needed in the calibration method, 'P' stands for 'probe', 'TC' is the abbreviation for 'Test Case' and 'z' denotes the Test Case number. For example, Test Case 2 for the one-probe calibration method will be denoted as '1pTC2' whereas '2pTC1' should be read as Test Case 1 for the two-probe calibration method. The test cases considered for the one-probe calibration integral equation method are listed in Table 4.1.

Table 4.1. Overview of Test Cases considered for One-probe Analysis.

Test Case	Calibration Run	Real Run
1pTC1	McRun1	McRun3
1pTC2	McRun1	McRun4
1pTC3	AlRun2	AlRun4
1pTC4	AlRun2	AlRun3

Estimation of heat activation time t_{ON} for the selected real runs – The knowledge of the heat activation time t_{ON} in the 'unknown run' is required to determine the amount of lead data available. As mentioned before, the lead data is utilized for determining the initial temperature T_o and the noise level σ of the measured temperature history. Once the initial temperature is known, it is subtracted from the real run temperature data to determine $T_{tc}(b,t) - T_o$ as required by the calibration integral. During the calibration test, the heat activation time t_{ON} is obtained from the measured heat flux. However, in practice, for the real run case the only available data is the measured temperature. Without the knowledge of the accompanying heat flux, the precise heat activation time t_{ON} cannot be determined. Therefore, a scheme for estimating t_{ON} for the real run cases will now be presented. The 'A-depth' temperature data presented in Figures 3.3(b) to 3.10(b) show the departure from the initial temperature at a certain time for each TC probe. This departure time is a combination of the actual heat activation time t_{ON} plus the experimental penetration time t_p that is required for the thermal front to reach the TC probe in a detectable manner. Recall that thermocouple S2A0 (b = 6.47 mm) has been chosen for analysis. The departure time is interpreted as the time needed for a departure from a known threshold or datum, which is normally the initial temperature T_o. Since T_o is unknown, a procedure must be devised to extract a good approximation of the initial temperature from the temperature data. For this purpose, the running average of the measured 'run' data is calculated via

$$T_{tc,avg}(b,t) = \frac{1}{t}\int_{u=0}^{t} T_{tc}(b,u)du \ , \qquad t \in (0, t_{max}]. \tag{4.3}$$

The difference $T_{tc}(b,t) - T_{tc,avg}(b,t)$ is then formed. This produces a 'rise-above-initial' term but in a running average sense. The plot of this term (not shown) against time displayed initial noisy behavior around zero followed by a departure, but a clear datum could not be determined. Further processing is hence needed. Accordingly, the metric $\beta(b,t)$ is then calculated by finding the running average of the absolute value of $T_{tc}(b,t) - T_{tc,avg}(b,t)$ as

$$\beta(b,t) = \frac{1}{t}\int_{u=0}^{t} \left|T_{tc}(b,u) - T_{tc,avg}(b,u)\right|du \, , \qquad t \in (0, t_{max}]. \tag{4.4}$$

The averaging process smoothens out the noise and the absolute value prevents the accumulation of negative values from unnecessarily delaying the departure time. The plot of $\beta(b,t)$ versus time as seen in Figures 4.3(a,b) to 4.6(a,b) shows a distinct monotonic rise after a certain time. This time is the cumulative effect of lead time, diffusion delay, sensor delay and departure from the noise level σ of the data. The exact time at which this occurs is, however, not clearly determined from the plot of $\beta(b,t)$ alone, since the initial bias like behavior cannot be quantified. Since the observed bias is relatively flat, the derivative of $\beta(b,t)$ w.r.t. time provides a fixed datum of zero, and a distinct time value beyond which the slope of $\beta(b,t)$ stays perpetually positive. The derivative $\mathrm{d}\beta(b,t)/dt$ was calculated by central differences and is plotted in Figures 4.3(c,d) to 4.6(c,d). The point at which $\mathrm{d}\beta(b,t)/dt > 0 \; \forall \; t$ marks the departure time t_β of a given real run temperature response. The heat activation time for the real runs can now be estimated with the knowledge of the experimental penetration time t_p of the accompanying calibration temperature data. In addition to the cumulative effects mentioned before, t_β contains some numerical delay due to the various integration/differentiation processes. Therefore, using a factor of safety of 2, two penetration times ($2t_p$) is subtracted from t_β to arrive at the estimated heat activation time. Once t_{ON} has been estimated, the arithmetic mean of the temperature data up to t_{ON} provides a good estimate of the required initial temperature T_o. Table 4.2 shows that the actual and estimated values of T_o are the same up to four significant figures. Table 4.2 also shows the different time values considered in this analysis.

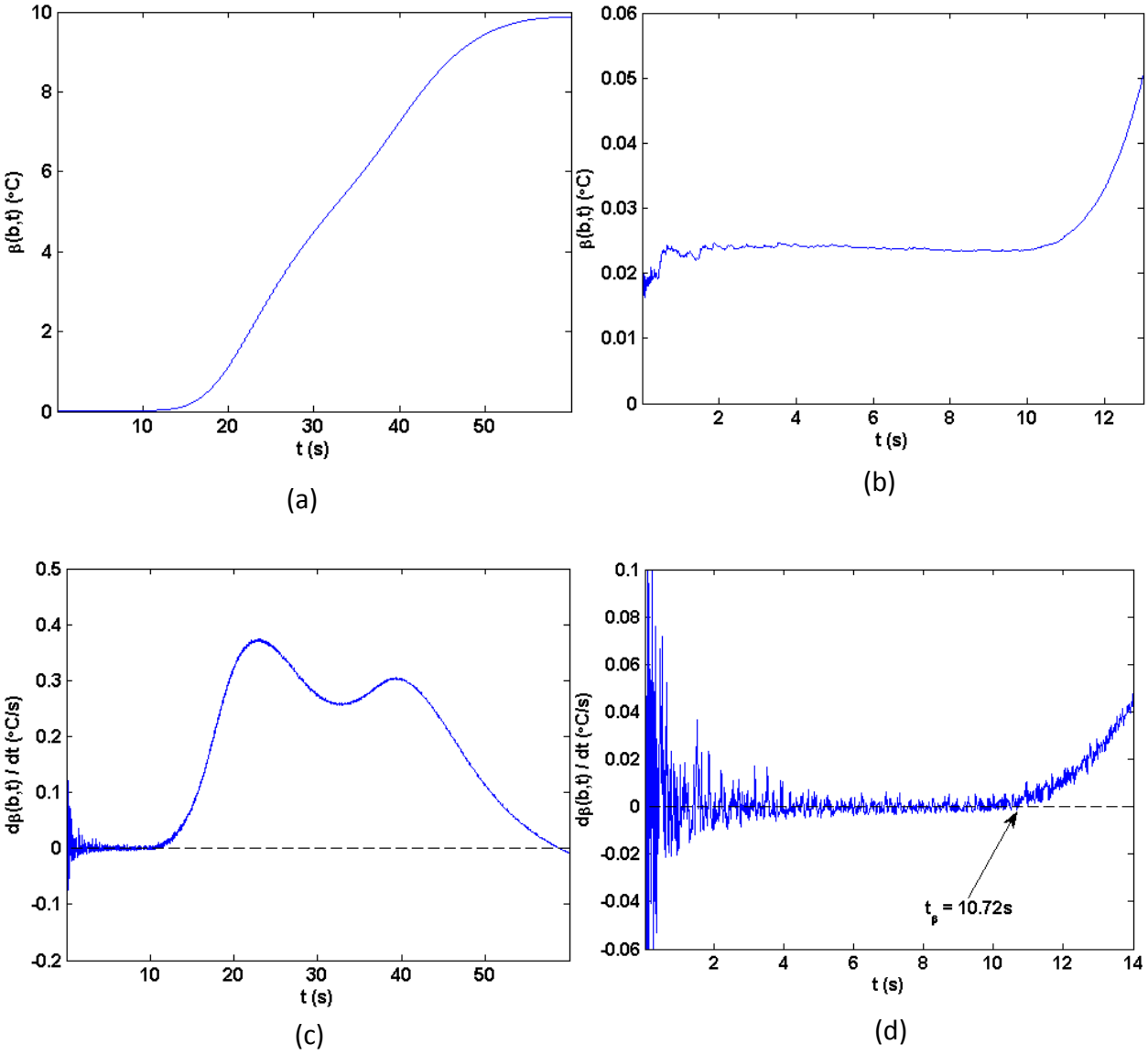

Figure 4.3. Metrics for estimation of t_{ON} for McRun3; (a) $\beta(b,t)$ versus t, (b) $\beta(b,t)$ versus t zoomed into region of interest, (c) $\mathrm{d}\beta(b,t)/dt$ versus t and (d) $\mathrm{d}\beta(b,t)/dt$ versus t zoomed in to show t_β = 10.72 s .

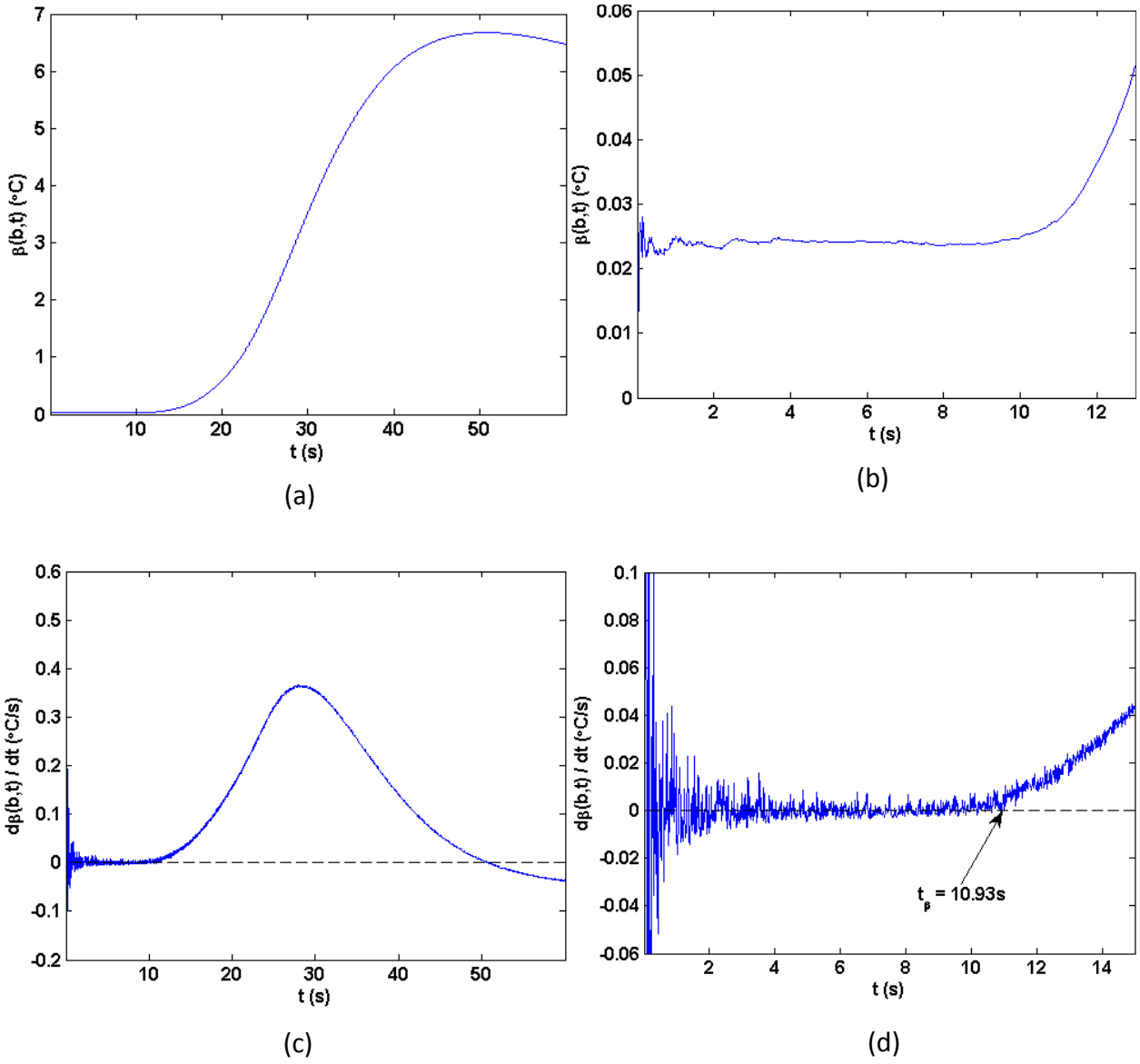

Figure 4.4. Metrics for estimation of t_{ON} for McRun4; (a) $\beta(b,t)$ versus t, (b) $\beta(b,t)$ versus t zoomed into region of interest, (c) $\mathrm{d}\beta(b,t)/dt$ versus t and (d) $\mathrm{d}\beta(b,t)/dt$ versus t zoomed in to show t_β = 10.93 s.

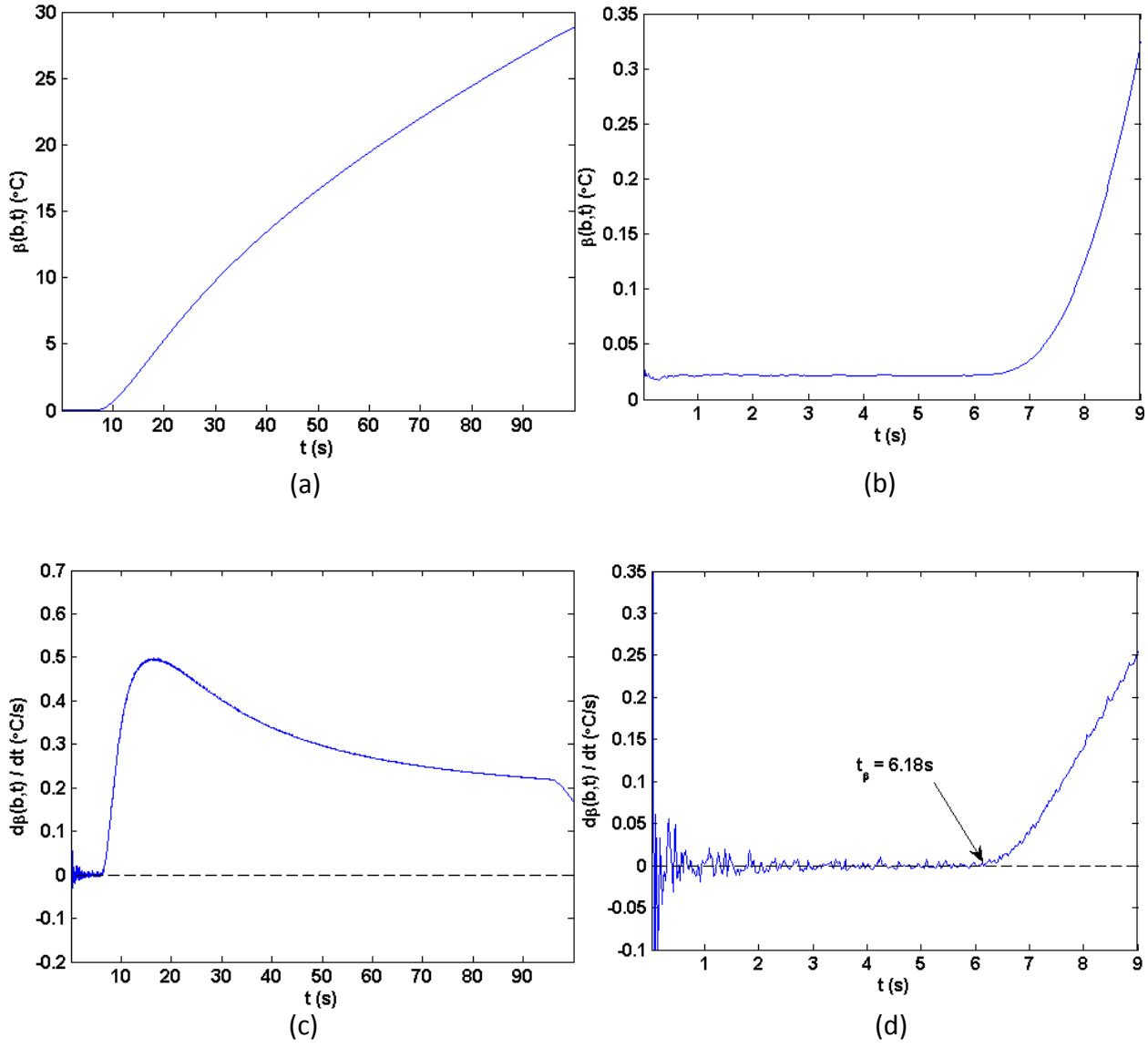

Figure 4.5. Metrics for estimation of t_{ON} for AlRun3; (a) $\beta(b,t)$ versus t, (b) $\beta(b,t)$ versus t zoomed into region of interest, (c) $\mathrm{d}\beta(b,t)/dt$ versus t and (d) $\mathrm{d}\beta(b,t)/dt$ versus t zoomed in to show t_β = 6.18 s.

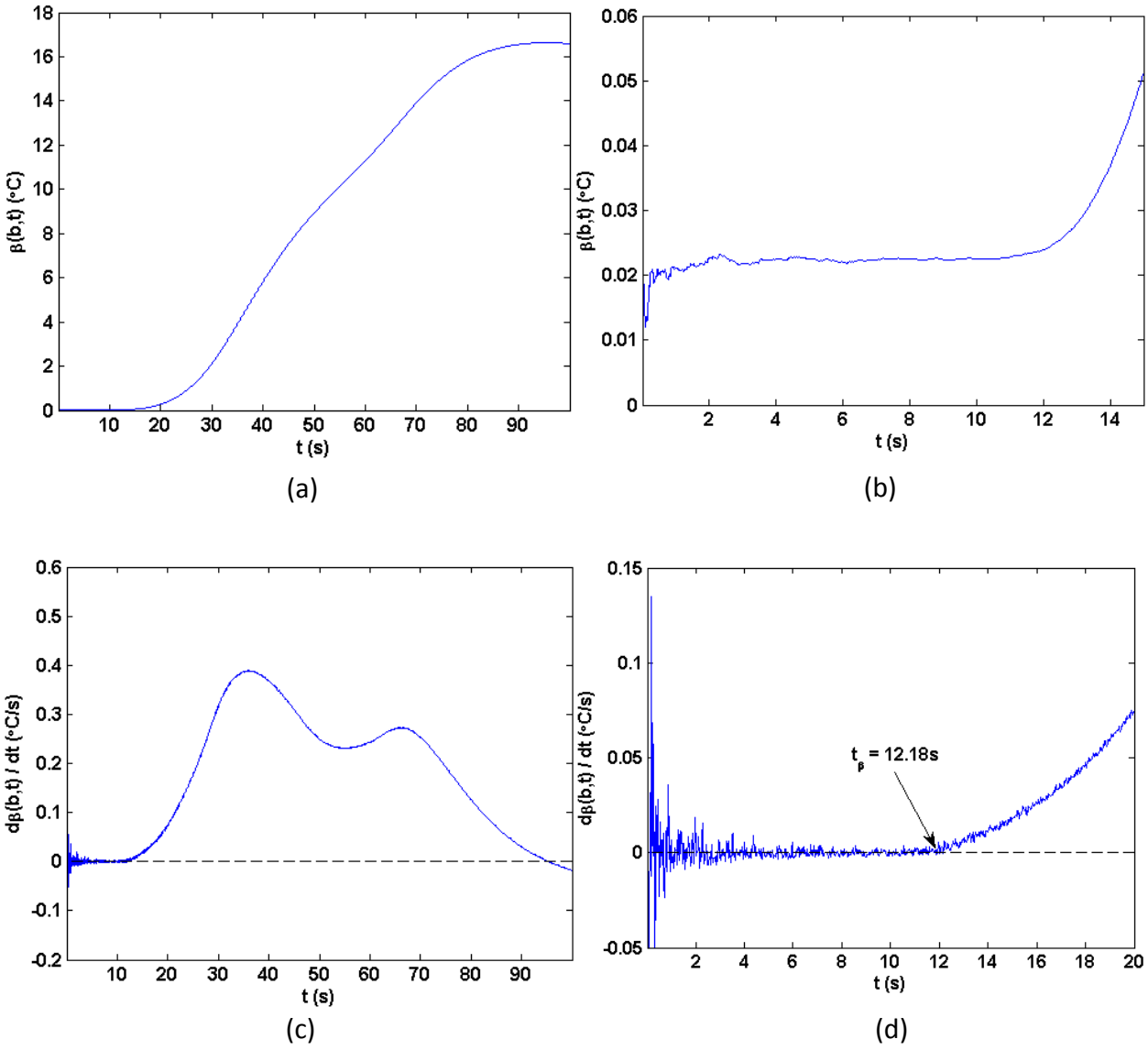

Figure 4.6. Metrics for estimation of t_{ON} for AlRun4; (a) $\beta(b,t)$ versus t, (b) $\beta(b,t)$ versus t zoomed into region of interest, (c) $\mathrm{d}\beta(b,t)/dt$ versus t and (d) $\mathrm{d}\beta(b,t)/dt$ versus t zoomed in to show t_β = 12.18 s.

Table 4.2. Time values required for the estimation of the heat activation time t_{ON} of the 'unknown' runs. Also shown are the actual and estimated initial temperatures T_o for the 'unknown' runs. Experimental penetration time t_p is obtained from the accompanying calibration run as listed in Table 4.1.

Real Run	t_p (s)	t_β (s)	Est. t_{ON}* (s)	Actual t_{ON} (s)	Est. T_o (°C)	Actual T_o (°C)
McRun3	1.55	10.72	7.62	6.52	22.367	22.368
McRun4	1.55	10.93	7.83	5.93	22.778	22.778
AlRun3	1.57	6.18	3.04	5.03	22.467	22.467
AlRun4	1.57	12.18	9.04	6.70	22.432	22.432

*=$t_\beta - 2t_p$

Elusive Search for Optimum Regularization Parameter. Determination of an optimal value for the regularization parameter is under extensive research and is an ongoing process. [1,6,7,9,21-24,27,30,31,35,41]. In the past studies on the future time regularization scheme applied to the physics-based calibration methodology [6,7,9], the goal was to identify a singular value as the optimum regularization parameter based on certain metrics. However, the robust nature of the one-probe calibration method, as will be demonstrated in the subsequent prediction results, suggests the establishment of an optimal 'band' for the selection of γ. The lower bound γ_{min}, as shown earlier in [7], is set by the time at which a unity signal-to-noise ratio is attained. The lower bound puts the future-time regularization scheme on the cusp of stability. Maximum retention of the original physics in the early segment of the transient is ensured at the cost of large oscillations as time progresses. A confidence level of σ translates to 68.3% certainty that the signal has reached an adequately strong level. By this rationale, it is proposed that a confidence level of 4 σ would indicate 99.99% certainty in the strength of the signal. It follows that the time required for the signal $D(\gamma)$ to cross the 4 σ noise level establishes an upper bound γ_{max} on the choice of γ. The inverse results will show that a choice of γ where $\gamma_{min} < \gamma < \gamma_{max}$, produces highly favorable resolutions of the net surface heat flux. If further reduction in oscillations is desired, the upper bound γ_{max} should be picked as the value of γ. An optimal band provides the necessary flexibility for choosing γ when different real run cases with varying levels of noise need to be resolved. This method intends to be a self-sufficient means of optimal regularization in that an optimal band capable of handling any real run data is known a priori, i.e., only calibration temperature data is required for determination of the optimal band. The optimal bands obtained for the selected calibration runs are shown in Figure 4.7(a,b).

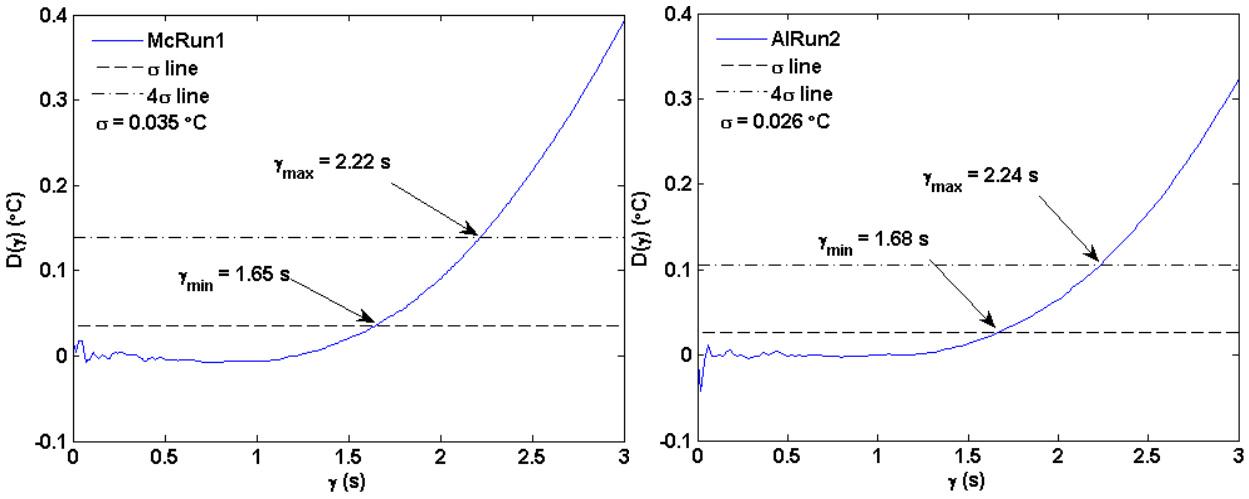

Figure 4.7. Establishment of optimal range of future time parameter γ for selected calibration runs; (a) McRun1 and (b) AlRun2.

4.1.2 Inverse Results

For the single-layer analysis, test cases 1pTC1 and 1pTC2, Mica was used as electrical insulation. The single-layer analysis disregards the effect of the additional mica layer. It is possible that the net heat flux $q''(0,t)$ actually incident on the stainless steel slab surface may differ slightly from the heat flux provided by the source (nichrome heater). It is shown in Appendix E that the presence of mica has no significant effect on the net surface heat flux $q''(0,t)$, permitting the measured heat flux to be used directly in the calculations.

The results obtained for the four test cases will now be analyzed.

1pTC1

As a pre-test diagnostic, to determine how accurately the data satisfies the one-probe calibration integral equation as per Eq. (2.8a), the RHS $f(t)$ and the LHS $g(t)$ of Eq. (2.8a) are calculated and compared.

The nature of the 'base residual function' $r(t)$, given by Eq. (4.5), and defined as the difference between the RHS and LHS of Eq. (2.8a), acts as a precursor to the quality of the inverse

prediction that can be expected of the data. It gives a measure of the extent by which the equality of Eq. (2.8a) is violated by the experimental data.

$$r(t) = f(t) - \int_{u=0}^{t} q''_{run}(0,u) T_{cal}(b, t-u) du \ , \qquad t \in [0, t_{max} - t_{ON}]. \tag{4.5}$$

Figure 4.8(a,b) shows the comparison of the LHS and RHS along with the base residual function. Comparison of the scales of Figures 4.18(a) and (b) shows that the base residual is three orders of magnitude smaller than the LHS (or RHS). Another assessment can be made by comparing the max absolute value reached in each figure. In this case, we can see that the max absolute value of $r(t)$ is about 0.3% of that of $f(t)$. The two sides of Eq. (2.8a) are in good agreement with each other. We can thus expect a good quality inverse prediction.

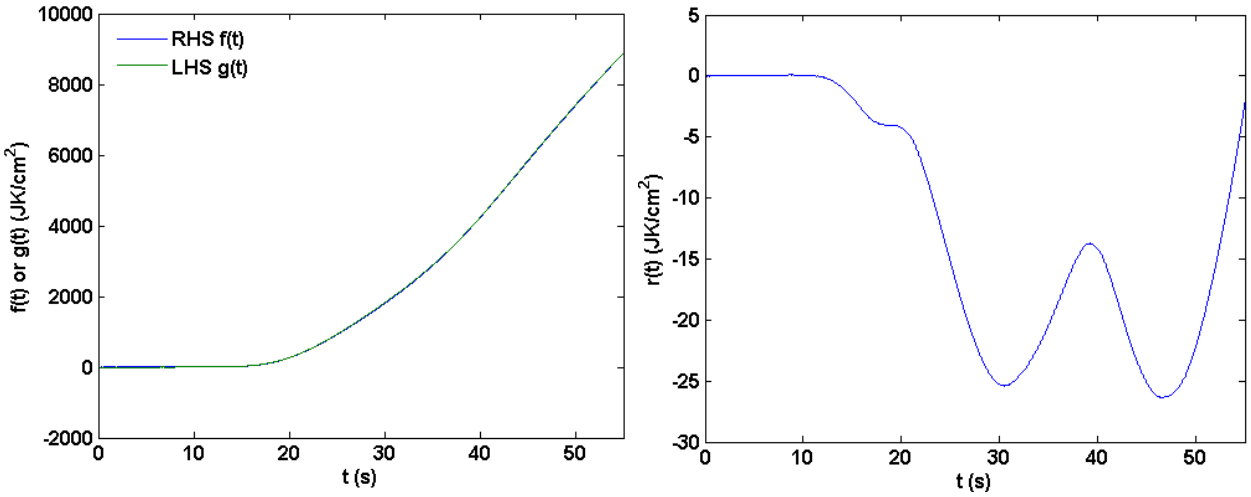

(a) (b)

Figure 4.8. Pre-test diagnostic plots for 1pTC1; (a) Comparison of LHS and RHS of Eq. (2.8a) and (b) base residual function $r(t)$.

The predictions are now presented for different values of γ in Figure 4.9(a-d).

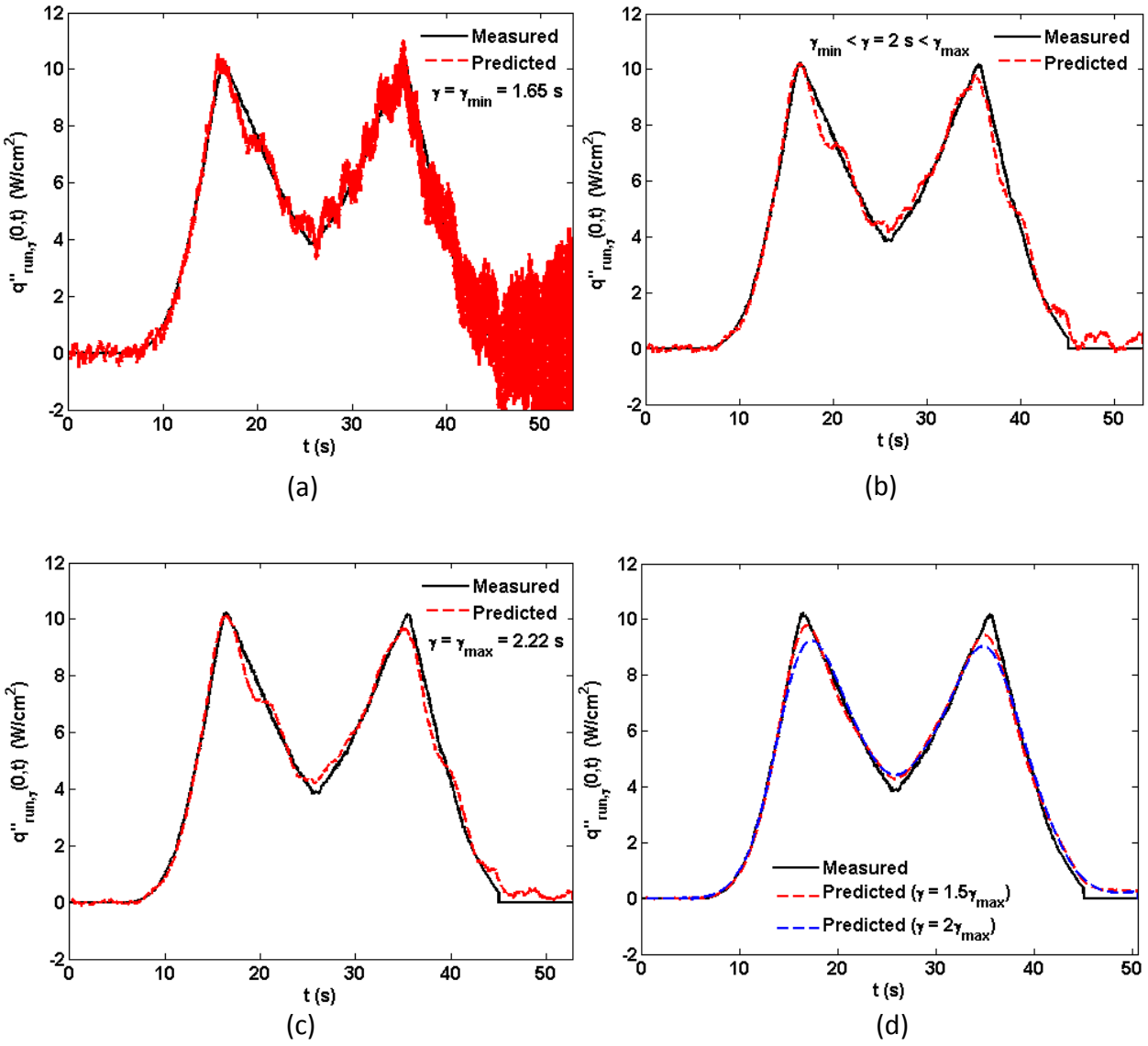

Figure 4.9. Inverse Results for 1pTC1 for (a) $\gamma = \gamma_{min}$, (b) $\gamma_{min} < \gamma < \gamma_{max}$, (c) $\gamma = \gamma_{max}$ and (d) $\gamma > \gamma_{max}$.

From Figure 4.9(a) we can observe that when $\gamma = \gamma_{min}$ the prediction is on the cusp of stability. The prediction stabilizes for the larger values of γ. The profile of the heat flux being sought poses a significant challenge to the regularization scheme in that the sharp peaks are invariably smoothed out at the expense of stability. The model appears to perform well in resolving the first peak regardless of the chosen value of γ. However, the second peak gets increasingly attenuated with increasing γ. The slight positive bias at the end of the second peak, or in other words, a slight over-estimation of the heat flux arises due to the negative nature of $r(t)$. The

model tries to maintain the equality of Eq. (2.8a), when hindsight reveals a negative valued base residual function.

The difference in the measured and predicted heat fluxes is calculated to form the error in prediction $\epsilon_q(t)$ as per Eq. (4.6a). The standard deviation $\sigma_{\epsilon q}$ of the error helps in quantifying the level of errors present for the whole time domain. The error during only the heating period $\epsilon_{q,heat}(t)$ is calculated as per Eq. (4.6b). The corresponding standard deviation $\sigma_{\epsilon q,heat}$ helps quantify the level of errors relevant to the heating period and ignores the oscillations present during the lead and post heating times.

$$\boldsymbol{\epsilon}_q(t) = q^{"}_{run}(0,t) - q^{"}_{run,\gamma}(0,t), \qquad t \in [0, t_{max} - t_{ON} - \gamma]. \tag{4.6a}$$

$$\boldsymbol{\epsilon}_{q,heat}(t) = q^{"}_{run}(0,t) - q^{"}_{run,\gamma}(0,t), \qquad t \in [t_{ON}, t_{OFF}]. \tag{4.6b}$$

The total energy input contained in the prediction E_γ is calculated as

$$E_\gamma = \int_{t=0}^{t_{max}-t_{ON}-\gamma} q^{"}_{run,\gamma}(0,t)dt, \quad t \in [0, t_{max} - t_{ON} - \gamma]. \tag{4.7}$$

The metrics for judging the quality of the predictions are presented in Tables 4.3(a) and 4.3(b).

Table 4.3(a). 1pTC1 – Inverse Prediction Metrics. E = 204.03 J/cm^2.

γ level	γ value (s)	$\sigma_{\epsilon q}$ (W/cm^2)	$\sigma_{\epsilon q,heat}$ (W/cm^2)	E_γ (J/cm^2)	E_γ/E
$\boldsymbol{\gamma = \gamma_{min}}$	1.65	0.915	0.628	206.77	1.013
$\boldsymbol{\gamma_{min} < \gamma < \gamma_{max}}$	2	0.345	0.381	206.55	1.012
$\boldsymbol{\gamma = \gamma_{max}}$	2.22	0.319	0.354	206.44	1.012
$\boldsymbol{\gamma = 1.5\gamma_{max}}$	3.33	0.242	0.259	206.21	1.011
$\boldsymbol{\gamma = 2\gamma_{max}}$	4.44	0.327	0.372	205.97	1.01

In Table 4.3(b) the symbol $q^{"}_{pk1}$represents the magnitude of the measured heat flux at the first peak. Accordingly, $q^{"}_{pk2}$ is the level of measured heat flux at the second peak (if present). Adding γ in the subscript indicates the corresponding predicted peak heat flux. The difference

in the times at which the peak occurs in the measured and predicted heat fluxes is denoted by $\Delta t_{pk1,\gamma}$ for the first peak and $\Delta t_{pk2,\gamma}$ for the second peak.

Table 4.3(b). 1pTC1 – Inverse Prediction Metrics. q''_{pk1}= 10.25 W/cm^2 @t = 16.41 s, q''_{pk2}= 10.18 W/cm^2 @t = 35.53 s

γ level	γ value (s)	$q''_{pk1,\gamma}$ (W/cm^2)	$\frac{q''_{pk1,\gamma}}{q''_{pk1}}$	$\Delta t_{pk1,\gamma}$ (s)	$q''_{pk2,\gamma}$ (W/cm^2)	$\frac{q''_{pk2,\gamma}}{q''_{pk2}}$	$\Delta t_{pk2,\gamma}$ (s)
$\gamma = \gamma_{min}$	1.65	10.56	1.03	-0.61	11.04	1.08	-0.12
$\gamma_{min} < \gamma < \gamma_{max}$	2	10.22	0.99	0.09	9.80	0.96	-0.38
$\gamma = \gamma_{max}$	2.22	10.14	0.98	- 0.13	9.71	0.95	-0.60
$\gamma = 1.5\gamma_{max}$	3.33	9.78	0.95	0.41	9.43	0.92	-0.48
$\gamma = 2\gamma_{max}$	4.44	9.43	0.92	0.8	9.04	0.88	-0.69

The metrics presented in Tables 4.3(a) and 4.3(b) are intended the show the effect of change in γ on the accuracy of the predictions. In practice, none of these metrics are available. Table 4.3(a) shows remarkable consistency in the conservation of total estimated energy input E_γ regardless of the chosen value of γ. The $\sigma_{\epsilon q}$ and $\sigma_{\epsilon q,heat}$ values show a decreasing trend with increasing γ up to $\gamma = 1.5\gamma_{max}$. The trend does reverse when $\gamma = 2\gamma_{max}$, indicating a high level of over-smoothing as reflected in Figure 4.9(d). Table 4.3(b) shows that for γ=2s (in the suggested band) the best ratios of the predicted peaks to the actual peaks (peak-1 ratio=0.99 with Δt=0.09s, and peak-2 ratio=0.96 with Δt=-0.38s) are obtained. It is important to remind the reader that the objective of the future-time regularization scheme is to stabilize the prediction with maximum retention of physics. With that in mind, staying within the proposed band of optimum γ values ensures both conditions are met satisfactorily.

1pTC2

Figure 4.10(a,b) shows the comparison of the LHS and RHS along with the base residual function. Comparison of the scales of Figures 4.10(a) and (b) shows that the base residual is now about two orders of magnitude smaller than the LHS (or RHS). By comparing the maximum absolute values we can see that the maximum absolute value of $r(t)$ has increased to about 0.67% of that of $f(t)$. The two sides of Eq. (2.8a) are still in good agreement with each other and a good quality inverse prediction is again expected.

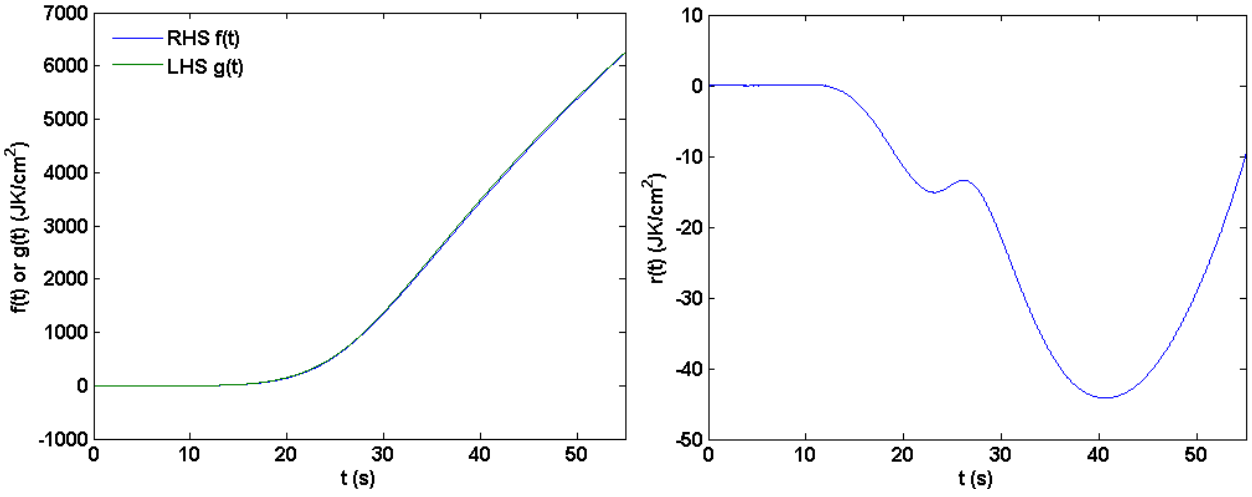

(a) (b)

Figure 4.10. Pre-test diagnostic plots for 1pTC2; (a) Comparison of LHS and RHS of Eq. (2.8a) and (b) base residual function $r(t)$.

The predictions are presented for different values of γ in Figure 4.11(a-d). The associated metrics are presented in Tables 4.4(a,b). From Figure 4.11(a) we can see the growth of oscillations similar to 1pTC1 but lesser in magnitude. The lower bound γ_{min} shows that the regularization model has just entered the stable region. The same suggested optimal band is shown to work very well for different real run cases.

Table 4.4(a) again shows a good conservation of energy independent of γ. Similar trends are observed in the $\sigma_{\epsilon q}$ and $\sigma_{\epsilon q,heat}$ values as in 1pTC1.

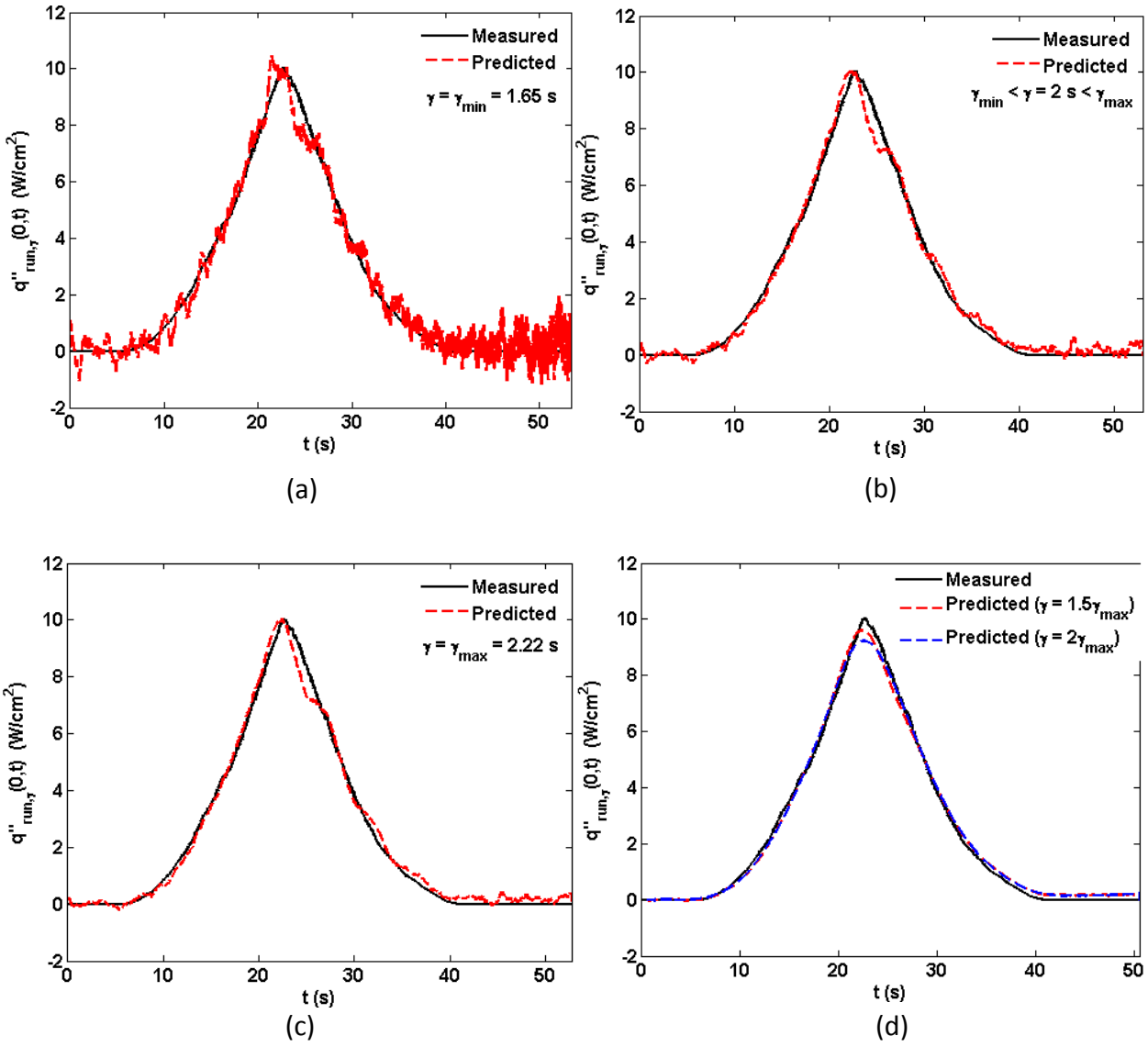

Figure 4.11. Inverse Results for 1pTC2 for (a) $\gamma = \gamma_{min}$, (b) $\gamma_{min} < \gamma < \gamma_{max}$, (c) $\gamma = \gamma_{max}$ and (d) $\gamma > \gamma_{max}$.

Table 4.4(a). 1pTC2 – Inverse Prediction Metrics. E = 128.39 J/cm^2.

γ level	γ value (s)	$\sigma_{\epsilon q}$ (W/cm^2)	$\sigma_{\epsilon q,heat}$ (W/cm^2)	E_γ (J/cm^2)	E_γ/E
$\gamma = \gamma_{min}$	1.65	0.453	0.439	130.92	1.02
$\gamma_{min} < \gamma < \gamma_{max}$	2	0.288	0.332	130.73	1.018
$\gamma = \gamma_{max}$	2.22	0.261	0.307	130.59	1.017
$\gamma = 1.5\gamma_{max}$	3.33	0.187	0.218	130.36	1.015
$\gamma = 2\gamma_{max}$	4.44	0.188	0.222	130.17	1.014

Table 4.4(b). 1pTC2 – Inverse Prediction Metrics. q''_{pk1}= 10.06 W/cm^2 @t = 22.66 s.

γ level	γ value (s)	$q''_{pk1,\gamma}$ (W/cm^2)	$\frac{q''_{pk1,\gamma}}{q''_{pk1}}$	$\Delta t_{pk1,\gamma}$ (s)
$\gamma = \gamma_{min}$	1.65	10.46	1.04	-1.17
$\gamma_{min} < \gamma < \gamma_{max}$	2	10.1	1.01	-0.51
$\gamma = \gamma_{max}$	2.22	10.04	0.99	-0.23
$\gamma = 1.5\gamma_{max}$	3.33	9.6	0.95	-0.33
$\gamma = 2\gamma_{max}$	4.44	9.23	0.92	-0.19

1pTC3

This test case marks the beginning of the two-layer calibration method analysis. All the data considered for the following test cases was generated with the Alumina setup. As mentioned before in Chapter 3, the data were downsampled to 50 Hz to save memory and computation time. In this test case a similar twin-peak heat flux profile is considered for resolution, albeit for a longer transient time of 99.98s. Measurement errors, numerical truncation and round-off errors accompanied by the inherent non-linearity of the physical system are expected to influence the resolved surface heat flux with increasing time.

Figure 4.12(a,b) shows the comparison of the LHS and RHS along with the base residual function $r(t)$. Comparison of the scales of Figures 4.12(a) and (b) shows that the base residual is two orders of magnitude smaller than the LHS (or RHS). A visibly larger deviation is seen in the comparison plot displayed in Figure 4.12(a). In this case, we can see that the max absolute value of $r(t)$ has now increased to about 1.15% of that of $f(t)$. The max absolute value of $r(t)$ for the previous two Mica test cases were about 0.3% and 0.67% of their respective *f(t).* The

effects of these larger discrepancies are seen in the predictions displayed in Figure 4.13(a-d). The associated metrics are given in Tables 4.5(a,b).

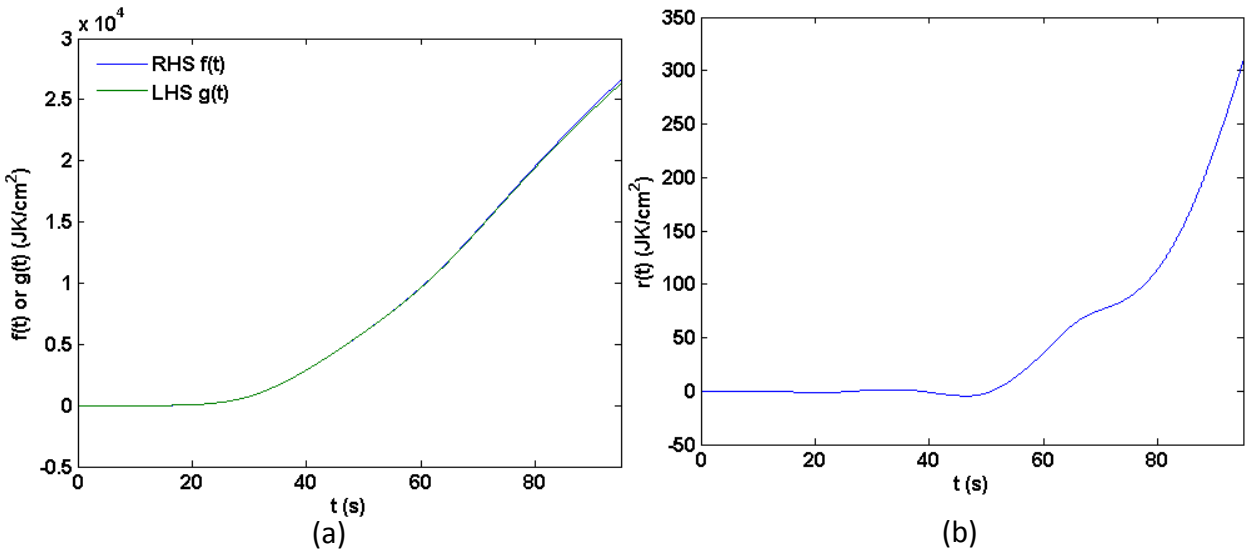

Figure 4.12. Pre-test diagnostic plots for 1pTC3; (a) Comparison of LHS and RHS of Eq. (2.8a) and (b) base residual function $r(t)$.

Consistent with the Mica test cases 1pTC1 and 1pTC2, the lower bound of γ puts the model on the cusp of stability. The oscillations seem to be more violent for the present case. Subsequent results for larger values of γ reveal a stable prediction with good resolution of the sharp peaks, especially the second peak. Also noticeable is a positive bias-like behavior towards the end, which is much more apparent when compared with 1pTC1 and 1pTC2. It is noted that the thermal conductivity of the Alumina (ADS-96R) plate is 26 W/(mK) at 20^{o}C and 12 W/(mK) at 400^{o}C. Clearly, the variable properties effect of Alumina begins to play an appreciable role as time progresses and temperature of the Alumina layer increases. Figure 4.13 supports this observation.

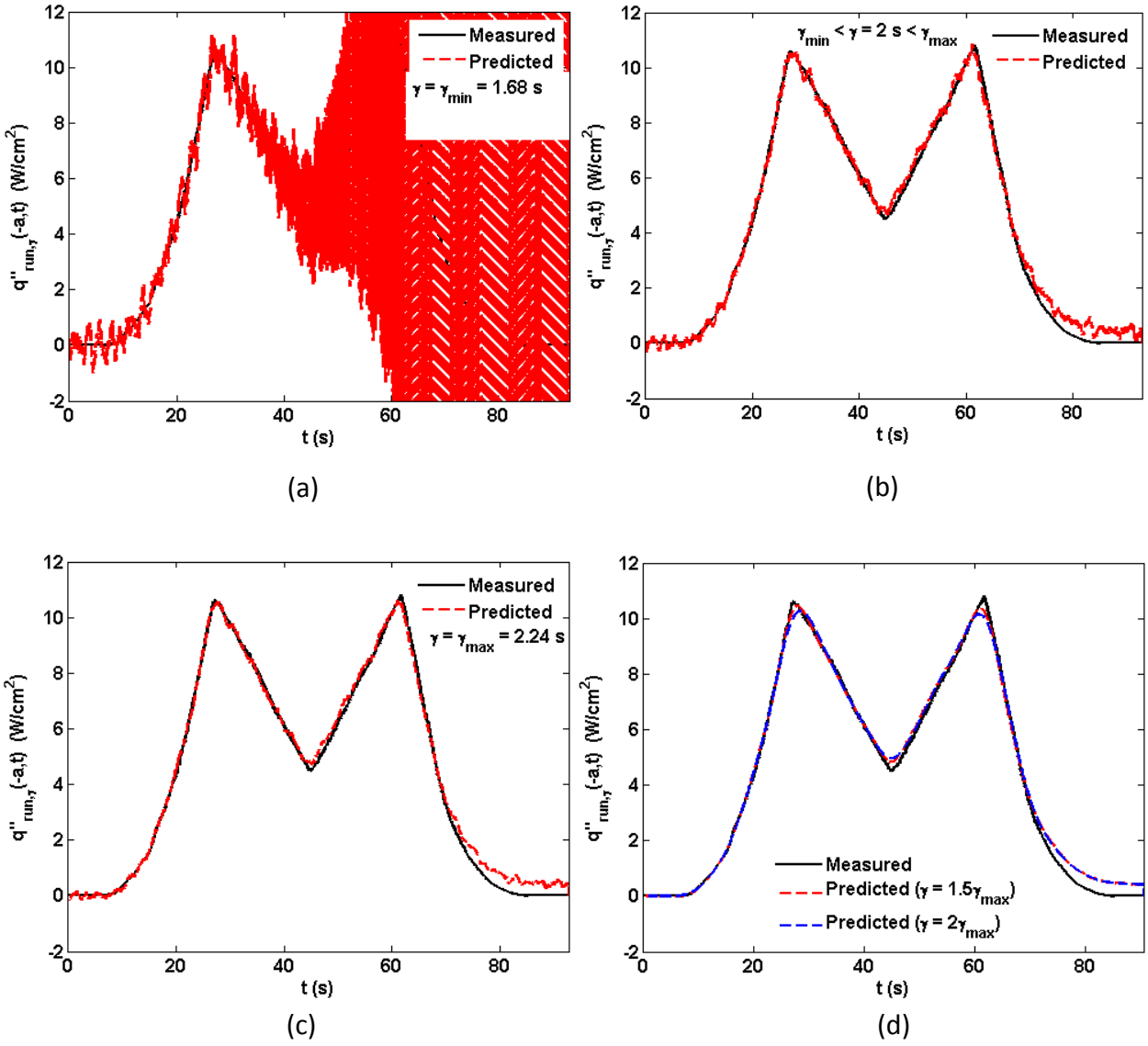

Figure 4.13. Inverse Results for 1pTC3 for (a) $\gamma = \gamma_{min}$, (b) $\gamma_{min} < \gamma < \gamma_{max}$, (c) $\gamma = \gamma_{max}$ and (d) $\gamma > \gamma_{max}$.

Table 4.5(a). 1pTC3 – Inverse Prediction Metrics. E = 404.91 J/cm^2.

γ level	γ value (s)	$\sigma_{\epsilon q}$ (W/cm^2)	$\sigma_{\epsilon q,heat}$ (W/cm^2)	E_γ (J/cm^2)	E_γ/E
$\gamma = \gamma_{min}$	1.68	93.38	37.62	421.53	1.041
$\gamma_{min} < \gamma < \gamma_{max}$	2	0.249	0.244	416.69	1.029
$\gamma = \gamma_{max}$	2.24	0.226	0.221	416.65	1.029
$\gamma = 1.5\gamma_{max}$	3.36	0.212	0.208	416.19	1.028
$\gamma = 2\gamma_{max}$	4.48	0.224	0.226	415.73	1.027

Table 4.5(b). 1pTC3 – Inverse Prediction Metrics. q''_{pk1}= 10.62 W/cm^2 @t = 27.1 s, q''_{pk2}= 10.8 W/cm^2 @t = 61.64 s.

γ level	γ value (s)	$q''_{pk1,\gamma}$ (W/cm^2)	$\frac{q''_{pk1,\gamma}}{q''_{pk1}}$	$\Delta t_{pk1,\gamma}$ (s)	$q''_{pk2,\gamma}$ (W/cm^2)	$\frac{q''_{pk2,\gamma}}{q''_{pk2}}$	$\Delta t_{pk2,\gamma}$ (s)
$\gamma = \gamma_{min}$	1.68	11.17	1.05	-0.58	- *	-	-0.42
$\gamma_{min} < \gamma < \gamma_{max}$	2	10.58	0.99	1	10.86	1.007	-0.66
$\gamma = \gamma_{max}$	2.24	10.57	0.99	0.76	10.62	0.983	-0.76
$\gamma = 1.5\gamma_{max}$	3.36	10.46	0.98	0.7	10.35	0.958	-0.9
$\gamma = 2\gamma_{max}$	4.48	10.27	0.96	1.32	10.14	0.939	-0.42

This can be attributed to the accumulation of various errors, but more so to the imbalance created by significantly different temperature levels attained during the calibration and real runs. The higher temperatures of the calibration run result in larger variations in the thermal properties of the host material. It also causes a relatively larger heat loss due to radiation from the back-surfaces and side walls, challenging the constraint of identical back-boundary conditions for the calibration and real runs.

The information provided by the metrics in Table 4.5a suggests a similar behavior as with the Mica test cases 1pTC1 and 1pTC2. Table 4.5b shows that the prediction for γ=2s again does an excellent job of capturing peak-1 (ratio=0.99) and peak-2 (ratio=0.983) values.

1pTC4

The motivation for presentation of this test case differs from the others in that it is designed specifically to demonstrate the breakdown of the one-probe calibration method. During both experimental runs considered for this case, namely AlRun2 and AlRun3, the active (heated) surface of the slabs was subjected to the same level of heat flux for equal durations. The only

difference between the two runs was the back-boundary condition. The back-surfaces of the slabs were cooled by natural convection for AlRun2 and forced convection for AlRun3. Such a scenario enables an easy correlation between the deviation in temperatures recorded by a particular thermocouple during the two runs, and the resulting deviation between the predicted and measured heat fluxes. The identical heating condition and the dissimilar back boundary condition during the two runs are displayed in Figure 4.14.

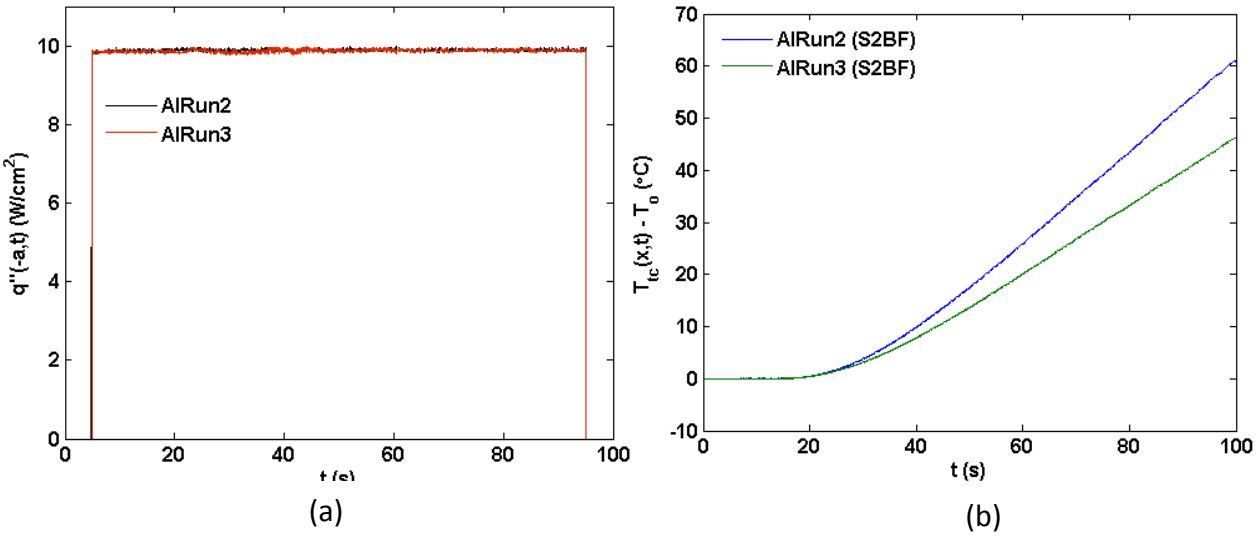

(a) (b)

Figure 4.14. (a) Comparison of imposed heat fluxes during AlRun2 and AlRun3 and (b) Comparison of back-face TC (S2BF) temperature responses showing the effect of dissimilar back boundary conditions.

Temperatures recorded by the S2A0 and S1B0 thermocouples are compared in Figure 4.15(a-d). The inclusion of S1B0 in this test case is explained by its location. It takes a certain amount of time for the heat front to propagate to the back-surface. Cooling due to natural (or forced) convection starts once the back-surface is penetrated. This information now back-propagates and is registered first by the probe site located closer to the back-surface. It follows that a comparison between the S1B0 temperature histories will reveal a larger deviation than the S2A0 temperature histories. Figure 4.15(b,d) shows an increasing deviation with time. The observed percentage deviations in temperature histories at these times are marked in Figure 4.15(b,d). In the S2A0 temperature comparison the observed deviation at t = 92.94 s was about 1% whereas in the comparison of the S1B0 temperature histories, the observed deviation at t = 89.44 s was approximately 2%.

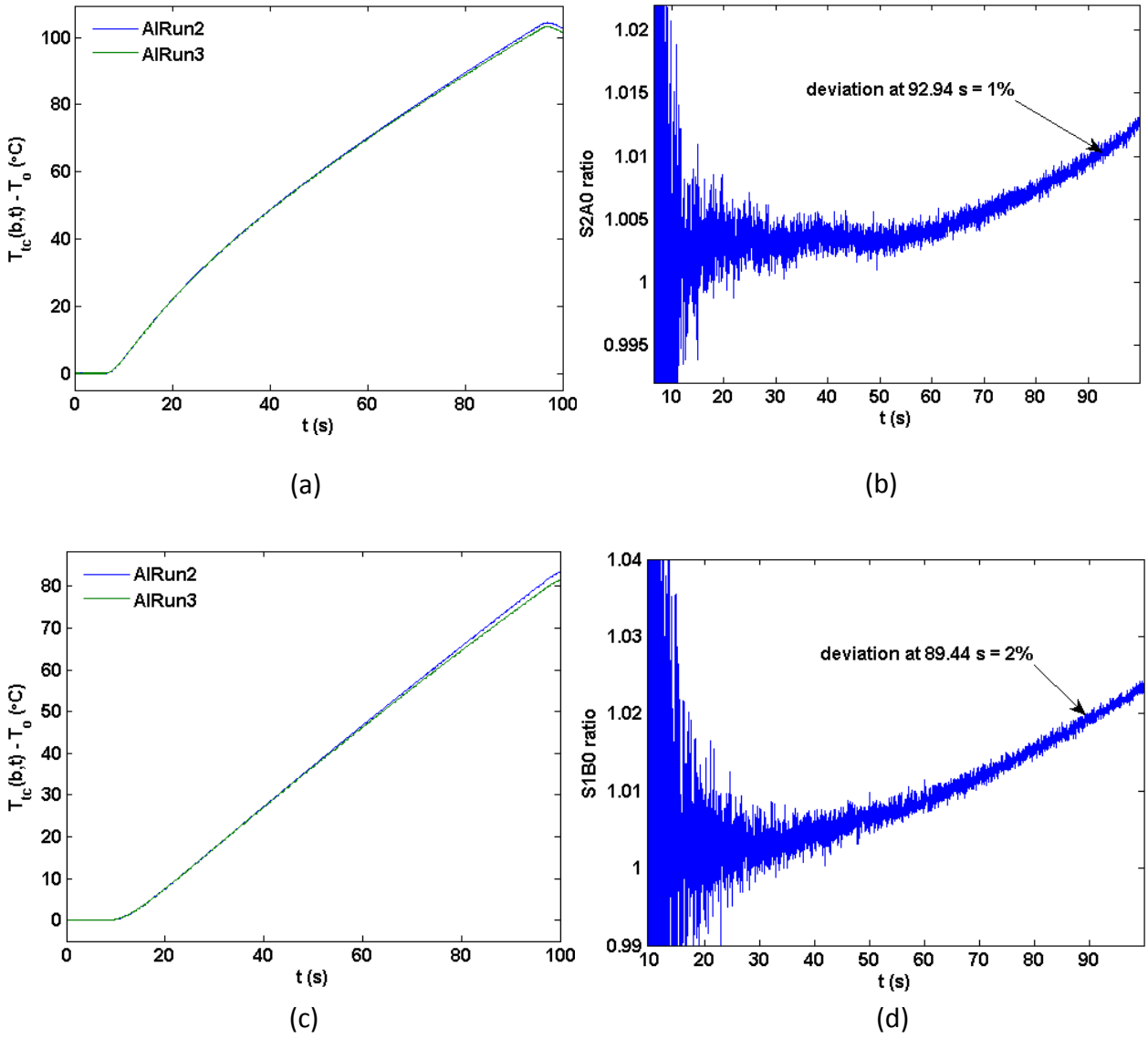

Figure 4.15. (a) Comparison of S2A0 temperature histories during AlRun2 and AlRun3, (b) Ratio of S2A0 temperature histories, (c) Comparison of S1B0 temperature histories during AlRun2 and AlRun3 and (d) Ratio of S1B0 temperature histories.

The maximum time available during the analysis is different from the maximum sampled time. It should be made clear that for this test case, both the calibration and real runs were clipped off their lead data. The heat activation times for both runs, as mentioned in Table 3.2, was 5.04s. In this case, the prediction using S2A0 temperature data is presented for γ = 2s. For the analysis using S1B0 temperature data, a suitable value of γ = 5.5s was chosen with the aid of

Figure 4.16. The two selected values of γ combined with the clipping of the data up to 5.04s, resulted in a maximum analysis time of 92.94s for the S2A0 case and 89.44s for the S1B0 case.

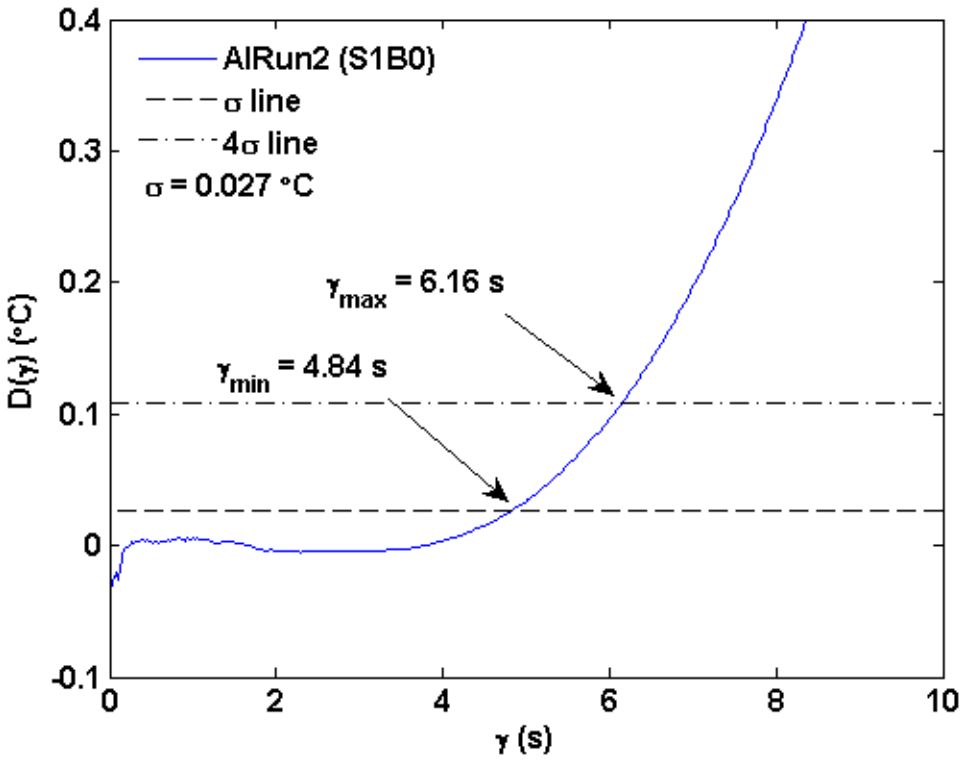

Figure 4.16. Establishment of optimum band for future-time regularization parameter γ using S1B0 temperature data of AlRun2 as calibration case.

The pre pre-test diagnostic plots and the predicted heat flux using the S2A0 probe data are presented in Figure 4.17(a,b,c). At time t=92.94s the ratio of $r(t)$ to $f(t)$, shown in Figure 4.17(a,b), is about -0.46%. The base residual, Figure 4.17(b), monotonically attains larger negative values as time progresses. Consequently, one should expect that the corresponding inverse solution, shown in 4.17(c), will exhibit an increasing level of under-prediction of the heat flux (4.1% at t=92.94s).

The pre pre-test diagnostic plots and the predicted heat flux using the S1B0 probe data are presented in Figure 4.18(a,b,c). At time t=89.44s the ratio of $r(t)$ to $f(t)$, shown in Figure 4.18(a,b), is about -1.1% which is about 2.4 larger than the S2A0 data case. Therefore, in this case one should expect even larger under-prediction of the heat flux (6% at t=89.44s). The

breakdown of the one-probe calibration method is clearly seen in Figure 4.18(c). The fact that the inverse prediction using S2A0 probe data shows as little as a 4.1% under prediction lends tremendous merit to the robustness of the one-probe calibration method. It is a giving method, capable of handling data corrupted by significant differences between the back-boundary conditions.

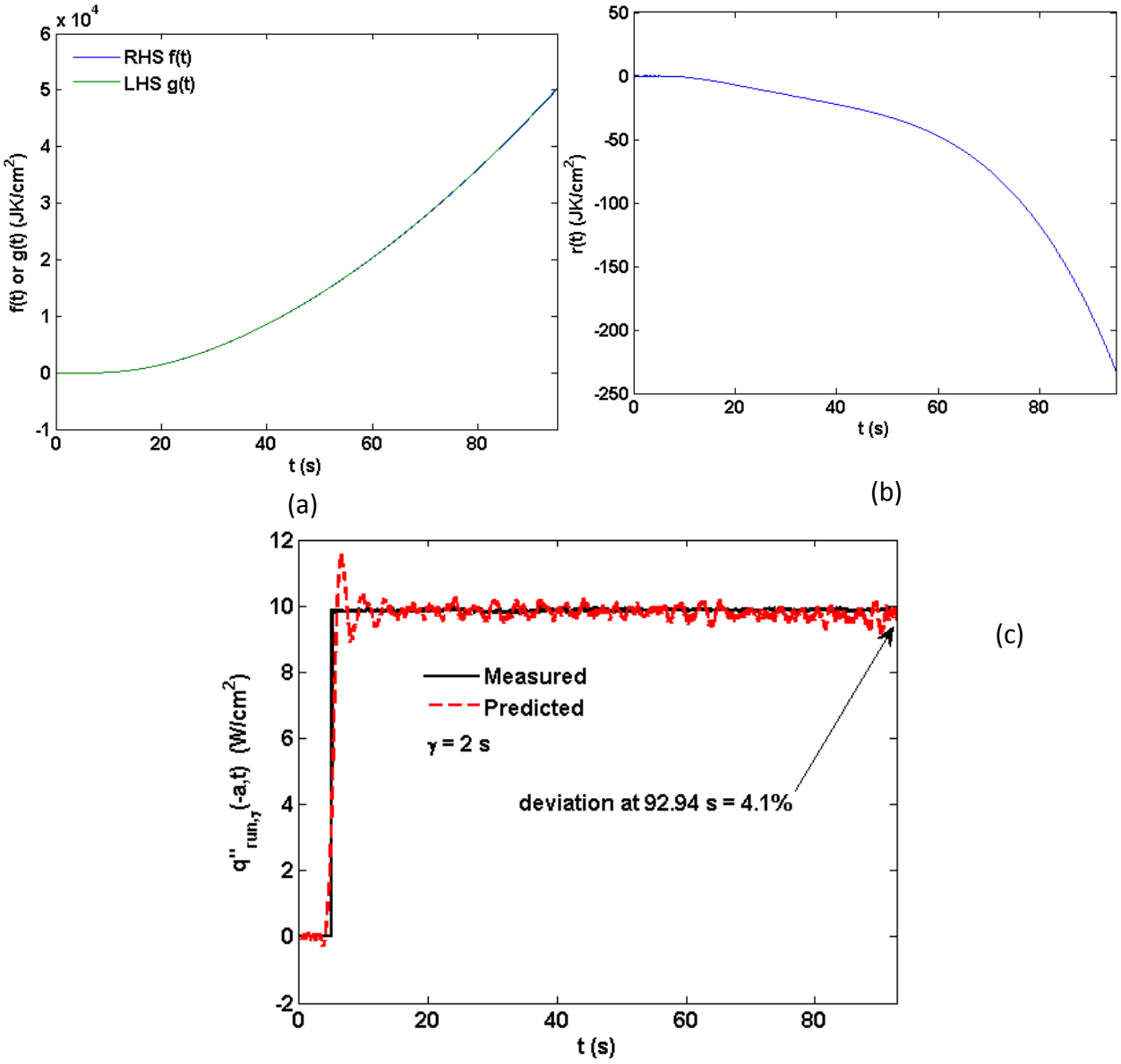

Figure 4.17. Pre-test diagnostic plots and the inverse prediction for case 1pTC4 using S2A0 thermocouple temperatures; (a) Comparison of LHS and RHS of Eq. (2.8a), (b) base residual function $r(t)$ and (c) inverse prediction

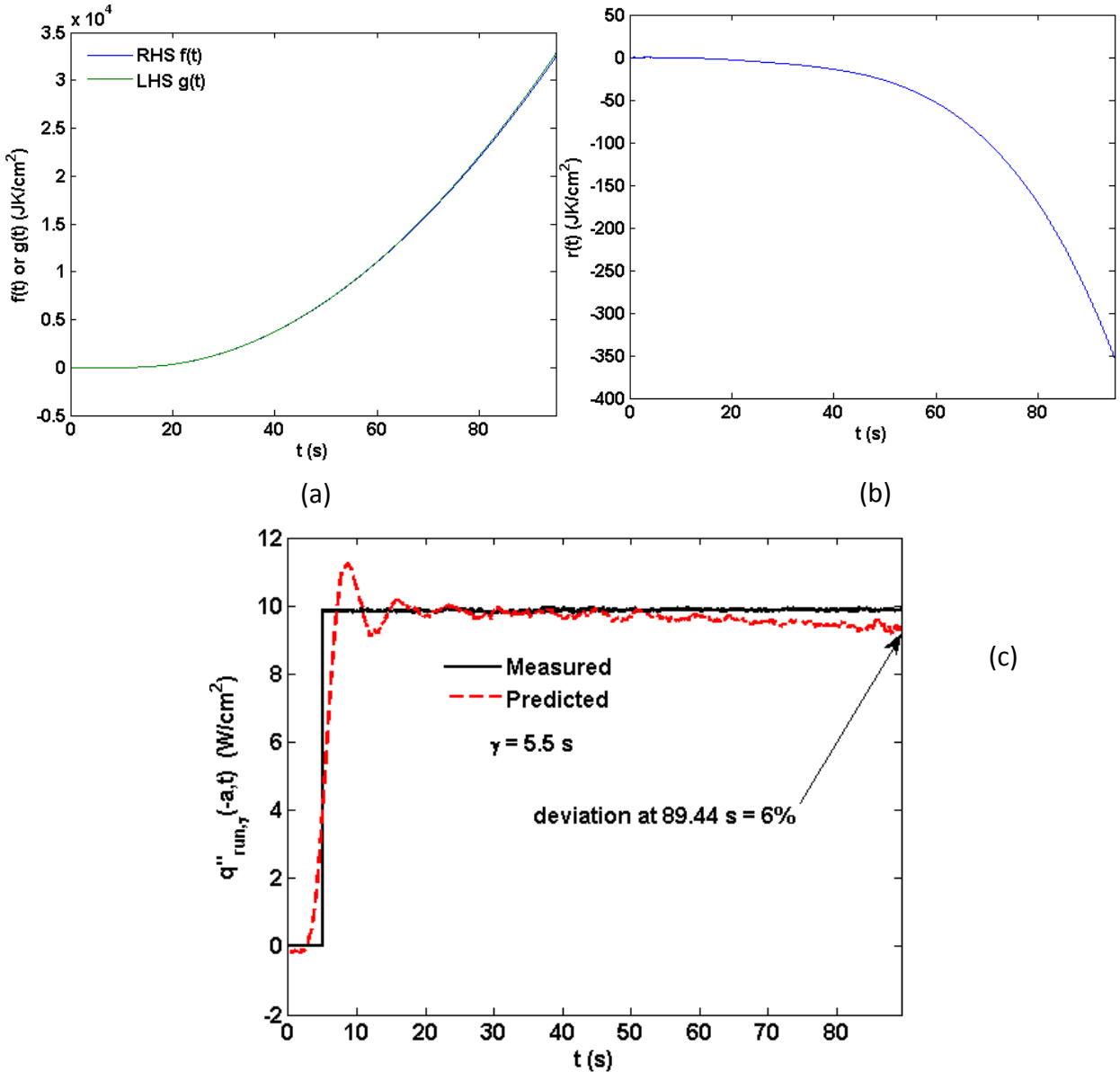

Figure 4.18. Pre-test diagnostic plots and the inverse prediction for 1pTC4 using S1B0 thermocouple temperatures; (a) Comparison of LHS and RHS of Eq. (2.8a), (b) base residual function $r(t)$ and (c) inverse prediction.

4.2 TWO-PROBE CALIBRATION INTEGRAL EQUATION METHOD

It has been shown in section 4.1 that the one-probe calibration integral equation method works very well when identical back-boundary conditions exist during both the calibration and real runs. It has also been shown that even when the back-boundary conditions are different, the error in the resolved heat flux prediction grows and becomes apparent only after a significantly large time interval, owing to the sequential nature of the resolution. However, in practice, the actual back-boundary conditions existing in-flight in the space vehicle will inevitably be different from the laboratory conditions. Accurate replication of the in-flight real run back-boundary conditions in a laboratory is highly unlikely. Also, for long heating durations, the error in the inverse prediction will be considerably large. The two-probe calibration integral equation method will attempt to address this issue, by providing an accurate reconstruction of the net surface heat flux, independent of the nature of the real run back-boundary condition.

4.2.1 Analysis of Kernel Strength

It has been proved in Appendix B that the two-probe calibration equation kernel $K(b, w, t-u)$, given by Eq. (2.23b), is identically equal to zero if the back-boundary conditions during the two calibration run stages are identical. To have a meaningful non-zero kernel, the back-boundary conditions must be vastly different. To analyze the behavior of the kernel, we start by re-stating the conventional (single-layer) two-probe calibration integral equation presented in compact form originally in Eq. (2.23a), as

$$\int_{u=0}^{t} q''_{run}(0,u)K(b,w,t-u)du = f(t)\ , \qquad t \geq 0, \tag{4.8a}$$

where the kernel $K(b, w, t-u)$ is explicitly given as

$$K(b,w,t-u) = \int_{r=0}^{t-u} [T_{cal1}(w,r)T_{cal2}(b,t-u-r) - T_{cal2}(w,r)T_{cal1}(b,t-u-r)]\, dr. \tag{4.8b}$$

From Eq. (4.8b), we can see that the kernel $K(b, w, t-u)$ is formed by the difference of two terms. We can also observe that $K(b, w, t-u)$ is dependent solely on the calibration temperature data. For convenience, we define

$$K_1(b,w,t-u) \triangleq \int_{r=0}^{t-u} T_{cal1}(w,r)T_{cal2}(b,t-u-r)\,dr, \qquad t-u \geq 0, \tag{4.9a}$$

and

$$K_2(b,w,t-u) \triangleq \int_{r=0}^{t-u} T_{cal2}(w,r)T_{cal1}(b,t-u-r)\,dr, \qquad t-u \geq 0. \tag{4.9b}$$

If the back-boundary conditions are identical during calibration runs 1 and 2, $K_1(b,w,t-u)$ equals $K_2(b,w,t-u)$ and their difference becomes zero. It follows that to obtain a non-zero difference, $K_1(b,w,t-u)$ and $K_2(b,w,t-u)$ should have different values. This difference occurs when the effect of the dissimilar boundary-conditions is sensed by one of the constituent thermocouple responses. The kernel $K(b,w,t-u)$ is a function of the b and w probe depths. It is known that the heat front takes some amount of time to penetrate the back-surface of the domain. Once the heat front reaches the back-surface, the convection boundary condition (forced or natural) becomes relevant and the problem becomes elliptic. The elliptic effect travels in the reverse direction and is first registered by the thermocouple located closest to the back surface, which, by definition, is the *w* depth thermocouple. It follows that the closer the *w* depth thermocouple is to the back surface, the sooner it will feel the effect of the back-boundary condition. For further explanation, it is essential to consider a test case for demonstrating the effects of the probe locations b and w on the strength of the kernel $K(b,w,t-u)$. Accordingly, let us consider AlRun2 (natural convection) as the first calibration run and AlRun3 (forced convection) as the second calibration run. Recall from Figures (3.8a-d) and (3.9a-d) and from Table 3.2, that the measured heat fluxes were almost equal for these two runs. The mean heat flux during AlRun2 was 9.89 W/cm^2 and during AlRun3 was 9.87 W/cm^2. The only difference between these two runs was the back-face boundary condition. Therefore, the selection of these particular runs helps to understand exclusively the effect of the different back boundary conditions on the kernel strength. Temperature data of probes S2A0 (x = 6.47mm), S1B0 (x = 12.95mm) and S2BF (x = L = 25.77mm) will be considered for investigating the effect of different probe depths on the kernel strength. As mentioned earlier, the kernel starts to attain non-zero values the moment when the *w* depth probe feels the effect of the back boundary condition. The physics changes from being driven solely by the active heated surface (parabolic or unidirectional) to also being influenced by the passively cooled back surface (elliptic or bi-directional). The time at which the effect of the back boundary condition starts to participate in the physics of the domain will be called the 'elliptic time'. The smaller the elliptic time, the sooner will the kernel become non-zero. This implies that placing the *w*

depth probe directly onto the back surface ($w = L$) would result in the shortest elliptic time. The favored location of the w depth probe has been determined. The best location for the b depth probe is understood with the aid of Figures 4.19(a-c) to 4.21(a-c). Figure 4.19(a-c) shows the kernel $K(b,w,t)$ and its components $K_1(b,w,t)$ and $K_2(b,w,t)$ obtained when S2A0 is chosen as the b depth probe and S2BF as the w depth probe. In Figure 4.20(a-c) S2BF is replaced by S1B0 as the w depth probe and lastly, in Figure 4.21(a-c), S1B0 is now considered as the b depth probe and S2BF as the w depth probe. It is important to note that for the sake of analysis, the kernel and its components have been expressed as a function of t instead of $t-u$. When plotted against t the behavior of the kernel and its components with increasing time can be easily understood.

Out of the three considered combinations of b and w depth probes, the strongest kernel is obtained in Figure 4.19(c) where b = 6.47mm and w = L = 25.77mm. The maximum value attained by $K_1(b,w,t)$ is about $1.6\text{x}10^4$ K^2s larger than that attained by $K_2(b,w,t)$. The difference between the two provided the required kernel $K(b,w,t)$ with a maximum value around 16000 K^2s. Observe that $K_2(b,w,t)$ contains $T_{cal2}(w,t)$ which belongs to the forced convection run AlRun3. When the heat front penetrates the back surface, $T_{cal2}(w,t)$, which is cooled by forced convection, records a lower temperature than $T_{cal1}(w,t)$, which stays hotter due to heat loss via natural convection. The effect of the back boundary condition has still not propagated to the b depth probes. Therefore, $T_{cal1}(b,t)$ and $T_{cal2}(b,t)$ are both equal. The value of $K_2(b,w,t)$, which contains the cooler $T_{cal2}(w,t)$, starts to decrease and ultimately results in a positive value of $K(b,w,t)$. The kernel $K(b,w,t)$ grows as the effect of dissimilar back boundary conditions becomes pronounced with increasing time. The start of this growth is strongly influenced by the location of the w probe whereas the rate of the growth is, in turn, strongly dependent on the location of the b probe. To explain this claim, consider the values of $K_1(b,w,t)$ and $K_2(b,w,t)$ before elliptic time has been reached. The temperatures $T_{cal1}(b,t)$and $T_{cal2}(b,t)$ are penetrated by the heat front first and hence start to increase. It follows that as the b location is brought closer to the heated surface, $T_{cal1}(b,t)$ and $T_{cal2}(b,t)$will get increasingly hotter. When elliptic time is eventually reached, the difference between the high magnitudes already attained by $T_{cal1}(b,t)$and $T_{cal2}(b,t)$ will be scaled by the difference between $T_{cal1}(w,t)$ and $T_{cal2}(w,t)$. It is noted that the difference between $T_{cal1}(w,t)$ and $T_{cal2}(w,t)$ does not increase significantly due to their dissimilar back-boundary conditions and is not dependent on the location of the b probes. It follows that the resulting kernel $K(b,w,t)$, which is the accumulation (integration over time) of the said 'scaled difference', will proceed to grow rapidly. In conclusion, the location of the b probe should be as

close to the heated surface as possible to ensure a rapid growth in kernel strength. This concept is supported by Figures 4.19 to 4.21.

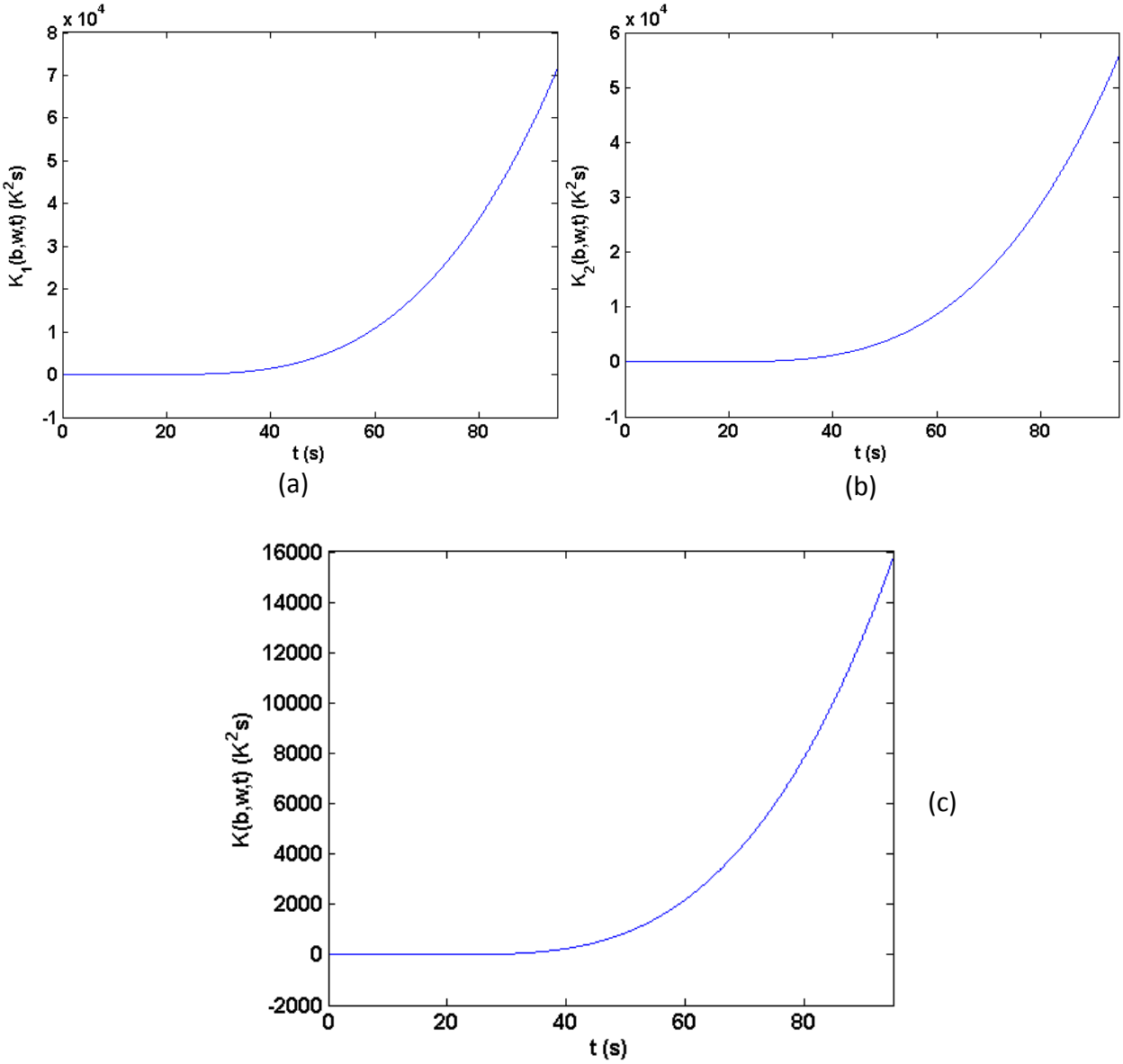

Figure 4.19. The kernel and its components obtained for S2A0 as the b depth probe and S2BF as the w depth probe; (a) $K_1(b,w,t)$, (b) $K_2(b,w,t)$ and (c) $K(b,w,t)$.

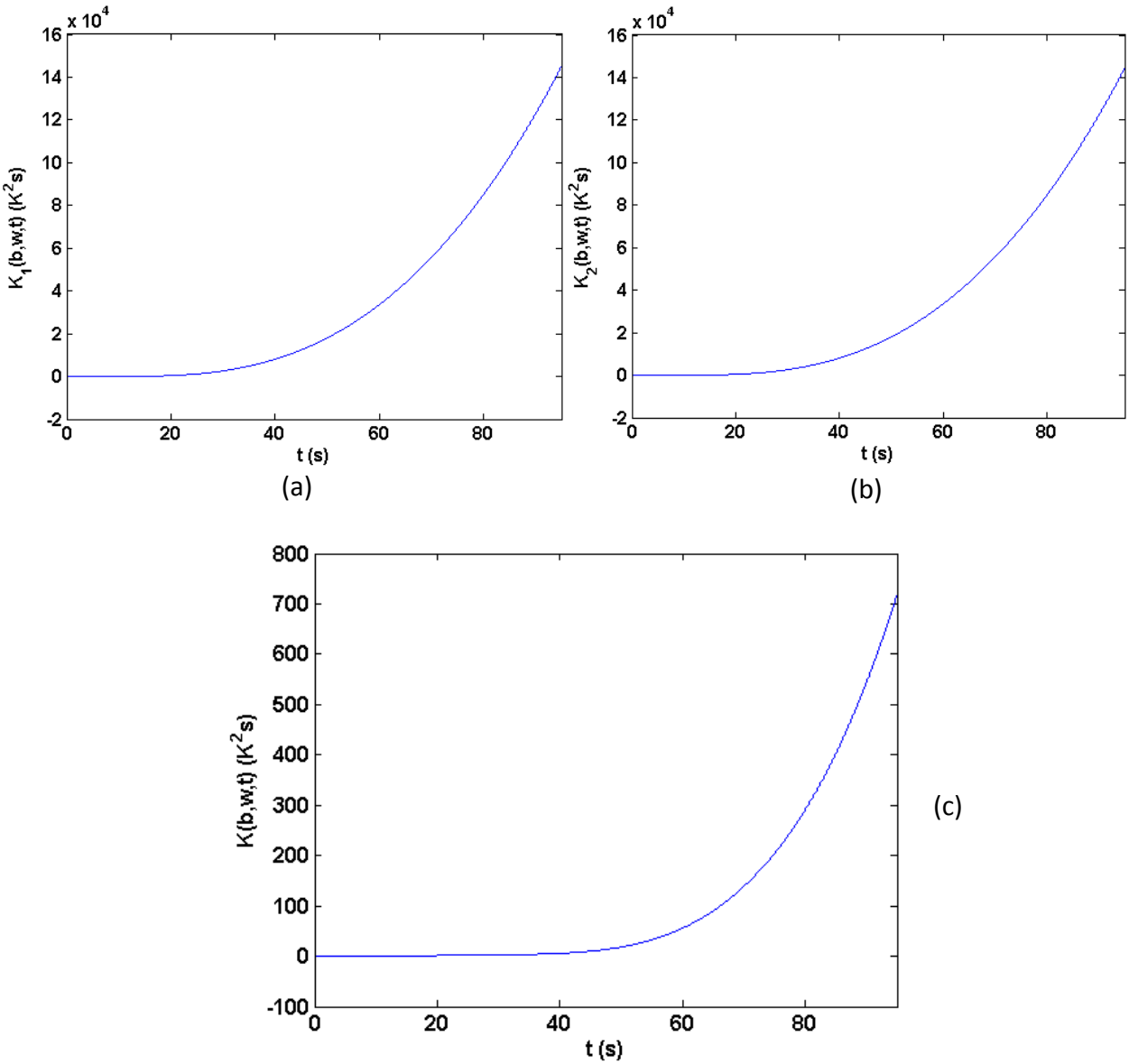

Figure 4.20. The kernel and its components obtained for S2A0 as the b depth probe and S1B0 as the w depth probe; (a) $K_1(b,w,t)$, (b) $K_2(b,w,t)$ and (c) $K(b,w,t)$.

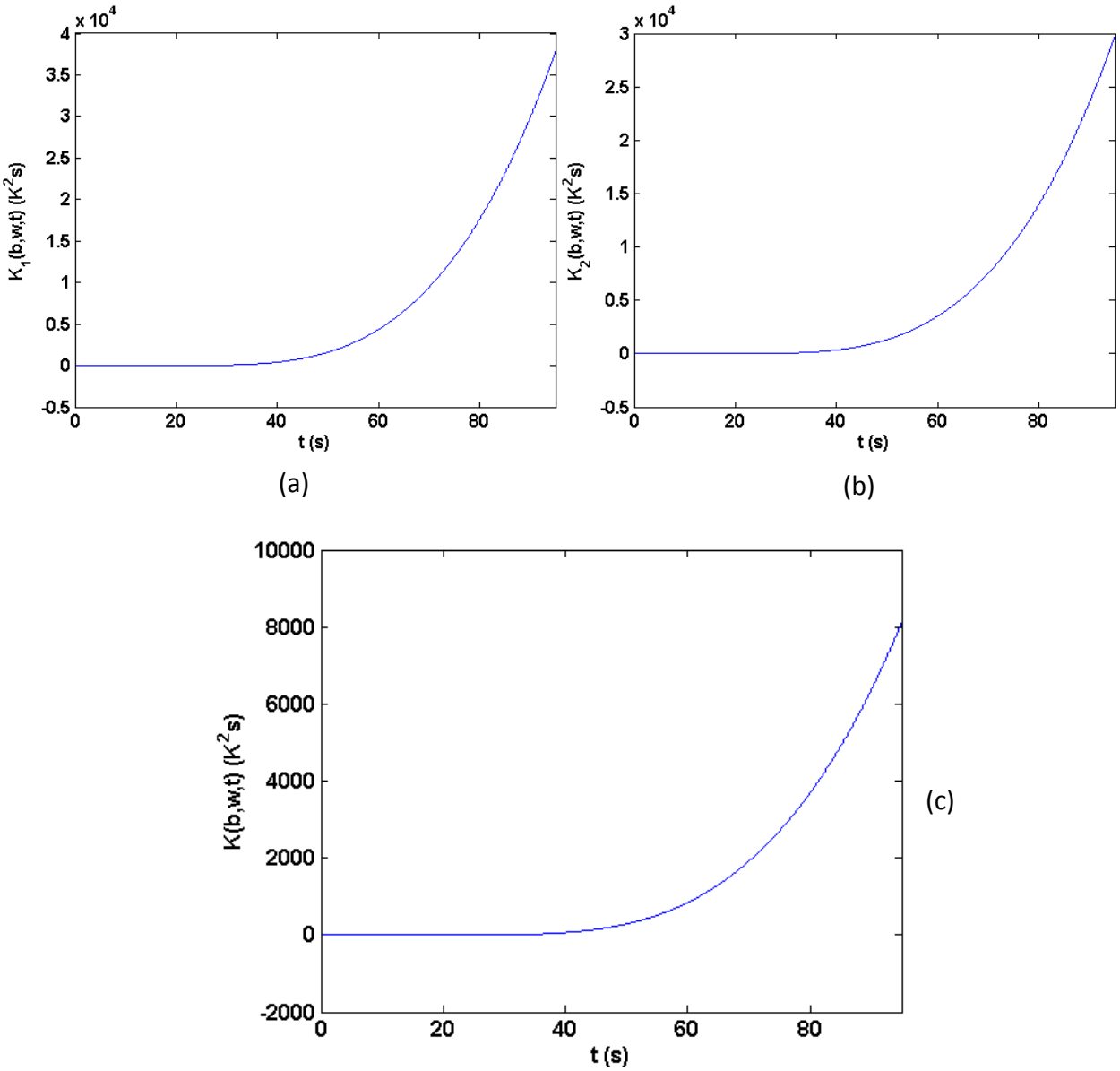

Figure 4.21. The kernel and its components obtained for S1B0 as the b depth probe and S2BF as the w depth probe; (a) $K_1(b,w,t)$, (b) $K_2(b,w,t)$ and (c) $K(b,w,t)$.

Comparison of Figure 4.19(c) and Figure 4.21(c) verifies that higher growth in the kernel is achieved when the b probe is closer (b = 6.47mm instead of b = 12.95mm) to the heated surface. Figure 4.20 shows that this combination of probes produces the highest individual magnitudes for $K_1(b,w,t)$ and $K_2(b,w,t)$ which results in a weak $K(b,w,t-u)$. This is as a result of both probes, b = 6.47mm and W = 12.95mm, having the closest proximity to the heated surface than that for the other two combinations in Figures 4.19(a,b) and 4.21(a,b). Furthermore, the elliptic time is relatively larger resulting in a smaller difference between $K_1(b,w,t)$ and $K_2(b,w,t)$ which produces a weaker kernel. Based on this discussion, thermocouple S2A0 will be considered as the b probe and thermocouple S2BF as the w probe for the two-probe calibration method.

4.2.2 Selection of Test Cases

As observed in the previous section, the kernel $K(b,w,t)$ is comprised of the calibration temperature data. Hence, similar to the one-probe calibration method, the selection of the most suitable calibration runs is vital to obtain a good inverse prediction. It is well understood that long pulse heat flux produces the strongest temperature response. Therefore, for the Mica Runs, the most suitable combination of calibration runs would be McRun1 (natural convection) as the first calibration run and McRun2 (forced convection) as the second calibration run. Similar to the one-probe analysis, Mica Runs 3 and 4 will be selected as the real runs for prediction.

For the Alumina Runs, AlRun3 (forced convection) will be considered as the second calibration run. For the first calibration run, a choice between AlRun1 and AlRun2 has to be made. Both AlRun1 and AlRun2 have pulse heat flux profiles but the magnitude is higher for AlRun1. Hence, a stronger kernel is expected with AlRun1. For verification, the kernels obtained for both candidates when paired with AlRun3 as the second calibration run are displayed in Figure 4.22. The kernel obtained with AlRun1 as the first calibration run is stronger as seen in Figure 4.22(a) versus Figure 4.22(b). The log-log plot places emphasis on early time behavior which reveals a distinct elbow, shown in Figure 4.22(b,d). The slope of the kernel starts to dip and then picks up. There is no physical reason for the value of the kernel to start decreasing once growth has begun. The elbow or dip can be best explained as the influence of measurement noise. However, it is interesting to note that the observed time for the heat front to reach the back surface is 11.98s as shown in Figure 4.23 for the AlRun2 case. Moreover, the time at which the elbow occurs for the AlRun2 kernel, as seen in Figure 4.22(d), is 18.66 s. This implies that the

time needed for the heat front to back propagate to the S2A0 location (about 21mm from the back face) should be about 6.7s.

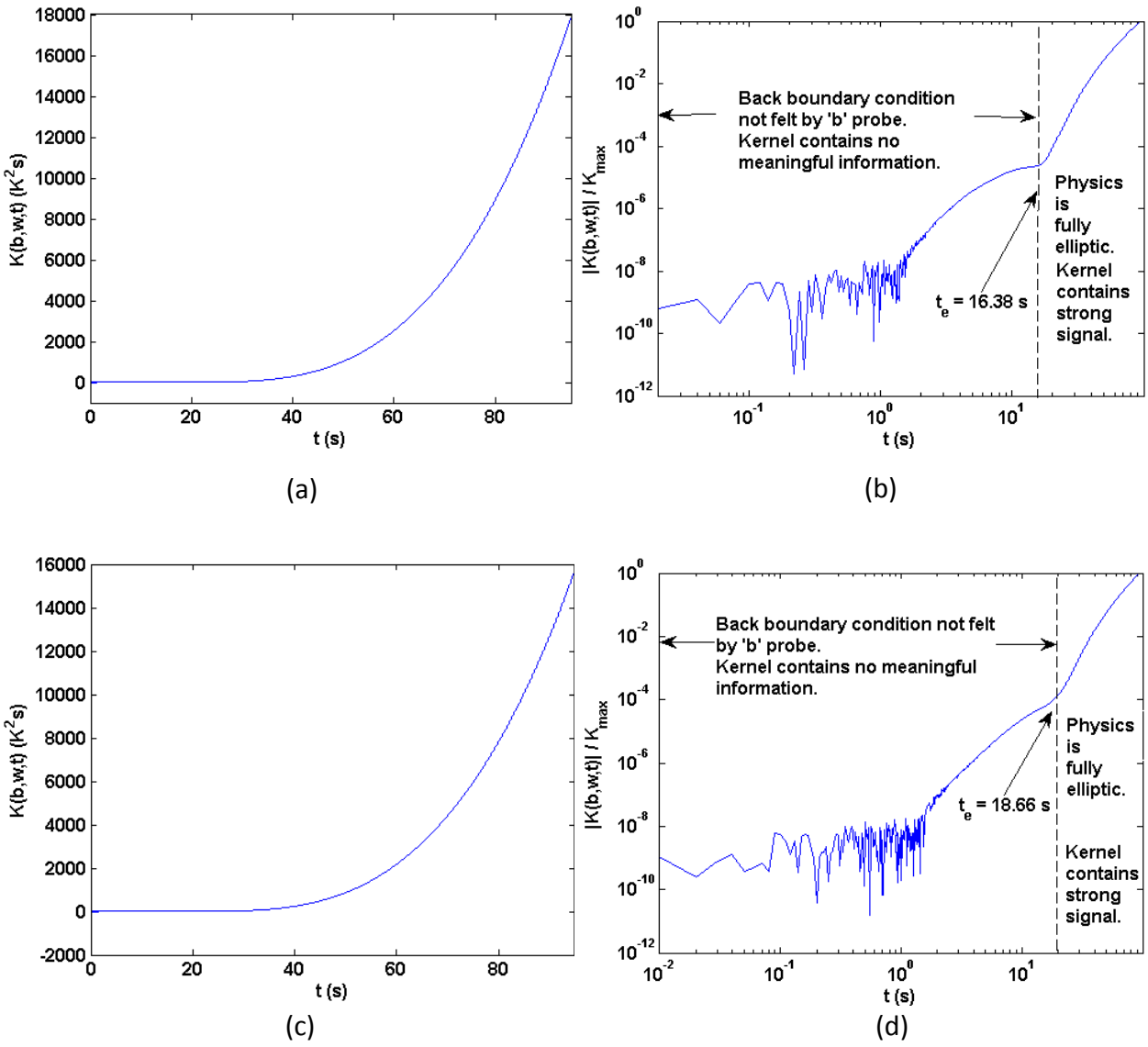

Figure 4.22. Assessment of kernel strength for AlRun1; (a) plot of kernel versus time, (b) log-log plot of absolute value of normalized kernel, and for AlRun2; (c) plot of kernel versus time, (d) log-log plot of absolute value of normalized kernel.

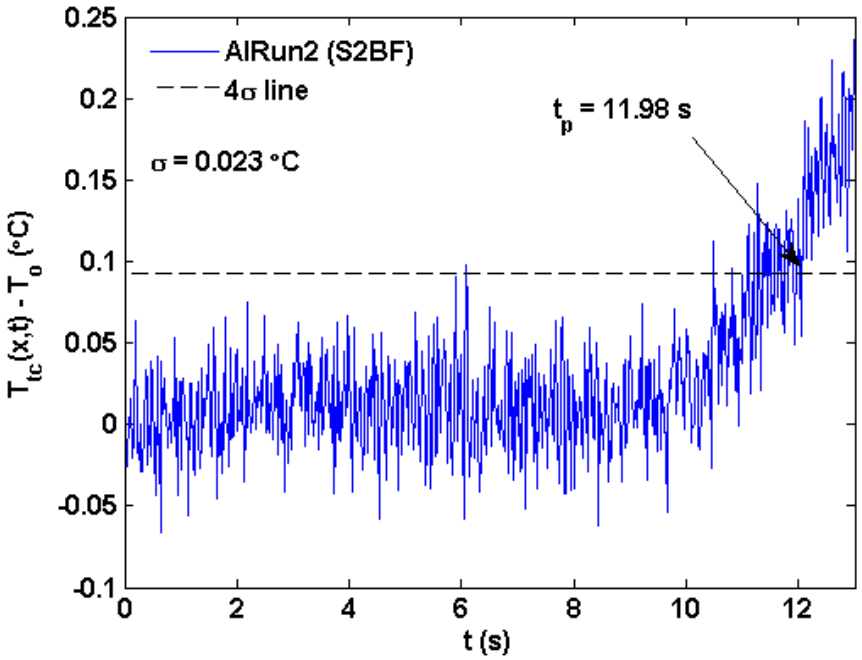

Figure 4.23. Observed penetration time at the S2BF probe site (x = L = 25.77 mm) for the AlRun2 case.

The closeness in these values suggests that the occurrence of the elbow is related with the effect of the back boundary condition reaching the b probe. After the elbow, Figures 4.22(b) and 4.22(d) show that the kernels monotonically increase as time progresses and hence can be considered to have achieved an adequate level of meaningful information. Accordingly, the time at which the elbow occurs will be defined as the 'effective elliptic time' t_e for the selected calibration run cases. It can be inferred that beyond t_e, the strength of the kernel continues to grow. Hence a strong kernel can be characterized by a low value of t_e and a high maximum value attained at the maximum data collection time. Based on these parameters, the combination of AlRun1 and AlRun3 as the two calibration runs produces the strongest kernel and will hence be selected for the two-layer analysis. The real run considered for the two-layer analysis will be AlRun4. The specific test cases considered for the two-probe analysis are presented in Table 4.6.

In comparison with the one-probe calibration method, a significantly longer time (t_e) than γ is required by the two probe kernel to achieve a strong signal. If t_e was used as the future-time parameter γ, the result would be extensively over-smoothed due to a significant loss in the original physics of the problem. Owing to the sequential nature of resolution, the future-time regularization method would be unstable for any $\gamma < t_e$ and cannot be used. Hence, a global

method, that simultaneously considers the entire time domain is needed for reconditioning of the kernel matrix $\mathcal{K}$, as discussed previously in Chapter 2.

Table 4.6. Overview of Test Cases considered for Two-probe Analysis.

Test Case	Calibration Run 1	Calibration Run 2	Real Run
2pTC1	McRun1	McRun2	McRun3
2pTC2	McRun1	McRun2	McRun4
2pTC3	AlRun1	AlRun3	AlRun4

4.2.3 Inverse Results

The heat activation time t_{ON} is known for the two calibration runs. To obtain a healthy kernel, it is highly advantageous to ignore the calibration data for $t < t_{ON}$. The clipping of the lead data prevents the unnecessary accumulation of noise in the kernel. The presence of lead data would also increase the estimated effective elliptic time t_e significantly. Accordingly, the calibration run data were clipped and only data from $t \geq t_{ON}$ were considered for analysis.

The results obtained for each test case will now be presented.

2pTC1 –

Similar to the one-probe calibration method, as a pre-test diagnostic, to determine how accurately the data satisfies the two-probe calibration integral equation, the RHS = $f(t)$ and the LHS = $g(t)$ of Eq.(2.22) are calculated and compared.

Again, the nature of the base residual function $r(t)$, as per Eq. (4.10), and defined as the difference between the RHS and LHS of Eq. (2.22), acts as a precursor to the quality of the inverse prediction that can be expected of the data. It gives a measure of the extent by which the equality of Eq. (2.22) is violated by the selected experimental data.

$$r(t) = f(t) - \int_{u=0}^{t} K(b, w, t-u)\, q''_{run}(0, u)\, du\,, \qquad t \in [0, t_{max} - t_{ON}]. \tag{4.10}$$

The base residual function and the LHS and RHS of Eq. (2.22) are compared in Figure 4.24. Comparison of the scales of Figures 4.24(a) and (b) shows that the base residual is two orders of

magnitude smaller than the LHS (or RHS). The maximum absolute value of $r(t)$ is about 1% of that of $f(t)$. The LHS and RHS of Eq. (2.22) are in good agreement with each other and a good quality inverse prediction is expected.

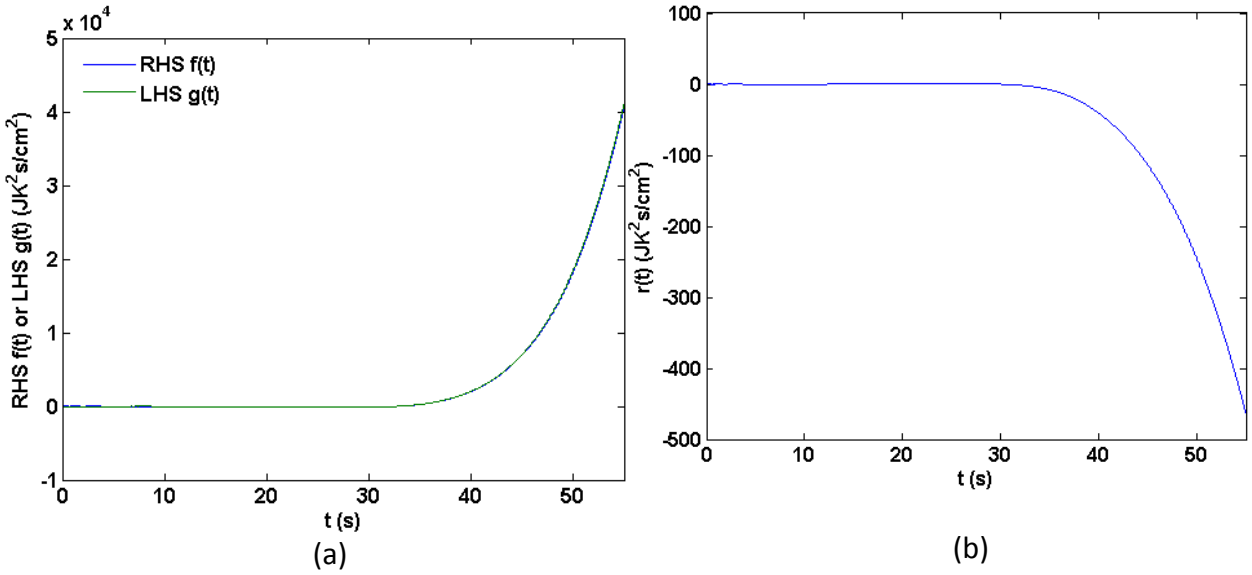

Figure 4.24. Pre-test diagnostic plots for 2pTC1; (a) Comparison of LHS and RHS of Eq. (2.22) and (b) base residual function $r(t)$.

We can now proceed to examining the nature of the kernel $K(b, w, t-u)$ produced by the 2pTC1 data. Again, important indicators of the quality of the kernel are the time at which the kernel comes out of the uncertainty region t_e and the maximum absolute value it attains. Figure 4.25(a) shows the kernel plotted against the u time-axis. The purpose of this figure is to show clearly the form in which the kernel enters the calculation at a given time. Figure 4.25(b), on the other hand, shows the kernel plotted against time. The value of the kernel at every instance in time can be observed from this figure. Figure 4.25(c) shows the log-log plot of the absolute value of the normalized kernel versus time t. This figure makes it easy to identify the effective elliptic time t_e of the system. Figure 4.25 also applies to 2pTC2 since the selected calibration runs are the same as 2pTC1.

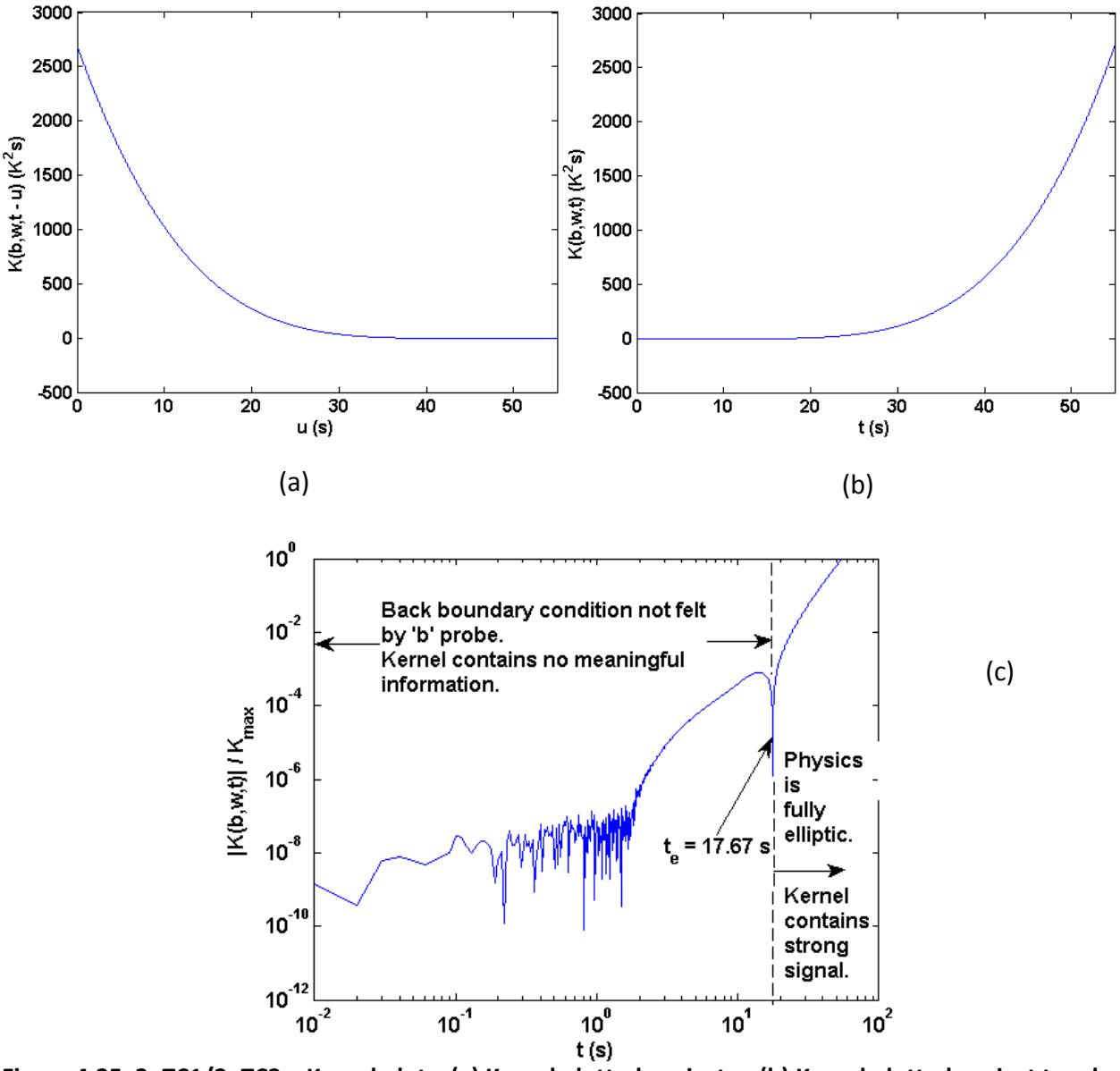

Figure 4.25. 2pTC1/2pTC2 – Kernel plots; (a) Kernel plotted against u, (b) Kernel plotted against t and (c) Log-log plot of absolute value of normalized kernel versus time.

From Figure 4.25(b), we can see that the signal starts to pick up around 20 s. Figure 4.25(c) gives a clearer perspective of the initial time domain when the kernel is hovering around zero. From t = 17.67s onwards the kernel shows a perpetually increasing trend. This is an indication of the physics becoming fully elliptic. The kernel has come out of the uncertainty region and is beginning to accumulate a meaningful signal. The effective elliptic time t_e = 17.67s is about 32% of the total analysis time t_{max} = 54.98s. Consequently, 32% of rows (first 1767 rows out of

total 5498 rows) of the matrix $\mathcal{K}$, given in Eq. (2.24b), would contain no meaningful data. This gives a good idea of how badly $\mathcal{K}$ is ill-conditioned.

As described in Chapter 2, the reconditioning of $\mathcal{K}$ is carried out by finding its SVD and truncating the S matrix at some truncation index p. The net surface heat flux vector $\bar{q}_p$ is then solved for by using Eq. (2.30f). Excessive truncation results in the loss of physics and tends to over-smooth or dampen the resulting prediction. Too little truncation retains more physics but fails to prevent the prediction from becoming unstable. To seek an optimum region for p the following procedure was followed.

A set of truncation indices $\{p\}_1^{500}$ was chosen, and $\bar{q}_p$ was evaluated at each p and the resulting error $\varepsilon_{q,p}(t)$ in predicting the measured $\bar{q}$ was calculated as

$$\varepsilon_{q,p}(t) = q''_{run}(0,t) - q''_{run,p}(0,t), \qquad t \in [0, t_{max} - t_{ON}]. \tag{4.11a}$$

The error during only the heating period $\varepsilon_{q,p,heat}(t)$ was also evaluated as

$$\varepsilon_{q,p,heat}(t) = q''_{run}(0,t) - q''_{run,p}(0,t), \qquad t \in [t_{ON}, t_{OFF}], \tag{4.11b}$$

where t_{OFF} is the time at which the heat was turned off. The temporal errors obtained at each value of p were quantified by finding their standard deviation $\sigma_{\varepsilon q}(p)$ for the whole time domain, and $\sigma_{\varepsilon q,heat}(p)$ for the heating period. Figure 4.26 shows the plot of $\sigma_{\varepsilon q}(p)$ versus p. Ideally, $\sigma_{\varepsilon q}(p)$ should be equal to zero, but due to the influence of the regularization scheme, $\sigma_{\varepsilon q}(p)$ shows a distinct non-zero minimum at p = 27. Figure 4.27 show the plot of $\sigma_{\varepsilon q,heat}(p)$ versus p. A distinct minimum is observed again at p = 27.

In hindsight, with having the knowledge of the measured surface heat flux $q''_{run}(0,t)$, we have determined where the optimum region of the truncation index should be. Since in the actual scenario $q''_{run}(0,t)$ is unknown, the challenge now lies in developing a metric that points to the neighborhood of p = 27, without the use of measured heat flux data.

Dr. Majid Keyhani proposed such a metric based on the statistical analysis of the local residual function $r_p(t)$. The local residual function is defined by

$$r_p(t) = f(t) - \int_{u=0}^{t} K(b, w, t-u) q''_{run,p}(0,u) du\,, \qquad t \in [0, t_{max} - t_{ON}]. \tag{4.12}$$

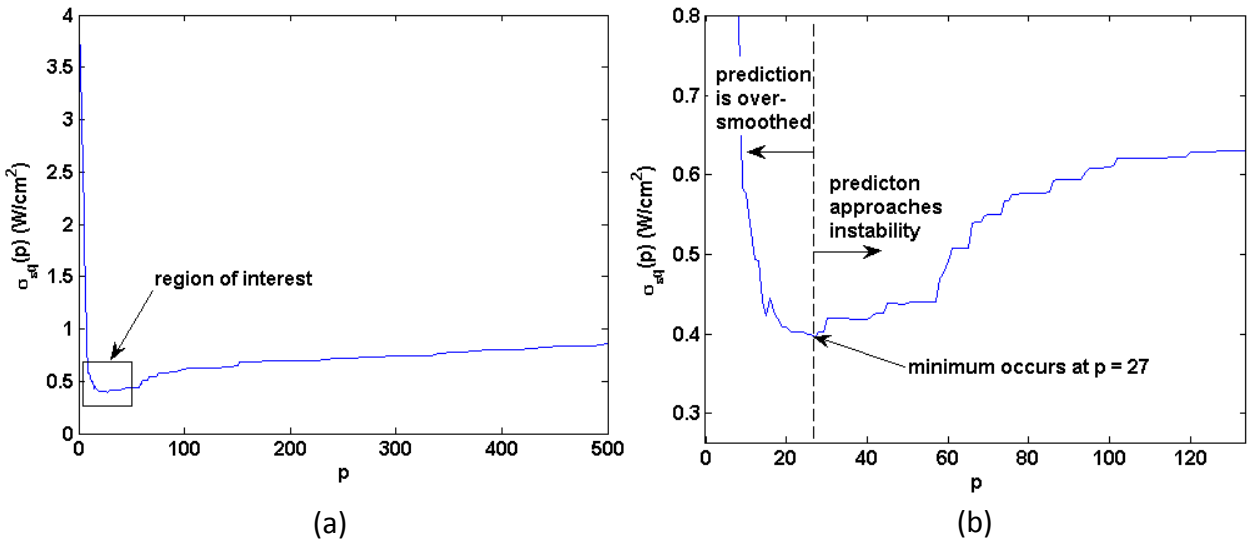

(a) (b)

Figure 4.26. 2pTC1 - Plot of $\sigma_{\varepsilon q}(p)$ versus p for (a) The entire set of truncation indices $\{p\}_1^{500}$ and (b) Zoomed into the region of interest.

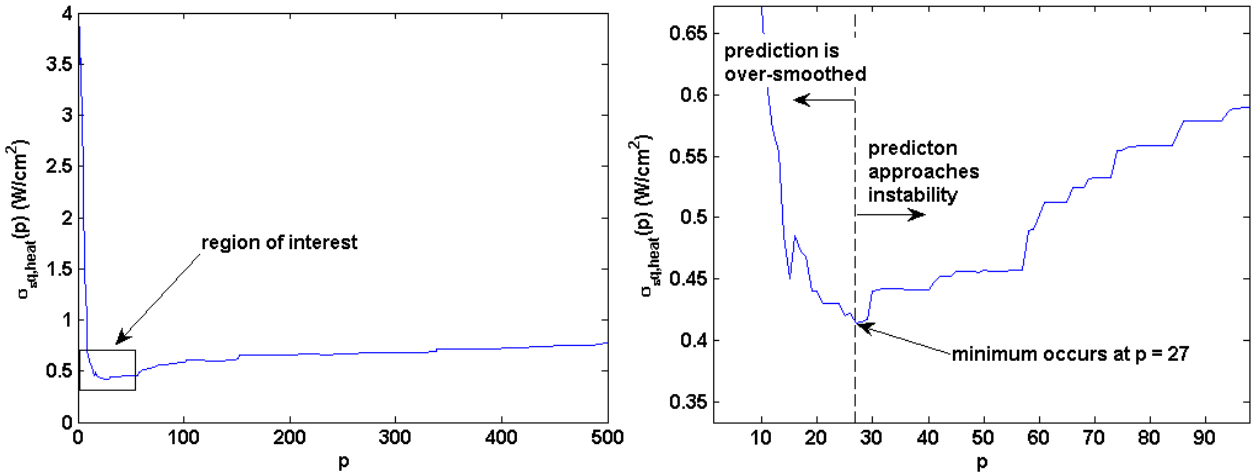

(a) (b)

Figure 4.27. 2pTC1 - Plot of $\sigma_{\varepsilon q,heat}(p)$ versus p for (a) The entire set of truncation indices $\{p\}_1^{500}$ and (b) Zoomed into the region of interest.

The local residual function $r_p(t)$ differs from the base residual $r(t)$ in that the calculation of $r_p(t)$ utilizes $q''_{run,p}(0,t)$ which carries the influence of the regularization scheme. It gives a measure of the extent by which the regularization parameter p violates the equality of Eq. (2.22). The metric $\psi(p)$ for estimating the optimum region for p is defined by

$$\psi(p) = \frac{\sigma_r(p)}{\mu\left(\{\sigma_r(j)\}_{j=1}^{p}\right)}, \qquad 1 \le p \le 500, \tag{4.13}$$

where $\sigma_r(p)$ is the standard deviation of $r_p(t)$ and μ is the arithmetic mean of σ_r. The metric $\psi(p)$ can be explained as the standard deviation of the local residual function evaluated at a specific p, divided by the running mean of the standard deviations of the local residual functions evaluated from 1 to the current value of p.

Figure 4.28 shows a log-log plot of $\psi(p)$ versus p. A distinct minimum is observed at p = 21 which is only 6 indices away from the pre-determined p = 27 from Figures 4.26(a,b) and 4.27(a,b). The corresponding predictions $q''_{run,p}(0,t)$ obtained at p = 21 and p = 27 are shown in

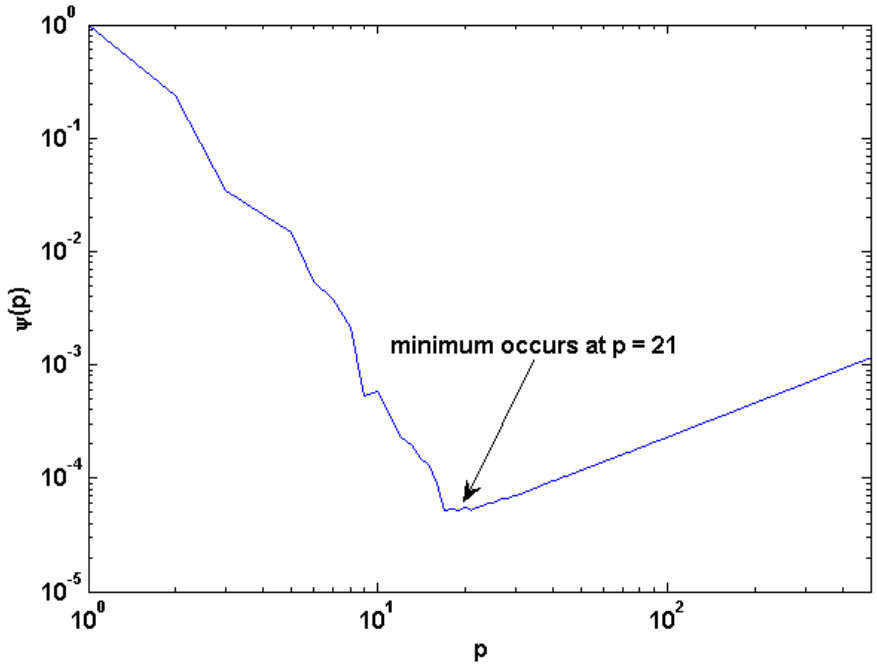

Figure 4.28. 2pTC1 - Log-log plot of $\psi(p)$ versus p. A distinct minimum is observed at p = 21.

Figure 4.29. The associated metrics for judging the quality of the predictions are presented in Table 4.7. The metrics are named in a manner similar to that described in the one-probe analysis. The regularization parameter is changed from γ to p.

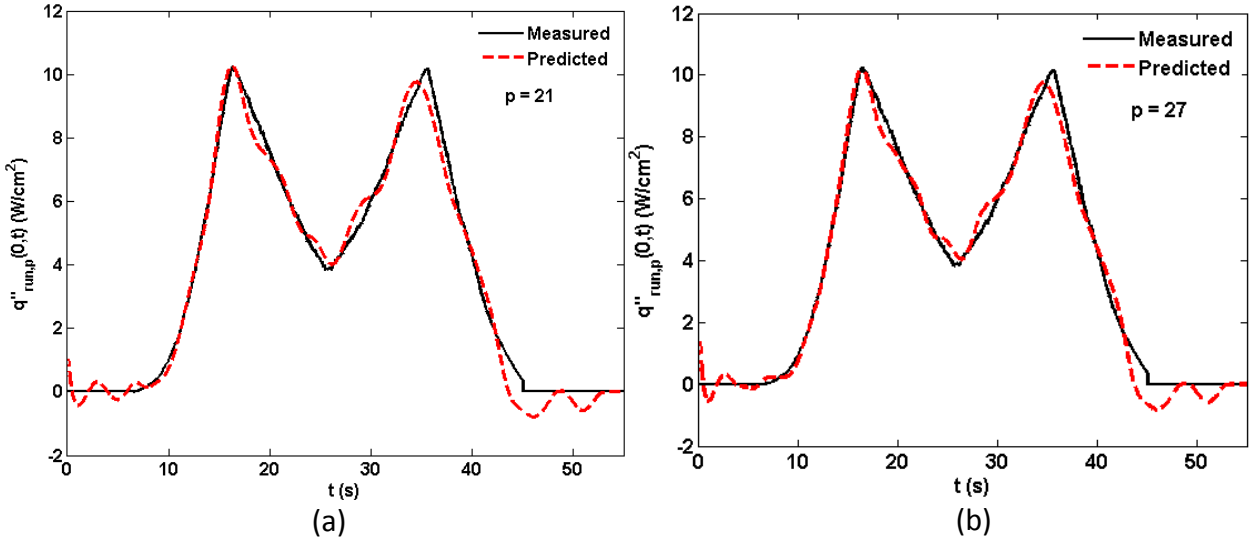

Figure 4.29. 2pTC1 - Plots of the predicted net surface heat flux $q''_{run,p}(0,t)$ at (a) p = 21 and (b) p = 27.

Table 4.7(a). 2pTC1 – Inverse Prediction Metrics. E = 204.03 J/cm^2.

p	$\sigma_{\epsilon q}$ (W/cm^2)	$\sigma_{\epsilon q,heat}$ (W/cm^2)	E_p (J/cm^2)	E_p/E
21	0.402	0.430	197.78	0.969
27	0.396	0.414	198.07	0.971

Table 4.7(b). 2pTC1 – Inverse Prediction Metrics. q''_{pk1}= 10.25 W/cm^2 @t = 16.41 s, q''_{pk2}= 10.18 W/cm^2 @t = 35.53 s

p	$q''_{pk1,p}$ (W/cm^2)	$\frac{q''_{pk1,p}}{q''_{pk1}}$	$\Delta t_{pk1,p}$ (s)	$q''_{pk2,p}$ (W/cm^2)	$\frac{q''_{pk2,p}}{q''_{pk2}}$	$\Delta t_{pk2,p}$ (s)
21	10.25	1	-0.14	9.75	0.96	-1.01
27	10.19	0.99	-0.07	9.75	0.96	-0.98

Figure 4.29 suggests no major differences in the two predictions in terms of appearance and associated metrics. The standard deviation of the error in prediction $\sigma_{\varepsilon q}$ changes by 1.5% and that only during the heating period $\sigma_{\varepsilon q,heat}$ changes by 3.8%. The predicted total energy input changes by only 0.15%. Observe that $\sigma_{\varepsilon q}$ and $\sigma_{\varepsilon q,heat}$ both decrease as p increases. The metric $\psi(p)$ suggests a truncation index p that tends to slightly over smooth the prediction. However, the overall quality of the prediction obtained at p = 21, as suggested by the metric $\psi(p)$, matches very well with the prediction obtained at the pre-determined p = 27. The accuracy of the predicted heat flux peak ratios using p = 21 (peak-1, ratio=1 and peak-2, ratio=0.96) and p = 27 (peak-1, ratio=0.99 and peak-2, ratio=0.96) is remarkable and practically the same. Similar to the one-probe calibration method, the first peak is resolved more accurately than the second. To infer that $\psi(p)$, at the very least, points to a region of low sensitivity to the choice of p, would be a fairly accurate assessment of the metric's performance. A differentiating factor between the two-probe and one-probe calibration methods is the frequency of oscillations observed in the predicted heat fluxes. The whole domain resolution process of the SVD tends to distribute the errors or oscillations over time, whereas the sequential nature of the future-time method shows high frequency oscillations in the predictions and may even tend to grow larger.

2pTC2 –

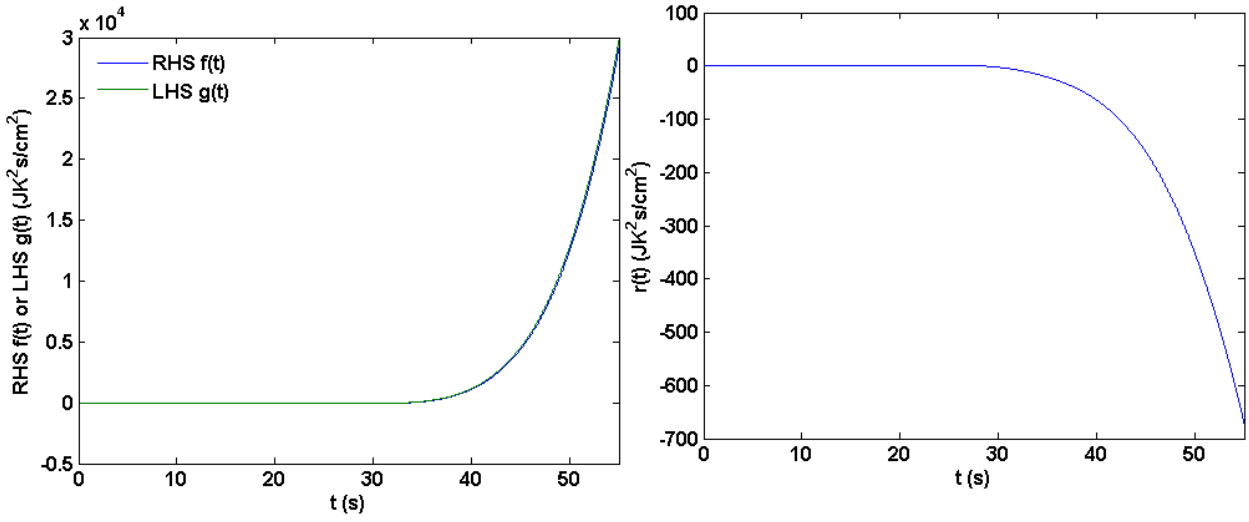

(a) (b)

Figure 4.30. Pre-test diagnostic plots for 2pTC2; (a) Comparison of LHS and RHS of Eq. (2.22) and (b) base residual function $r(t)$.

Figure 4.30 presents the comparison of the LHS and RHS of Eq. (2.22) and the accompanying base residual function $r(t)$ for test case 2pTC2. Similar to 2pTC1, comparison of the scales of Figure 4.30(a) and (b) shows that the base residual is two orders of magnitude smaller than the LHS (or RHS). For this case the maximum absolute value of $r(t)$ is about 2% of that of $f(t)$ which is higher than the test case 2pTC1 (about 1%). Consistently negligible base residual functions have been attained throughout the one-probe and two-probe test cases. The collected data are shown to be of a high quality and applicable equally well for both methods.

Since the calibration runs for both test cases are the same, the analysis of the kernel is not repeated here. Following the procedure described in 2pTC1, $\sigma_{\varepsilon q}(p)$ and $\sigma_{\varepsilon q,heat}(p)$ were evaluated and are shown in Figure 4.31 and Figure 4.32, respectively. Both metrics suggest p = 15 as the optimum value.

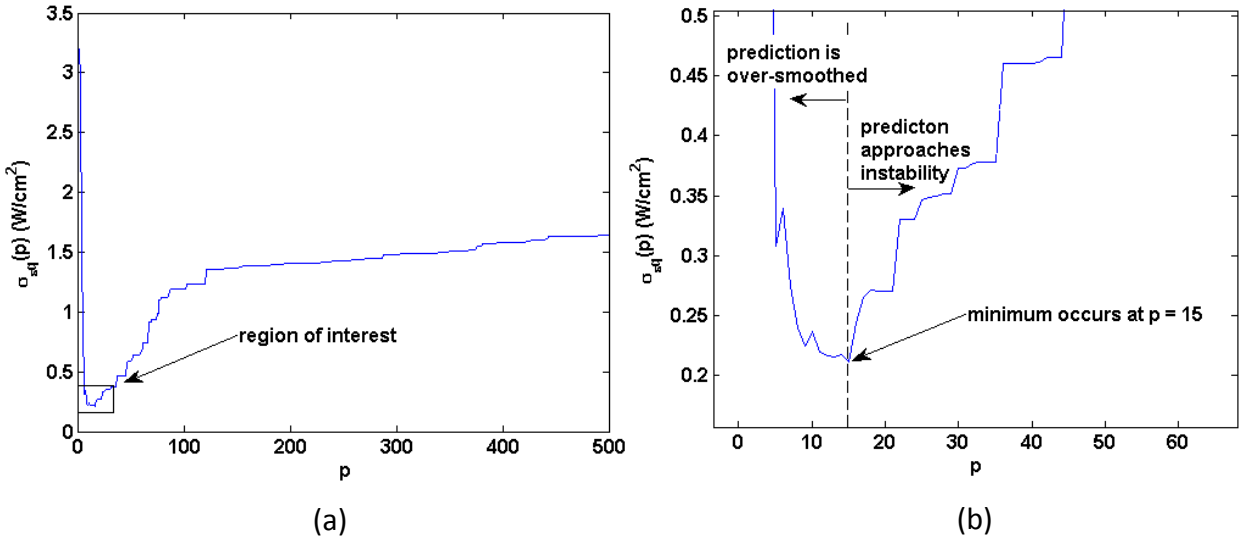

Figure 4.31. 2pTC2 - Plot of $\sigma_{\varepsilon q}(p)$ versus p for (a) The entire set of truncation indices $\{p\}_1^{500}$ and (b) Zoomed into the region of interest.

From Figure 4.31 we can see that the curve around the region of the minimum is not as gradual as in 2pTC1. The sensitivity to the selected value of p is hence expected to be higher. The metric $\psi(p)$ shows a distinct minimum at p = 17 as shown in Figure 4.33, which is only two indices more than the pre-determined optimum value p = 15. The predictions obtained at p = 15 and p = 17 are displayed in Figure 4.34. The accompanying metrics are listed in Table 4.8.

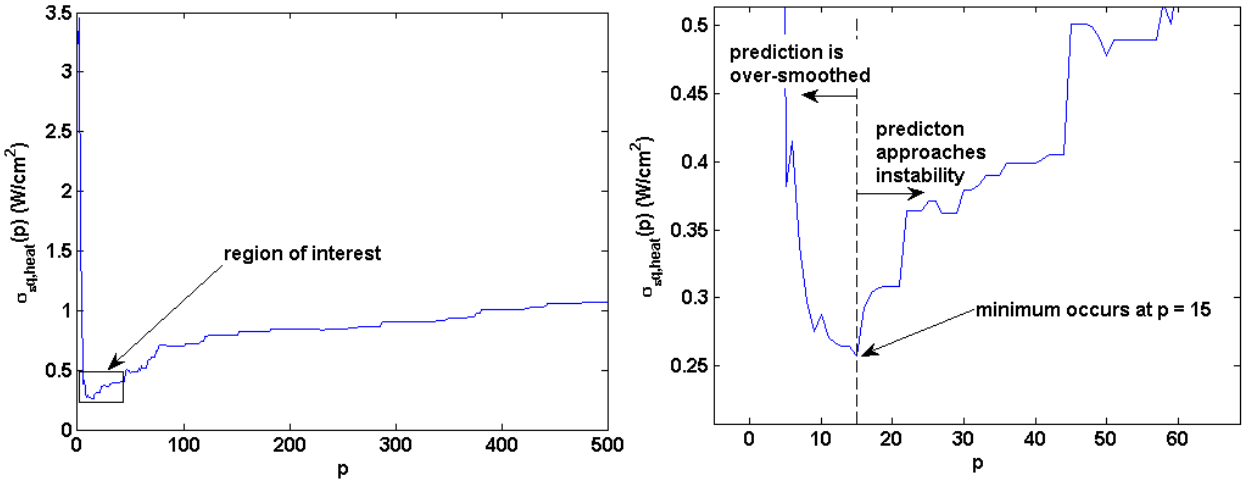

(a) (b)

Figure 4.32. 2pTC2 - Plot of $\sigma_{\varepsilon q,heat}(p)$ versus p for (a) The entire set of truncation indices $\{p\}_1^{500}$ and (b) Zoomed into the region of interest.

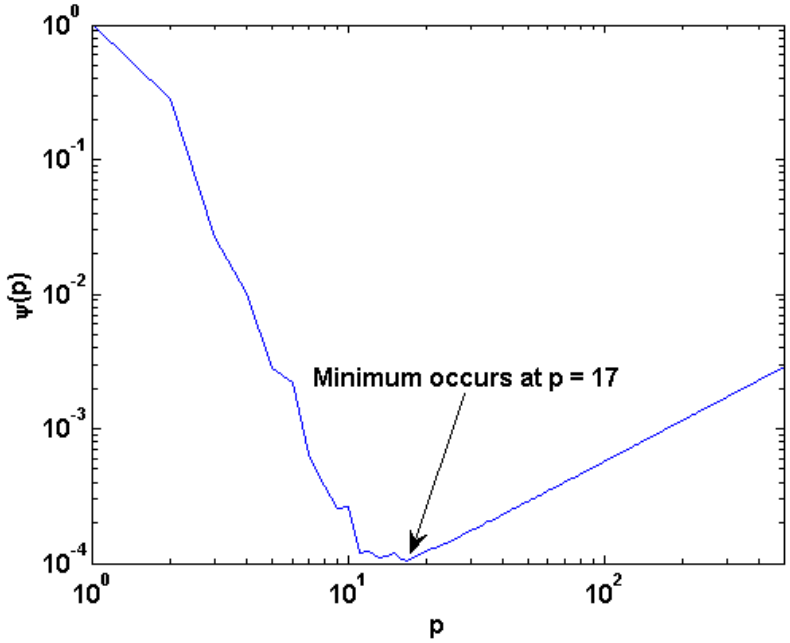

Figure 4.33. 2pTC2 - Log-log plot of $\psi(p)$ versus p. A distinct minimum is observed at p = 17.

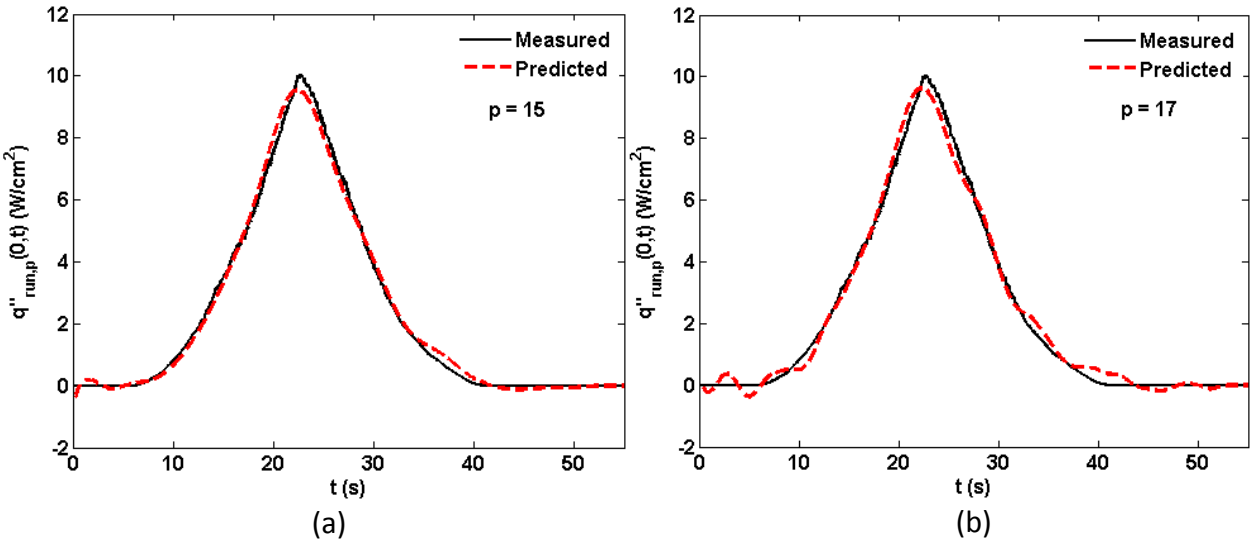

Figure 4.34. 2pTC2 - Plots of the predicted net surface heat flux $q''_{run,p}(0,t)$ at (a) p = 15 and (b) p = 17.

Table 4.8. 2pTC2 – Inverse Prediction Metrics. E = 128.39 J/cm^2, q''_{pk1}= 10.06 W/cm^2 @t = 22.66 s.

p	$\sigma_{\epsilon q}$ (W/cm^2)	$\sigma_{\epsilon q,heat}$ (W/cm^2)	E_p (J/cm^2)	E_p/E	$q''_{pk1,p}$ (W/cm^2)	$\frac{q''_{pk1,p}}{q''_{pk1}}$	$\Delta t_{pk1,p}$ (s)
15	0.211	0.257	127.79	0.995	9.53	0.95	-0.35
17	0.265	0.303	128.69	1.002	9.62	0.96	-0.47

From Figure 4.34 we can see that the prediction at p = 17 has slightly larger oscillations. The standard deviation of the error in prediction $\sigma_{\epsilon q}$ changes by 25% and that during the heating period $\sigma_{\epsilon q,heat}$ changes by 18%. The percentage changes are considerably higher as compared to 2pTC1. The prediction is definitely more sensitive to the value of p since a difference of 2 indices has been shown to produce relatively larger variations in the resolved heat flux. But as a standalone test case, the performance of the model is fairly satisfactory. On a visible level, the two predictions do not seem to be adversely affected by changing p from 15 to 17. Overall, the quality of the prediction obtained at p = 17, as suggested by the metric $\psi(p)$, matches quite well with the prediction obtained at the pre-determined p = 15, especially during the heating time. Again, the accuracy of the predicted heat flux peak ratio using p = 15 (ratio=0.995) and p = 17 (ratio=1.002) is remarkable and practically the same. The metric $\psi(p)$ performs in an acceptable fashion in indicating the correct region of optimum p.

2pTC3 -

This test case will consider data collected using Alumina as the electrical insulation. The data will be used to demonstrate the operation of the two-layer two probe calibration integral equation. The subsequent inverse results will show that even for longer duration data that are susceptible to the inherent non-linearity of the heat conduction physics, the reconstruction of the net surface heat flux is not adversely affected.

Again, we start by comparing the LHS = $g(t)$ and RHS = $f(t)$ of Eq. (A.17) and assessing the level of the base residual function $r(t)$ as shown in Figure 4.35.

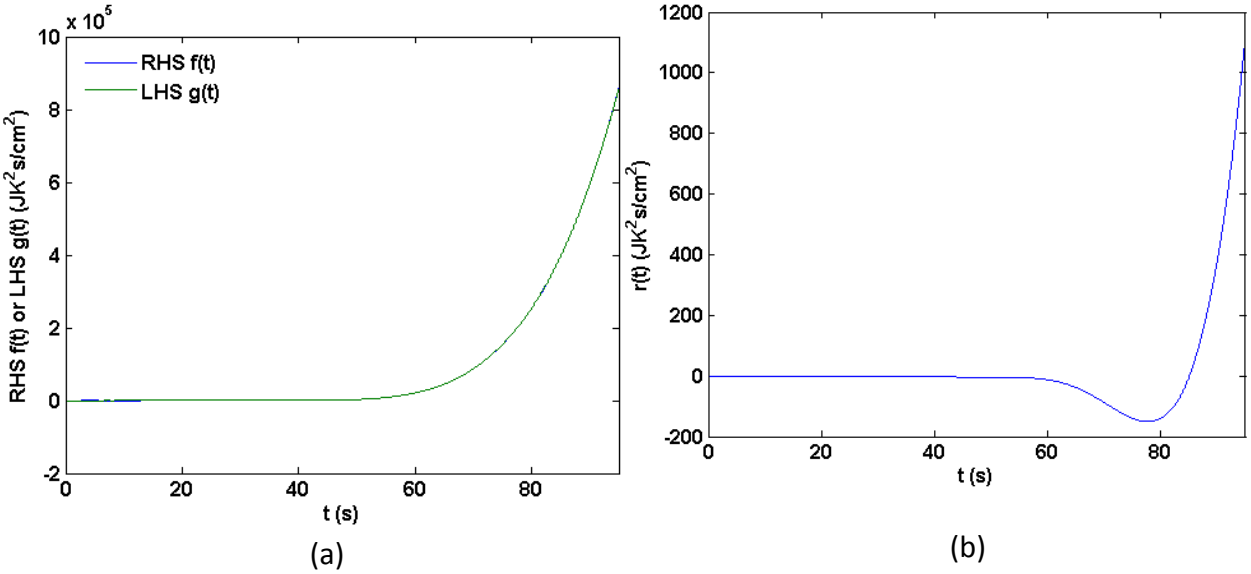

Figure 4.35. Pre-test diagnostic plots for 2pTC3; (a) Comparison of LHS and RHS of Eq. (A.17) and (b) base residual function $r(t)$.

From Figure 4.35 we can see that the base residual is three orders of magnitude smaller than the LHS (or RHS). The maximum absolute value of $r(t)$ is about 0.1 % of that of $f(t)$. The data provides excellent reconciliation of the two sides of Eq. (A.17) and bodes well for further analyses. The assessment of the kernel strength for this set of calibration data has been carried out in section 4.2.2 and the kernel has been plotted in Figure 4.22(b,c).

Pre-determination of an optimum value for the truncation index p is achieved by means of the standard deviation of the error in prediction during the whole time domain $\sigma_{\varepsilon q}(p)$ and during

the heating period $\sigma_{\varepsilon q,heat}(p)$. The plots for $\sigma_{\varepsilon q}(p)$ and $\sigma_{\varepsilon q,heat}(p)$ are shown in Figure 4.36 and Figure 4.37, respectively.

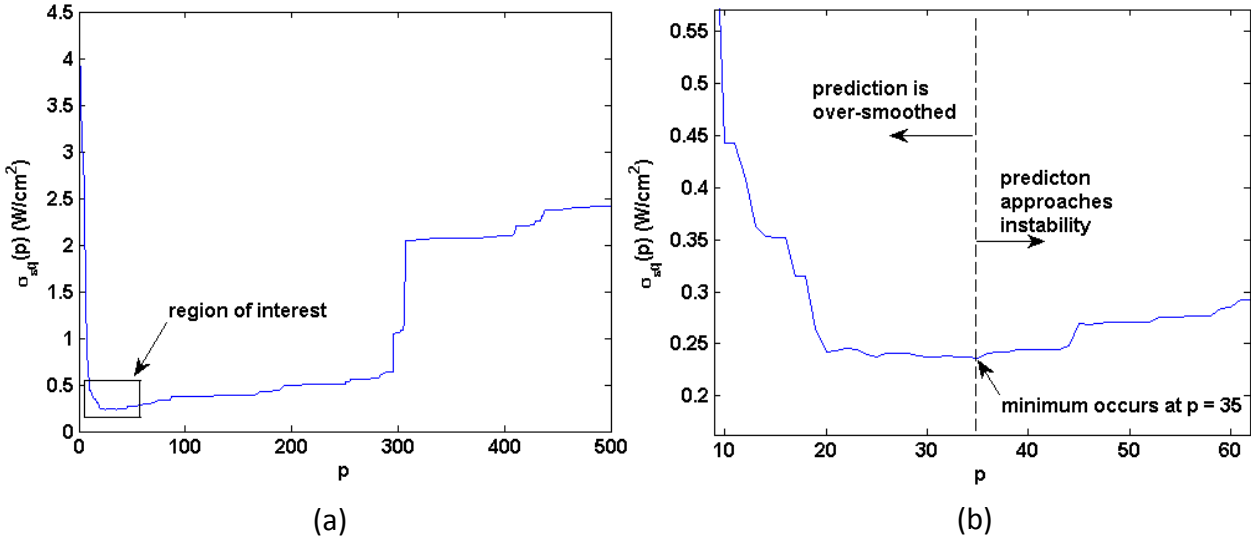

Figure 4.36. 2pTC3 - Plot of $\sigma_{\varepsilon q}(p)$ versus p for (a) The entire set of truncation indices $\{p\}_1^{500}$ and (b) Zoomed into the region of interest.

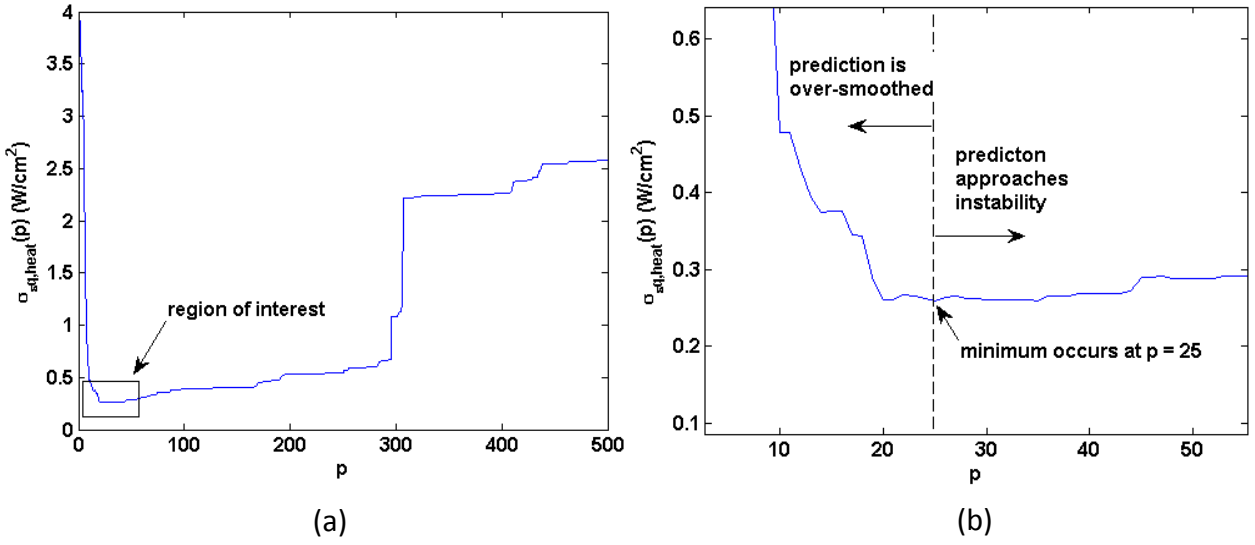

Figure 4.37. 2pTC3 - Plot of $\sigma_{\varepsilon q,heat}(p)$ versus p for (a) The entire set of truncation indices $\{p\}_1^{500}$ and (b) Zoomed into the region of interest.

In the test case 2pTC3, two different values for the pre-determined optimum truncation index p have been determined. Figure 4.36 suggests, $\sigma_{\varepsilon q}(p)$, the optimum value to be p = 35 whereas Figure 4.37, $\sigma_{\varepsilon q,heat}(p)$, indicates p = 25 as the optimum value. This can be an indicator of slightly larger oscillations in the error in prediction occurring during the heating period as compared to the lead and post time periods. The predictions will be made using both of these p values for comparison. We can also observe from Figures 4.36 and 4.37 the reappearance of a region of low sensitivity to p. This can help to explain the difference of 10 indices between the pre-determined values for optimum p. The estimation of a suitable p value determined by metric $\psi(p)$ is presented in Figure 4.38.

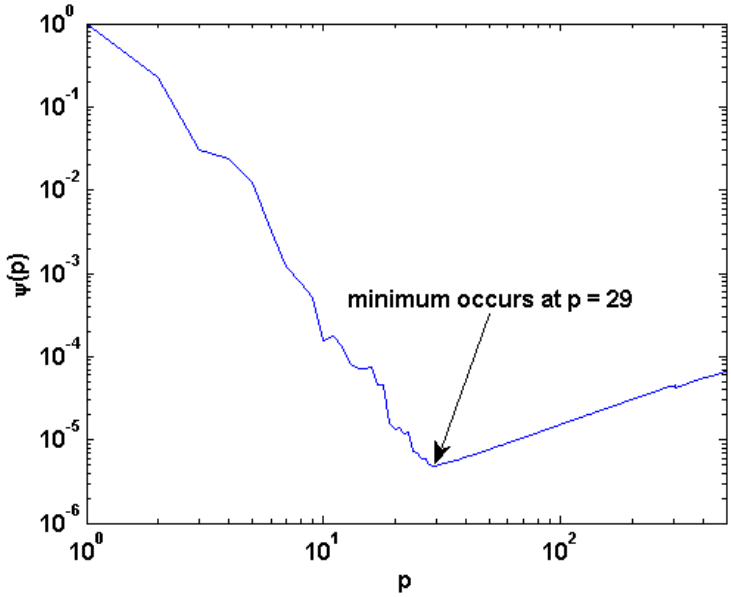

Figure 4.38. 2pTC3 - Log-log plot of $\psi(p)$ versus p. A distinct minimum is observed at p = 29.

The metric $\psi(p)$ suggests p = 29 as the optimum value and it is found to lie conveniently within the reference values of p = 25 and p = 35. Predictions using these values of p are shown in Figure 4.39. Also included is a prediction at p = 75 to observe the behavior of the model at high truncation indices. The associated metrics are presented in Table 4.9. The predictions shown in Figure 4.39 display excellent reconstruction of the first peak with good consistency for varying values of p. The second peak is shown to be under predicted and advanced in time, for all the values of p. Within the band of reference p values (25 and 35) the metrics shown in Table 4.9 remain almost constant. This is reflected by the flat region of insensitivity around the minimum

that was observed in Figures 4.36 and 4.37. Visibly, the predictions appear very smooth and stable with minimal oscillations.

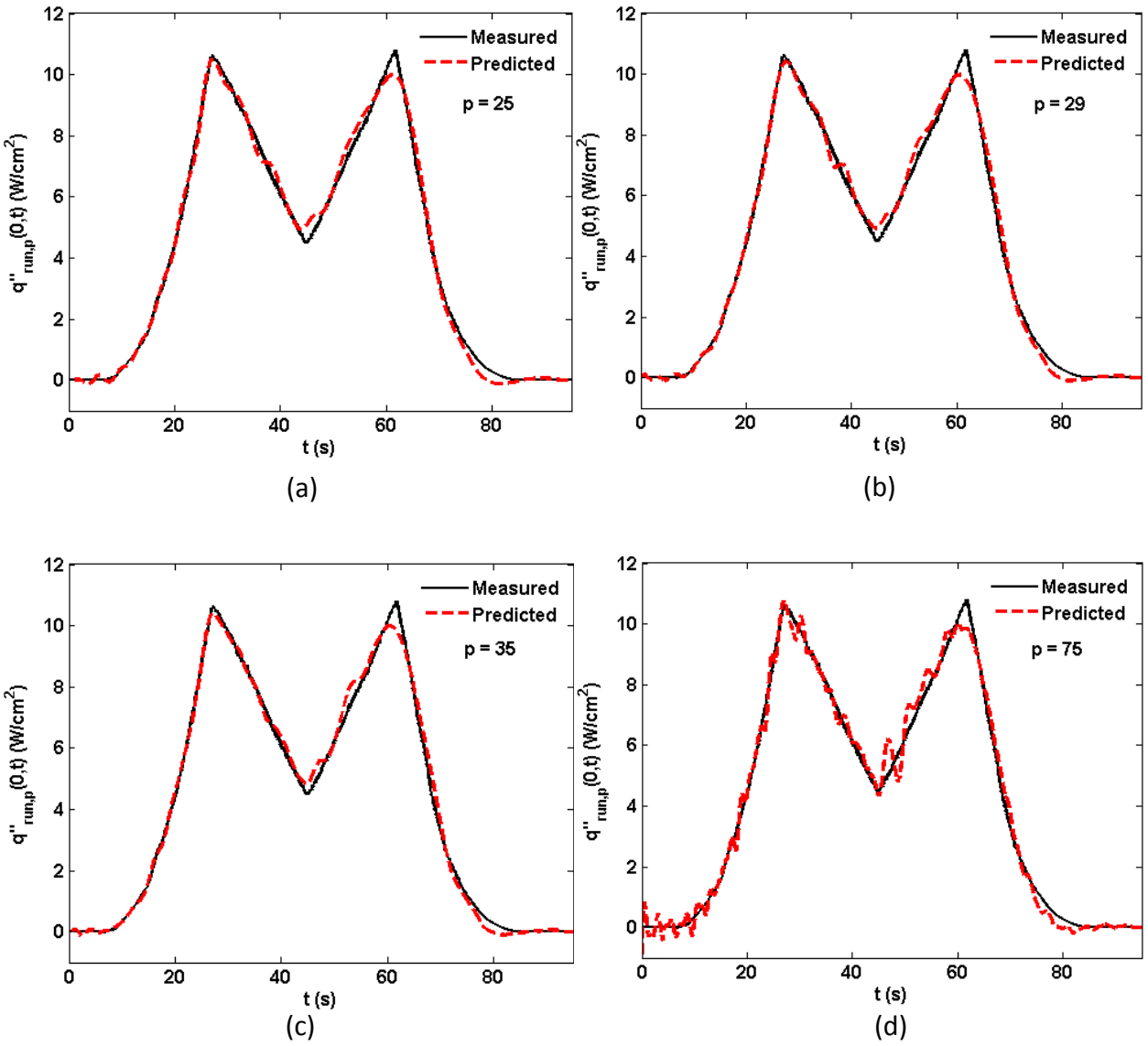

Figure 4.39. 2pTC3 - Plots of the predicted net surface heat flux $q''_{run,p}(0,t)$ at (a) p = 25, (b) p = 29, (c) p = 35 and (d) p = 75.

Table 4.9(a). 2pTC3 – Inverse Prediction Metrics. E = 404.91 J/cm^2.

p	$\sigma_{\epsilon q}$ (W/cm^2)	$\sigma_{\epsilon q,heat}$ (W/cm^2)	E_p (J/cm^2)	E_p/E
25	0.237	0.259	405.1	1
29	0.238	0.262	406.13	1.003
35	0.237	0.260	406.65	1.004
75	0.335	0.356	406.68	1.004

Table 4.9(b). 2pTC3 – Inverse Prediction Metrics. q''_{pk1}= 10.62 W/cm^2 @t = 27.1 s, q''_{pk2}= 10.8 W/cm^2 @t = 61.64 s.

p	$q''_{pk1,p}$ (W/cm^2)	$\frac{q''_{pk1,p}}{q''_{pk1}}$	$\Delta t_{pk1,p}$ (s)	$q''_{pk2,p}$ (W/cm^2)	$\frac{q''_{pk2,p}}{q''_{pk2}}$	$\Delta t_{pk2,p}$ (s)
25	10.49	0.98	0.06	9.99	0.93	-0.34
29	10.41	0.98	0.54	9.98	0.92	-1.24
35	10.43	0.98	0	10.01	0.93	-1.24
75	10.79	1.02	0	9.98	0.92	-1.66

Table 4.9(b) shows that for p =25 to 35 peak-1 ratio is constant at 0.98 and peak-2 ratios are 0.93 (p =25), 0.92 (p =29) and 0.93 (p =35) which suggests remarkable accuracy and stability. For the prediction obtained using p = 75, high frequency oscillations are produced and further increase in the truncation index p would eventually lead to instability. In yet another case the metric $\psi(p)$ has proved to be a very good indicator of the actual optimum band or a flat band of insensitivity around the optimal value.

4.3 CHAPTER SUMMARY

The operation of the one-probe and two-probe calibration integral equation methods for resolving the IHCP was successfully demonstrated using experimentally gathered data for short and long durations, single and two-layer domains. The high quality of the experimental data was emphasized by the consistently low magnitudes of the base residual function obtained for both one-probe and two-probe calibration methods. The suggested regularization schemes for both methods were shown to be robust and simple to implement. The results presented in this chapter lend significant merit to the applicability and ease of use of the physics based CIEM for resolving the IHCP.

CHAPTER 5. CONCLUSIONS AND FUTURE WORK

5.1 CONCLUSIONS

The one-probe and two-probe calibration integral equation methods (CIEM) for resolving the Inverse Heat Conduction Problem (IHCP) were validated using experimental data. The thought process behind the derivation of these equations was explained. The collected experimental data were shown to be of a high quality and adhered very well to the underlying assumptions of the calibration integral equation method. The applicability of the CIEM was expanded to two-layer domains and the two-probe CIEM enabled the reconstruction of the net surface heat flux independent of the back boundary condition during the real 'unknown' run. It was explained that the selection of the regularization scheme was dependent on the governing physics of the one–probe and two-probe CIEMSs. For the one-probe CIEM, a modified approach wherein an optimum band is established for the selection of the optimum regularization parameter was suggested. The idea was to develop a scheme based solely on the available calibration run temperature data. It was demonstrated that the suggested method worked very well for the reconstruction of varying surface heat flux profiles. For the two-probe CIEM, the proposed metric for the selection of the optimum truncation index p was shown to be robust and easy to implement. The operation of the one-probe and two-probe calibration integral equation methods for resolving the IHCP was successfully demonstrated using experimentally gathered data for short and long durations, single and two-layer domains. The high quality of the experimental data was emphasized by the consistently low magnitudes of the base residual function obtained for both one-probe and two-probe calibration methods. The results presented in Chapter 4 lend significant merit to the applicability and ease of use of the physics based CIEM for resolving the IHCP.

5.2 FUTURE WORK

The inherent simplicity of the derivation process of the physics based calibration method provides a strong and highly flexible foundation that allows the extension of the methodology to multi-dimensional and non-linear regimes. Presently, a non-linear model of the CIEM that accounts for the temperature dependence of the thermo-physical properties is under development. To improve the strength of the two-probe calibration kernel, improvements in the design of the calibration runs are being developed. The proposed calibration run stage would include active heating of both sample surfaces during calibration run 1, whereas during calibration run 2, one surface would be actively heated $\left(\frac{\partial T}{\partial t} > 0\right)$ and the other surface would

be cooled $\left(\frac{\partial T}{\partial t} < 0\right)$. It is expected that the largely varying boundary conditions at one surface accompanied by high levels of heating would produce a strong kernel with a significantly smaller effective elliptic time. The possibility of using the future-time regularization scheme for such a strong kernel can then be explored. Additionally, a physics based calibration approach applicable to multi-layer ablating domains is being devised. Ablation is an important concern for the aerospace industry and the physics based calibration approach being developed for the implicit characterization of recessing boundaries aims to achieve a significant step forward in this area of research.

LIST OF REFERENCES

[1] Beck, J.V., Blackwell, B., and St. Clair, C.R., Jr., *Inverse Heat Conduction: Ill-Posed Problems*, Wiley, New York, 1985.

[2] Ozisik, M.N., *Heat Conduction*, John Wiley and Sons, New York, 1980.

[3] Incropera, F.P. and DeWitt, D.P., *Fundamentals of Heat and Mass Transfer*, John Wiley & Sons Inc., New York, 5th edition.

[4] Ozisik, M.N. and Orlande, H.R.B., *Inverse Heat Transfer: Fundamentals and Applications*, Taylor and Francis, New York, 2000.

[5] Hadamard, J., *Lectures on Cauchy's Problem in Linear Partial Differential Equations*, Yale University Press, New Haven, CT, 1923.

[6] Frankel, J.I., Keyhani, M. and Elkins, B., "Surface Heat Flux Prediction Through Physics-Based Calibration-Part 1: Theory", *AIAA Journal of Thermophysics and Heat Transfer*, Vol. 27, No. 2, 2013, pp. 189-205.

[7] Elkins, B., Keyhani, M. and Frankel, J.I., "Surface Heat Flux Prediction Through Physics-Based Calibration-Part 2: Experimental Verification", *AIAA Journal of Thermophysics and Heat Transfer*, Vol. 27, No. 2, 2013, pp. 206-216.

[8] Frankel, J.I. and Keyhani, M., "Theoretical Development of a New Surface Heat Flux Calibration Method for Thin Film Resistive Temperature Gauges and Co-Axial Thermocouples", *Shock Waves*, Vol. 23, Issue 2, 2013, pp. 177-188.

[9] Chen, H., "*Two-Dimensional Formulation and Quasi-One-Dimensional Approximation to Inverse Heat Conduction by the Calibration Integral Equation Method (CIEM)*", M.S. Thesis, The University of Tennessee, Knoxville, TN, August 2013.

[10] Frankel, J.I., Keyhani, M., "*Transformative Inverse Heat Conduction Through Calibration",* The University of Tennessee, Knoxville, TN, 2011 (internal technical note).

[11] Stolz, G., Jr., "Numerical Solutions to an Inverse Problem of Heat Conduction for Simple Shapes", *Journal of Heat Transfer*, Vol. 82, 1960, pp. 20-26.

[12] Mirsepassi, T.J., "Heat-Transfer Charts for Time-Variable Boundary Conditions", *British Chemical Engineering,* 4, 1959, pp. 130-136.

[13] Mirsepassi, T.J., "Graphical Evaluation of a Convolution Integral", *Mathematical Tables Other Aides Computation*, 13, 1959, pp. 202-212.

[14] Shumakov, N.V., “A Method for the Experimental Study of the Process of Heating a Solid Body”, *Soviet Physics – Technical Physics*, (Translated by American Institute of Physics), Vol. 2, 1957, pp. 771-781.

[15] Beck, J.V., “Nonlinear Estimation Applied to the Nonlinear Heat Conduction Problem”, *International Journal of Heat and Mass Transfer*, Vol. 13, 1970, pp. 703-716.

[16] Monde, M., “Analytical Method in Inverse Heat Transfer Problem Using Laplace Transform Technique”, *International Journal of Heat and Mass Transfer*, Vol. 43, No. 21, 2000, pp. 3965-3975.

[17] Burggraf, O.R., “An Exact Solution of the Inverse Problem in Heat Conduction Theory and Application”, *Journal of Heat Transfer*, Vol. 86, 1964, pp. 373–382.

[18] Tikhonov, A.N. and Arsenin, V.Y., *Solution of Ill-Posed Problems*, V. H. Winston & Sons, Washington, D. C., 1977.

[19] Engl, H.W., Hanke, M., and Neubauer, A., *Regularization of Inverse Problems*, Dordrecht: Kluwer Academic Publishers, 2000.

[20] Morozov, V.A., *Methods for Solving Incorrectly Posed Problems*, New York: Springer, 1984.

[21] Hansen, P.C., “Analysis of Discrete Ill-Posed Problems by Means of the L-Curve”, *SIAM Review*, Vol. 34, No. 4, 1992, pp. 561–580.

[22] Hansen, M., Limitations of the L-Curve Method in Ill-Posed Problems, *BIT Numerical Mathematics*, Vol. 36, No. 2, 1996, pp. 287–301.

[23] Carasso, A.S., “Space Marching Finite Difference Schemes in the Nonlinear Inverse Heat Conduction Problem”*, Inverse Problems*, Vol. 8, No. 1, 1992, pp. 25-43.

[24] Carasso, A.S., “Slowly Divergent Space Marching Schemes in the Inverse Heat Conduction Problem”, *Numerical Heat Transfer, Part B*, Vol. 23, No. 1, 1993, pp. 111–126.

[25] Zhou, J., Zhang, Y., Chen, J.K. and Feng, Z.C., “Inverse Heat Conduction Using Measured Back Surface Temperature and Heat Flux”, *AIAA Journal of Thermophysics and Heat Transfer*, Vol. 24, No. 1, 2010, pp. 95-103.

[26] Elkins, B.S., Keyhani, M., and Frankel, J.I., “Global Time Method for Inverse Heat Conduction Problem”, *Inverse Problems in Science and Engineering*, Vol. 20, No. 5, 2012, pp. 651-664.

[27] Frankel, J.I., "Regularization of Inverse Heat Conduction by Combination of Rate Sensor Analysis and Analytic Continuation", *Journal of Engineering Mathematics*, Vol. 57, No. 2, 2007, pp. 181-198.

[28] Golub, G. and Van Loan, C., *Matrix Computations*, The Johns Hopkins University Press, Baltimore, 1998.

[29] Strang, G., *Linear Algebra and its Applications*, Cengage Learning, 4th edition, 2005.

[30] Fierro, R. D., Golub, G. H., Hansen, P. C. and O'Leary, D. P., "Regularization by Truncated Total Least Squares", *SIAM Journal on Scientific Computing*, Vol. 18, No. 4, July 1997, pp. 1223-1241.

[31] Shenefelt, J.R., Luck, R., Taylor, R.P. and Berry, J.T., "Solution to Inverse Heat Conduction Problems Employing Singular Value Decomposition and Model-Reduction, *International Journal of Heat and Mass Transfer*, Vol. 45, 2002, pp. 67-74.

[32] Loehle, S., Battaglia, J.L., Batsale, J.C., Enouf, O., Dubard, J. and Filtz, J.R., "Characterization of a Heat Flux Sensor Using Short Pulse Laser Calibration", *Review of Scientific Instrumentation*, Vol. 78, No. 5, 2007, pp. 053501(6).

[33] Battaglia, J.L., Cois, O., Puigsegur, L. and Oustaloup, A., "Solving an Inverse Heat Conduction Problem Using a Non-Integer Identified Model", *International Journal of Heat and Mass Transfer*, Vol. 44, No. 14, 2001, pp. 2671–2680.

[34] Linz, P., *Analytical and Numerical Methods for Volterra Equations*, SIAM, Philadelphia, PA, 1985.

[35] Lamm, P.K., "A Survey of Regularization Methods for First-Kind Volterra Equations", (in Surveys on Solution Methods for Inverse Problems) Eds.: D. Colton, H. W. Engl, A. Louis, J. R. McLaughlin, W. Rundell, Springer (Vienna, New York), pp. 53-82, 2000.

[36] Plewa, J., Elkins, B.S., Keyhani, M. and Frankel, J.I., "Heat Transfer Analysis Via Rate Based Sensors", *50th AIAA Aerospace Sciences Meeting and Exhibit, Nashville, TN*, January 9-12, 2012 (AIAA-2012-0810).

[37] Plewa, J.E., "*Heat Transfer Analysis Via Rate Based Sensors*", M.S. Thesis, The University of Tennessee, Knoxville, TN, December 2012.

[38] NIST, “ITS-90 Thermocouple Database”, http://srdata.nist.gov/its90/download/download.html, 1995

[39] Elkins, B.S., “Challenges for the Accurate Determination of the Surface Thermal Condition via In-Depth Sensor Data”, Ph.D. Dissertation, The University of Tennessee, Knoxville, TN, August 2011.

[40] “*Thermal Performance of Fire Resistive Materials - I. Characterization with respect to thermal performance models*”, National Institute of Standards and Technology, NISTIR 7401.

[41] Beck, J.V., Blackwell, B. and Haji-Sheikh, A., “Comparison of Some Inverse Heat Conduction Methods Using Experimental Data”, *International Journal of Heat and Mass Transfer*, Vol. 39, No. 17, 1996, pp. 3649-3657.

[42] Schiff, J.L., *The Laplace Transform: Theory and Applications*, Springer-Verlag New York, Inc., 1999.

APPENDICES

APPENDIX A. DERIVATION OF THE ONE-DIMENSIONAL TWO-PROBE LINEAR CALIBRATION INTEGRAL EQUATION FOR A TWO-LAYER DOMAIN

The derivation of the linear two-probe calibration integral equation for a two-layer domain is now presented. Consider the two-layer problem per Figure A.1 and defined as

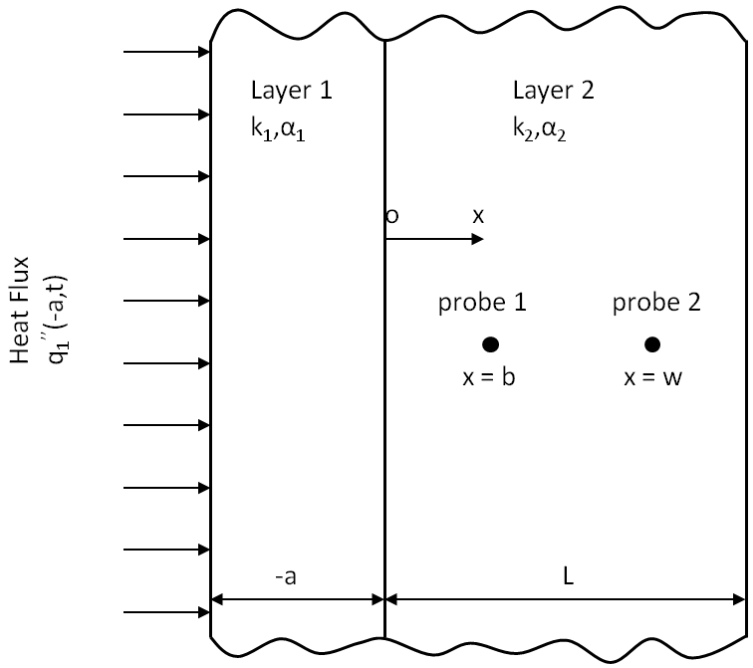

Figure A.1. Schematic of the two-layer domain. Thermocouples are installed at 'x=b' and 'x=w' positions.

$$\frac{1}{\alpha_1}\frac{\partial T_1}{\partial t}(x,t) = \frac{\partial^2 T_1}{\partial x^2}(x,t), \quad x \in [-a, 0], \qquad t \geq 0, \tag{A.1a}$$

$$\frac{1}{\alpha_2}\frac{\partial T_2}{\partial t}(x,t) = \frac{\partial^2 T_2}{\partial x^2}(x,t), \quad x \in [0, L], \qquad t \geq 0, \tag{A.1b}$$

subject to the boundary and interfacial conditions

$$q_1^{"}(-a,t) = -k_1 \frac{\partial T_1}{\partial x}(-a,t), \quad t > 0, \tag{A.2a}$$

$$T_1(0,t) = T_2(0,t), \tag{A.2b}$$

$$q_1^{"}(0,t) = q_2^{"}(0,t), \tag{A.2c}$$

and the initial condition

$$T_1(x,0) = T_2(x,0) = T_o\,, \quad x \in [-a, L], \tag{A.2d}$$

with temperature measurements (known) at two in-depth locations

$$T_2(b,t) = T_b(t)\,, \;\; t \geq 0, \tag{A.2e}$$

$$T_2(w,t) = T_w(t)\,, \;\; t \geq 0, \tag{A.2f}$$

where the first layer is denoted by subscript '1', the second layer by subscript '2', k is the thermal conductivity, α is the thermal diffusivity and a is the thickness of the first layer. The origin is deliberately located at the interface for practical reasons that will be understood as the derivation progresses. For simplicity and without loss of generality, we let $T_o = 0°C$ in Eq. (A.2d).

The calibration approach requires the algebratization of Eqs. (A.1a,b), subject to Eqs. (A.2a-f) by means of the Laplace Transform [42] wherein the time variable 't' is transformed into the frequency variable 's'.

The Laplace Transform of a function $f(t)$ is given by [42]

$$\mathcal{L}\{f(t)\} = \hat{f}(s) = \int_{t=0}^{\infty} e^{-st} f(t) ds\,, \;\; s \geq 0, \tag{A.3a}$$

where $\mathcal{L}$ is the Laplace Transform operator. The Laplace three-term convolution integral is [10,42]

$$\hat{f}(s) * \hat{g}(s) * \hat{h}(s) = \mathcal{L}\left\{ \int_{u=0}^{t} f(u) \int_{r=0}^{t-u} g(r)\, h(t-u-r) dr du \right\}, \;\; s \geq 0, \tag{A.3b}$$

whereas the inverse is [10,42]

$$\mathcal{L}^{-1}\{\hat{f}(s) * \hat{g}(s) * \hat{h}(s)\} = \int_{u=0}^{t} f(u) \int_{r=0}^{t-u} g(r)\, h(t-u-r) dr du\,, \quad t \geq 0. \tag{A.3c}$$

The objective is to relate the surface heat flux at $x = -a$ to the in-depth probe temperature measurements at $x = b$ and $x = w$. Starting with Layer 2, we take the Laplace Transform of Eq. (A.1b) subject to the trivial initial condition given by Eq. (A.2d), where $T_o = 0°C$, to get

$$\frac{1}{\alpha_2}\left(s\hat{T}_2(x,s) - T_2(x,0)\right) = \frac{d^2\hat{T}_2}{dx^2}(x,s)\,, \qquad x \in [0,L], \qquad s \geq 0. \tag{A.4a}$$

Rearranging, we get

$$\frac{d^2\hat{T}_2}{dx^2}(x,s) - \frac{s}{\alpha_2}\hat{T}_2(x,s) = 0, \quad x \in [0,L], \qquad s \geq 0, \tag{A.4b}$$

whose general solution is given by

$$\hat{T}_2(x,s) = A(s)\cosh\left(\sqrt{\frac{s}{\alpha_2}}x\right) + B(s)\sinh\left(\sqrt{\frac{s}{\alpha_2}}x\right), \qquad x \in [0,L], s \geq 0. \tag{A.4c}$$

The unknown coefficients $A(s)$ and $B(s)$ will be determined with the help of the interface conditions as per Eqs. (A.2b-c). This would first require the expression for the heat flux in the transformed domain which can be easily obtained by Fourier's Law as

$$\hat{q}_2^{"}(x,s) = -k_2\frac{d\hat{T}_2}{dx}(x,s), \quad x \in [0,L], s \geq 0, \tag{A.5a}$$

which leads us to

$$\hat{q}_2^{"}(x,s) = -k_2\sqrt{\frac{s}{\alpha_2}}\left[A(s)\sinh\left(\sqrt{\frac{s}{\alpha_2}}x\right) + B(s)\cosh\left(\sqrt{\frac{s}{\alpha_2}}x\right)\right], \quad x \in [0,L], s \geq 0. \tag{A.5b}$$

Solving for the interfacial temperature yields

$$\hat{T}_2(0,s) = A(s), \quad s \geq 0, \tag{A.6a}$$

and solving for the interfacial heat flux yields

$$\hat{q}_2^{"}(0,s) = -k_2\sqrt{\frac{s}{\alpha_2}}B(s), \quad s \geq 0, \tag{A.6b}$$

which upon rearranging gives us the expression for $B(s)$

$$B(s) = -\frac{1}{k_2}\sqrt{\frac{\alpha_2}{s}}\,\hat{q}_2^{"}(0,s), \quad s \geq 0. \tag{A.6c}$$

Substituting Eqs. (A.6a,c) into Eq. (A.4c), we get

$$\hat{T}_2(x,s) = \hat{T}_2(0,s)\cosh\left(\sqrt{\frac{s}{\alpha_2}}x\right) - \frac{1}{k_2}\sqrt{\frac{\alpha_2}{s}}\,\hat{q}_2^{"}(0,s)\sinh\left(\sqrt{\frac{s}{\alpha_2}}x\right), x \in [0,L], s \geq 0. \tag{A.7a}$$

Evaluating Eq. (A.7a) at each of the probe locations b and w, we now have

$$\hat{T}_2(b,s) = \left[\cosh\left(\sqrt{\frac{s}{\alpha_2}}b\right)\right]\hat{T}_2(0,s) - \left[\frac{1}{k_2}\sqrt{\frac{\alpha_2}{s}}\,\sinh\left(\sqrt{\frac{s}{\alpha_2}}b\right)\right]\hat{q}_2^{"}(0,s), \quad x \in [0,L],\ s \geq 0, \tag{A.7b}$$

and

$$\hat{T}_2(w,s) = \left[\cosh\left(\sqrt{\frac{s}{\alpha_2}}w\right)\right]\hat{T}_2(0,s) - \left[\frac{1}{k_2}\sqrt{\frac{\alpha_2}{s}}\,\sinh\left(\sqrt{\frac{s}{\alpha_2}}w\right)\right]\hat{q}_2^{"}(0,s), \quad x \in [0,L],\ s \geq 0. \tag{A.7c}$$

Using Cramer's Rule, we can now develop expressions for the interfacial temperature and heat flux in terms of the in-depth temperature measurements as

$$\hat{\boldsymbol{T}}_{\boldsymbol{2}}(\boldsymbol{0},\boldsymbol{s}) = \frac{\hat{\boldsymbol{T}}_{\boldsymbol{2}}(\boldsymbol{b},\boldsymbol{s})\sinh\left(\sqrt{\frac{s}{\alpha_2}}w\right) - \hat{\boldsymbol{T}}_{\boldsymbol{2}}(\boldsymbol{w},\boldsymbol{s})\sinh\left(\sqrt{\frac{s}{\alpha_2}}b\right)}{\cosh\left(\sqrt{\frac{s}{\alpha_2}}b\right)\sinh\left(\sqrt{\frac{s}{\alpha_2}}w\right) - \cosh\left(\sqrt{\frac{s}{\alpha_2}}w\right)\sinh\left(\sqrt{\frac{s}{\alpha_2}}b\right)}, \qquad s \geq 0, \tag{A.8a}$$

$$\widehat{\boldsymbol{q}}_{\boldsymbol{2}}^{"}(\boldsymbol{0},\boldsymbol{s}) = \frac{\widehat{\boldsymbol{T}}_{\boldsymbol{2}}(\boldsymbol{b},\boldsymbol{s})k_2\sqrt{\frac{s}{\alpha_2}}\cosh\left(\sqrt{\frac{s}{\alpha_2}}w\right) - \widehat{\boldsymbol{T}}_{\boldsymbol{2}}(\boldsymbol{w},\boldsymbol{s})k_2\sqrt{\frac{s}{\alpha_2}}\cosh\left(\sqrt{\frac{s}{\alpha_2}}b\right)}{\cosh\left(\sqrt{\frac{s}{\alpha_2}}b\right)\sinh\left(\sqrt{\frac{s}{\alpha_2}}w\right) - \cosh\left(\sqrt{\frac{s}{\alpha_2}}w\right)\sinh\left(\sqrt{\frac{s}{\alpha_2}}b\right)}, \qquad s \geq 0. \quad \text{(A.8b)}$$

Equations (A.2b,c) are valid with the assumption of perfect thermal contact (zero contact resistance). This allows us to merely rewrite Eqs. (A.8a,b) for $\hat{T}_1(0,s)$ and $\hat{q}_1^{"}(0,s)$ as

$$\widehat{\boldsymbol{T}}_{\boldsymbol{1}}(\boldsymbol{0},\boldsymbol{s}) = \frac{\widehat{\boldsymbol{T}}_{\boldsymbol{2}}(\boldsymbol{b},\boldsymbol{s})\sinh\left(\sqrt{\frac{s}{\alpha_2}}w\right) - \widehat{\boldsymbol{T}}_{\boldsymbol{2}}(\boldsymbol{w},\boldsymbol{s})\sinh\left(\sqrt{\frac{s}{\alpha_2}}b\right)}{\cosh\left(\sqrt{\frac{s}{\alpha_2}}b\right)\sinh\left(\sqrt{\frac{s}{\alpha_2}}w\right) - \cosh\left(\sqrt{\frac{s}{\alpha_2}}w\right)\sinh\left(\sqrt{\frac{s}{\alpha_2}}b\right)}, \qquad s \geq 0, \quad \text{(A.8c)}$$

$$\widehat{\boldsymbol{q}}_{\boldsymbol{1}}^{"}(\boldsymbol{0},\boldsymbol{s}) = \frac{\widehat{\boldsymbol{T}}_{\boldsymbol{2}}(\boldsymbol{b},\boldsymbol{s})k_2\sqrt{\frac{s}{\alpha_2}}\cosh\left(\sqrt{\frac{s}{\alpha_2}}w\right) - \widehat{\boldsymbol{T}}_{\boldsymbol{2}}(\boldsymbol{w},\boldsymbol{s})k_2\sqrt{\frac{s}{\alpha_2}}\cosh\left(\sqrt{\frac{s}{\alpha_2}}b\right)}{\cosh\left(\sqrt{\frac{s}{\alpha_2}}b\right)\sinh\left(\sqrt{\frac{s}{\alpha_2}}w\right) - \cosh\left(\sqrt{\frac{s}{\alpha_2}}w\right)\sinh\left(\sqrt{\frac{s}{\alpha_2}}b\right)}, \qquad s \geq 0. \quad \text{(A.8d)}$$

Next, we take the Laplace Transform of Eq. (A.1a) subject to the trivial initial condition as per Eq. (A.2d) to get

$$\frac{1}{\alpha_1}\left(s\hat{T}_1(x,s) - T_1(x,0)\right) = \frac{d^2\hat{T}_1}{dx^2}(x,s), \qquad x \in [-a,0], s \geq 0. \quad \text{(A.9a)}$$

Rearranging, we get

$$\frac{d^2\hat{T}_1}{dx^2}(x,s) - \frac{s}{\alpha_1}\hat{T}_1(x,s) = 0, \quad x \in [-a,0], s \geq 0, \quad \text{(A.9b)}$$

whose general solution is given by

$$\hat{T}_1(x,s) = C(s)\cosh\left(\sqrt{\frac{s}{\alpha_1}}x\right) + D(s)\sinh\left(\sqrt{\frac{s}{\alpha_1}}x\right), \qquad x \in [-a,0], s \geq 0. \quad \text{(A.9c)}$$

The unknown coefficients $C(s)$ and $D(s)$ will be determined with the help of the interface conditions as per Eqs. (A.2b-c). This would first require the expression for the heat flux in the transformed domain which can be easily obtained by Fourier's Law

$$\hat{q}_1^{"}(x,s) = -k_1 \frac{d\hat{T}_1}{dx}(x,s), \quad x \in [-a,0], s \geq 0, \tag{A.10a}$$

which leads us to

$$\hat{q}_1^{"}(x,s) = -k_1 \sqrt{\frac{s}{\alpha_1}} \left[C(s) \sinh\left(\sqrt{\frac{s}{\alpha_1}} x \right) + D(s) \cosh\left(\sqrt{\frac{s}{\alpha_1}} x \right) \right], \quad x \in [-a,0], s \geq 0. \tag{A.10b}$$

Solving for the interfacial temperature yields

$$\hat{T}_1(0,s) = C(s), \quad s \geq 0. \tag{A.11a}$$

Solving for the interfacial heat flux yields

$$\hat{q}_1^{"}(0,s) = -k_1 \sqrt{\frac{s}{\alpha_1}} D(s), \quad s \geq 0, \tag{A.11b}$$

or upon rearranging, we get the expression for $D(s)$

$$D(s) = -\frac{1}{k_1} \sqrt{\frac{\alpha_1}{s}}\, \hat{q}_1^{"}(0,s), \quad s \geq 0. \tag{A.11c}$$

Now, we need to relate the surface heat flux to the two in-depth probes via the interfacial conditions. Therefore, we evaluate Eq. (A.10b) at $x = -a$ and substitute for the unknown coefficients from Eqs. (A.11a,c) to get

$$\hat{q}_1^{"}(-a,s) = -k_1 \sqrt{\frac{s}{\alpha_1}} \left[\hat{T}_1(0,s) \sinh\left(\sqrt{\frac{s}{\alpha_1}}(-a) \right) - \frac{1}{k_1} \sqrt{\frac{\alpha_1}{s}}\, \hat{q}_1^{"}(0,s) \cosh\left(\sqrt{\frac{s}{\alpha_1}}(-a) \right) \right],$$

$$s \geq 0. \tag{A.12a}$$

Upon rearranging and simplifying, we now have

$$\widehat{\boldsymbol{q}}_{\boldsymbol{1}}^{"}(-\boldsymbol{a},\boldsymbol{s}) = k_1\sqrt{\frac{s}{\alpha_1}}\sinh\left(\sqrt{\frac{s}{\alpha_1}}a\right)\widehat{\boldsymbol{T}}_{\boldsymbol{1}}(\boldsymbol{0},\boldsymbol{s}) + \cosh\left(\sqrt{\frac{s}{\alpha_1}}a\right)\widehat{\boldsymbol{q}}_{\boldsymbol{1}}^{"}(\boldsymbol{0},\boldsymbol{s}), \qquad s \geq 0. \tag{A.12b}$$

Equation (A.12b) relates the surface heat flux with the interfacial conditions. We can now propagate to the in-depth probes by substituting Eqs. (A.8c,d) into Eq. (A.12b) to obtain

$$\begin{aligned}
&\widehat{\boldsymbol{q}}_{\boldsymbol{1}}^{"}(-\boldsymbol{a},\boldsymbol{s}) \\
&= k_1\sqrt{\frac{s}{\alpha_1}}\sinh\left(\sqrt{\frac{s}{\alpha_1}}a\right)\left[\frac{\widehat{\boldsymbol{T}}_{\boldsymbol{2}}(\boldsymbol{b},\boldsymbol{s})\sinh\left(\sqrt{\frac{s}{\alpha_2}}w\right) - \widehat{\boldsymbol{T}}_{\boldsymbol{2}}(\boldsymbol{w},\boldsymbol{s})\sinh\left(\sqrt{\frac{s}{\alpha_2}}b\right)}{\cosh\left(\sqrt{\frac{s}{\alpha_2}}b\right)\sinh\left(\sqrt{\frac{s}{\alpha_2}}w\right) - \cosh\left(\sqrt{\frac{s}{\alpha_2}}w\right)\sinh\left(\sqrt{\frac{s}{\alpha_2}}b\right)}\right] \\
&+ \cosh\left(\sqrt{\frac{s}{\alpha_1}}a\right)\left[\frac{\widehat{\boldsymbol{T}}_{\boldsymbol{2}}(\boldsymbol{b},\boldsymbol{s})k_2\sqrt{\frac{s}{\alpha_2}}\cosh\left(\sqrt{\frac{s}{\alpha_2}}w\right) - \widehat{\boldsymbol{T}}_{\boldsymbol{2}}(\boldsymbol{w},\boldsymbol{s})k_2\sqrt{\frac{s}{\alpha_2}}\cosh\left(\sqrt{\frac{s}{\alpha_2}}b\right)}{\cosh\left(\sqrt{\frac{s}{\alpha_2}}b\right)\sinh\left(\sqrt{\frac{s}{\alpha_2}}w\right) - \cosh\left(\sqrt{\frac{s}{\alpha_2}}w\right)\sinh\left(\sqrt{\frac{s}{\alpha_2}}b\right)}\right], \\
&\qquad\qquad s \geq 0.
\end{aligned} \tag{A.12c}$$

Upon regrouping, we get

$$\begin{aligned}
&\widehat{\boldsymbol{q}}_{\boldsymbol{1}}^{"}(-\boldsymbol{a},\boldsymbol{s}) \\
&= \left[\frac{k_1\sqrt{\frac{s}{\alpha_1}}\sinh\left(\sqrt{\frac{s}{\alpha_1}}a\right)\sinh\left(\sqrt{\frac{s}{\alpha_2}}w\right) + k_2\sqrt{\frac{s}{\alpha_2}}\cosh\left(\sqrt{\frac{s}{\alpha_1}}a\right)\cosh\left(\sqrt{\frac{s}{\alpha_2}}w\right)}{\cosh\left(\sqrt{\frac{s}{\alpha_2}}b\right)\sinh\left(\sqrt{\frac{s}{\alpha_2}}w\right) - \cosh\left(\sqrt{\frac{s}{\alpha_2}}w\right)\sinh\left(\sqrt{\frac{s}{\alpha_2}}b\right)}\right]\widehat{\boldsymbol{T}}_{\boldsymbol{2}}(\boldsymbol{b},\boldsymbol{s}) \\
&- \left[\frac{k_1\sqrt{\frac{s}{\alpha_1}}\sinh\left(\sqrt{\frac{s}{\alpha_1}}a\right)\sinh\left(\sqrt{\frac{s}{\alpha_2}}b\right) + k_2\sqrt{\frac{s}{\alpha_2}}\cosh\left(\sqrt{\frac{s}{\alpha_1}}a\right)\cosh\left(\sqrt{\frac{s}{\alpha_2}}b\right)}{\cosh\left(\sqrt{\frac{s}{\alpha_2}}b\right)\sinh\left(\sqrt{\frac{s}{\alpha_2}}w\right) - \cosh\left(\sqrt{\frac{s}{\alpha_2}}w\right)\sinh\left(\sqrt{\frac{s}{\alpha_2}}b\right)}\right]\widehat{\boldsymbol{T}}_{\boldsymbol{2}}(\boldsymbol{w},\boldsymbol{s}), \\
&\qquad\qquad s \geq 0.
\end{aligned} \tag{A.12d}$$

Expressing Eq. (A.12d) in compact form, we get

$$\widehat{\boldsymbol{q}}_{\boldsymbol{1}}^{"}(-\boldsymbol{a},\boldsymbol{s}) = \widehat{M}(k_1,k_2,\alpha_1,\alpha_2,a,b,w;s)\widehat{\boldsymbol{T}}_{\boldsymbol{2}}(\boldsymbol{b},\boldsymbol{s}) - \widehat{N}(k_1,k_2,\alpha_1,\alpha_2,a,b,w;s)\widehat{\boldsymbol{T}}_{\boldsymbol{2}}(\boldsymbol{w},\boldsymbol{s}), \quad s \geq 0, \tag{A.13a}$$

where

$$\widehat{M}(k_1, k_2, \alpha_1, \alpha_2, a, b, w; s) \triangleq$$

$$\left[\frac{k_1\sqrt{\frac{s}{\alpha_1}}\sinh\left(\sqrt{\frac{s}{\alpha_1}}a\right)\sinh\left(\sqrt{\frac{s}{\alpha_2}}w\right) + k_2\sqrt{\frac{s}{\alpha_2}}\cosh\left(\sqrt{\frac{s}{\alpha_1}}a\right)\cosh\left(\sqrt{\frac{s}{\alpha_2}}w\right)}{\cosh\left(\sqrt{\frac{s}{\alpha_2}}b\right)\sinh\left(\sqrt{\frac{s}{\alpha_2}}w\right) - \cosh\left(\sqrt{\frac{s}{\alpha_2}}w\right)\sinh\left(\sqrt{\frac{s}{\alpha_2}}b\right)}\right], \quad \text{(A.13b)}$$

and

$$\widehat{N}(k_1, k_2, \alpha_1, \alpha_2, a, b, w; s) \triangleq$$

$$\left[\frac{k_1\sqrt{\frac{s}{\alpha_1}}\sinh\left(\sqrt{\frac{s}{\alpha_1}}a\right)\sinh\left(\sqrt{\frac{s}{\alpha_2}}b\right) + k_2\sqrt{\frac{s}{\alpha_2}}\cosh\left(\sqrt{\frac{s}{\alpha_1}}a\right)\cosh\left(\sqrt{\frac{s}{\alpha_2}}b\right)}{\cosh\left(\sqrt{\frac{s}{\alpha_2}}b\right)\sinh\left(\sqrt{\frac{s}{\alpha_2}}w\right) - \cosh\left(\sqrt{\frac{s}{\alpha_2}}w\right)\sinh\left(\sqrt{\frac{s}{\alpha_2}}b\right)}\right]. \quad \text{(A.13c)}$$

The functions $\widehat{M}(k_1, k_2, \alpha_1, \alpha_2, a, b, w; s)$ and $\widehat{N}(k_1, k_2, \alpha_1, \alpha_2, a, b, w; s)$ carry the physics of diffusion and relevant information regarding the thermo-physical properties and the probe positions. For a given domain as per Figure A.1, these functions remain constant.

This suggests that with two separate experimental 'calibration runs', $\widehat{M}(k_1, k_2, \alpha_1, \alpha_2, a, b, w; s)$ and $\widehat{N}(k_1, k_2, \alpha_1, \alpha_2, a, b, w; s)$ can be solved for following

$$\widehat{\boldsymbol{q}}^{"}_{\boldsymbol{cal1}}(-\boldsymbol{a}, \boldsymbol{s}) = \widehat{M}(k_1, k_2, \alpha_1, \alpha_2, a, b, w; s)\widehat{\boldsymbol{T}}_{\boldsymbol{cal1}}(\boldsymbol{b}, \boldsymbol{s}) - \widehat{N}(k_1, k_2, \alpha_1, \alpha_2, a, b, w; s)\widehat{\boldsymbol{T}}_{\boldsymbol{cal1}}(\boldsymbol{w}, \boldsymbol{s}), \quad s \geq 0, \quad \text{(A.14a)}$$

$$\widehat{\boldsymbol{q}}^{"}_{\boldsymbol{cal2}}(-\boldsymbol{a}, \boldsymbol{s}) = \widehat{M}(k_1, k_2, \alpha_1, \alpha_2, a, b, w; s)\widehat{\boldsymbol{T}}_{\boldsymbol{cal2}}(\boldsymbol{b}, \boldsymbol{s}) - \widehat{N}(k_1, k_2, \alpha_1, \alpha_2, a, b, w; s)\widehat{\boldsymbol{T}}_{\boldsymbol{cal2}}(\boldsymbol{w}, \boldsymbol{s}), \quad s \geq 0. \quad \text{(A.14b)}$$

Solving for $\widehat{M}(k_1, k_2, \alpha_1, \alpha_2, a, b, w; s)$ and $\widehat{N}(k_1, k_2, \alpha_1, \alpha_2, a, b, w; s)$ by applying Cramer's Rule to Eqs. (A.14a,b) yields

$$\widehat{M}(k_1, k_2, \alpha_1, \alpha_2, a, b, w; s) = \frac{\hat{q}^{"}_{cal2}(-a, s)\hat{T}_{cal1}(w, s) - \hat{q}^{"}_{cal1}(-a, s)\hat{T}_{cal2}(w, s)}{\hat{T}_{cal2}(b, s)\hat{T}_{cal1}(w, s) - \hat{T}_{cal1}(b, s)\hat{T}_{cal2}(w, s)}, s \geq 0, \quad \text{(A.15a)}$$

$$\widehat{N}(k_1,k_2,\alpha_1,\alpha_2,a,b,w;s)=\frac{\hat{q}^{"}_{cal2}(-a,s)\hat{T}_{cal1}(b,s)-\hat{q}^{"}_{cal1}(-a,s)\hat{T}_{cal2}(b,s)}{\hat{T}_{cal2}(b,s)\hat{T}_{cal1}(w,s)-\hat{T}_{cal1}(b,s)\hat{T}_{cal2}(w,s)}\,,s\geq 0. \quad \text{(A.15b)}$$

Equations (A.15a,b) consist solely of experimentally obtained data streams. These data implicitly account for the physics of diffusion, thermo-physical properties and the probe positions. The specific domain of interest has been effectively 'calibrated' by two carefully designed experimental runs. The final step involves developing an expression for the unknown surface heat flux during a third 'real' run. The essential ingredients for this expression are the known in-depth temperature measurements during the 'real' run, alongwith the two calibration runs.

Rewriting Eq. (A.13a) for the real run case and substituting for $\widehat{M}(k_1,k_2,\alpha_1,\alpha_2,a,b,w;s)$ and $\widehat{N}(k_1,k_2,\alpha_1,\alpha_2,a,b,w;s)$ produces

$$\begin{aligned}\widehat{\boldsymbol{q}}^{"}_{\boldsymbol{run}}(-\boldsymbol{a},\boldsymbol{s})=&\frac{\hat{q}^{"}_{cal2}(-a,s)\hat{T}_{cal1}(w,s)-\hat{q}^{"}_{cal1}(-a,s)\hat{T}_{cal2}(w,s)}{\hat{T}_{cal2}(b,s)\hat{T}_{cal1}(w,s)-\hat{T}_{cal1}(b,s)\hat{T}_{cal2}(w,s)}\widehat{\boldsymbol{T}}_{\boldsymbol{run}}(\boldsymbol{b},\boldsymbol{s})\\&-\frac{\hat{q}^{"}_{cal2}(-a,s)\hat{T}_{cal1}(b,s)-\hat{q}^{"}_{cal1}(-a,s)\hat{T}_{cal2}(b,s)}{\hat{T}_{cal2}(b,s)\hat{T}_{cal1}(w,s)-\hat{T}_{cal1}(b,s)\hat{T}_{cal2}(w,s)}\widehat{\boldsymbol{T}}_{\boldsymbol{run}}(\boldsymbol{w},\boldsymbol{s}),s\geq 0. \quad \text{(A.16a)}\end{aligned}$$

We can easily identify the three-term convolution format by rearranging Eq. (A.16a) as

$$\begin{aligned}&\hat{q}^{"}_{run}(-a,s)\left[\hat{T}_{cal2}(b,s)\hat{T}_{cal1}(w,s)-\hat{T}_{cal1}(b,s)\hat{T}_{cal2}(w,s)\right]\\&=\hat{T}_{run}(b,s)\left[\hat{q}^{"}_{cal2}(-a,s)\hat{T}_{cal1}(w,s)-\hat{q}^{"}_{cal1}(-a,s)\hat{T}_{cal2}(w,s)\right]\\&-\hat{T}_{run}(w,s)\left[\hat{q}^{"}_{cal2}(-a,s)\hat{T}_{cal1}(b,s)-\hat{q}^{"}_{cal1}(-a,s)\hat{T}_{cal2}(b,s)\right],\qquad s\geq 0. \text{(A.16b)}\end{aligned}$$

We have now arrived at the final step of the frequency domain analysis. Equation (A.16b) can be readily inverted back to the time domain as per Eq. (A.3c), to produce the two-probe calibration integral equation for a two-layer geometry as

$$\int_{u=0}^{t} q''_{run}(-a,u) \int_{r=0}^{t-u} [T_{cal1}(w,r)T_{cal2}(b,t-u-r) - T_{cal2}(w,r)T_{cal1}(b,t-u-r)]\, drdu$$

$$= \int_{u=0}^{t} T_{run}(b,u) \int_{r=0}^{t-u} \left[q''_{cal2}(-a,r)T_{cal1}(w,t-u-r) - q''_{cal1}(-a,r)T_{cal2}(w,t-u-r)\right] drdu$$

$$- \int_{u=0}^{t} T_{run}(w,u) \int_{r=0}^{t-u} \left[q''_{cal2}(-a,r)T_{cal1}(b,t-u-r) - q''_{cal1}(-a,r)T_{cal2}(b,t-u-r)\right] drdu,$$

$$t \geq 0. \tag{A.17}$$

Equation (A.17) defaults to the conventional single-layer two-probe calibration integral equation, as per Eq. (2.22), when a = 0.

APPENDIX B. PROOF OF THE CLAIM: THE TWO-PROBE CALIBRATION KERNEL IS IDENTICALLY ZERO IF THE BACK-BOUNDARY CONDITIONS DURING THE TWO CALIBRATION RUNS ARE IDENTICAL

Appendix B presents the proof to the comment in Section 4.2.1 that claims, "*It has been proved in Appendix B that the two-probe calibration equation kernel $K(b,w,t-u)$, given by Eq. (2.23b), is identically equal to zero if the back-boundary conditions during the two calibration run stages are identical.*"

The expression for the two-probe calibration kernel $K(b,w,t-u)$ given by Eq. (2.23b) is now restated as

$$K(b,w,t) = \int_{u=0}^{t} [T_{cal1}(w,u)T_{cal2}(b,t-u) - T_{cal2}(w,u)T_{cal1}(b,t-u)]\,du, \tag{B.1}$$

where the kernel is now expressed as a function of t. As noted before, the kernel $K(b,w,t)$ is comprised of the calibration stage temperature responses. The proof is implicitly contained in the derivation of the one-probe calibration integral equation for a finite width domain on page 8 of Ref. [9]. Recall that the one-probe calibration integral equation is derived based on the constraint of similar back boundary conditions during the calibration and real 'unknown' run stages. The general solution to the governing heat equation of the finite-width domain subject to the trivial initial condition was given by Eq. (3.3c) on page 9 of Ref. [9], and is now restated as

$$\hat{T}(x,s) = C(s)\cosh\left(\sqrt{\frac{s}{\alpha}}x\right) + D(s)\sinh\left(\sqrt{\frac{s}{\alpha}}x\right), \qquad x \in [0.L], s \geq 0. \tag{B.2}$$

The unknown coefficients $C(s)$ and $D(s)$were determined with the help of the known boundary conditions $\hat{q}^{"}(0,s)$, $\hat{q}^{"}(L,s)$ and interior temperature measurement at the x=b location $\hat{T}(b,s)$ to obtain an input-output relationship shown as

$$\frac{\hat{q}^{"}(0,s)}{\hat{T}(b,s)} = \hat{N}(b,L,k,\alpha,h,s), \qquad s \geq 0. \tag{B.3}$$

As seen before, Eq. (B.3) presents a relationship between the desired boundary condition and interior temperature measurement in terms of a kernel function $\hat{N}(b,L,k,\alpha,h,s)$that remains constant for a fixed domain. Now, suppose a second in-depth temperature measurement

$\hat{T}(w,s)$ at x = w is made. Equation (B.3) can be written in terms of an input output relationship between $\hat{q}^{"}(0,s)$ and the resulting second temperature measurement $\hat{T}(w,s)$ at x=w, as

$$\frac{\hat{q}^{"}(0,s)}{\hat{T}(w,s)} = \hat{N}(w,L,k,\alpha,h,s), \qquad s \geq 0. \tag{B.4}$$

By relating Eq. (B.3) with Eq. (B.4), $\hat{q}^{"}(0,s)$ can be eliminated to form an expression that relates the two interior temperatures $\hat{T}(b,s)$ and $\hat{T}(w,s)$, by means of a new consolidated kernel function $\hat{N}^{*}(b,w,L,k,\alpha,h,s)$, as

$$\frac{\hat{T}(w,s)}{\hat{T}(b,s)} = \frac{\hat{N}(b,L,k,\alpha,h,s)}{\hat{N}(w,L,k,\alpha,h,s)} = \hat{N}^{*}(b,w,L,k,\alpha,h,s), \qquad s \geq 0. \tag{B.5}$$

Again, for a fixed domain and fixed back boundary condition (fixed heat transfer coefficient h of constant magnitude), the new kernel $\hat{N}^{*}(b,w,L,k,\alpha,h,s)$ remains constant. Accordingly, we can proceed to eliminate $\hat{N}^{*}(b,w,L,k,\alpha,h,s)$ via the process of performing two calibration runs to give

$$\frac{\hat{T}_{cal1}(w,s)}{\hat{T}_{cal1}(b,s)} = \frac{\hat{T}_{cal2}(w,s)}{\hat{T}_{cal2}(b,s)}, \qquad s \geq 0, \tag{B.6}$$

where the subscript 'cal1' refers to calibration run 1 and subscript 'cal2' denotes calibration run 2. Cross multiplying Eq (B.6) produces

$$\hat{T}_{cal1}(w,s)\hat{T}_{cal2}(b,s) = \hat{T}_{cal2}(w,s)\hat{T}_{cal1}(b,s), \qquad s \geq 0. \tag{B.7}$$

Inverting Eq. (B.7) to the time domain via the inverse Laplace convolution theorem yields

$$\int_{u=0}^{t} T_{cal1}(w,u)T_{cal2}(b,t-u)\,du = \int_{u=0}^{t} T_{cal2}(w,u)T_{cal1}(b,t-u)du\,, \qquad t \geq 0. \tag{B.8}$$

By re-arranging Eq. (B.8) we arrive at the desired result shown as

$$\int_{u=0}^{t} [T_{cal1}(w,u)T_{cal2}(b,t-u) - T_{cal2}(w,u)T_{cal1}(b,t-u)]\,du = 0, \qquad t \geq 0. \tag{B.9}$$

By comparing Eq. (B.9) with Eq. (B.1), it is now proved that the two-probe calibration kernel

$K(b, w, t)$is identically equal to zero if the back boundary conditions (fixed heat transfer coefficient h of constant magnitude) during the calibration runs are identical.

APPENDIX C. SANDWICH SETUP SPECIFICATIONS AND OTHER PERTINENT INFORMATION

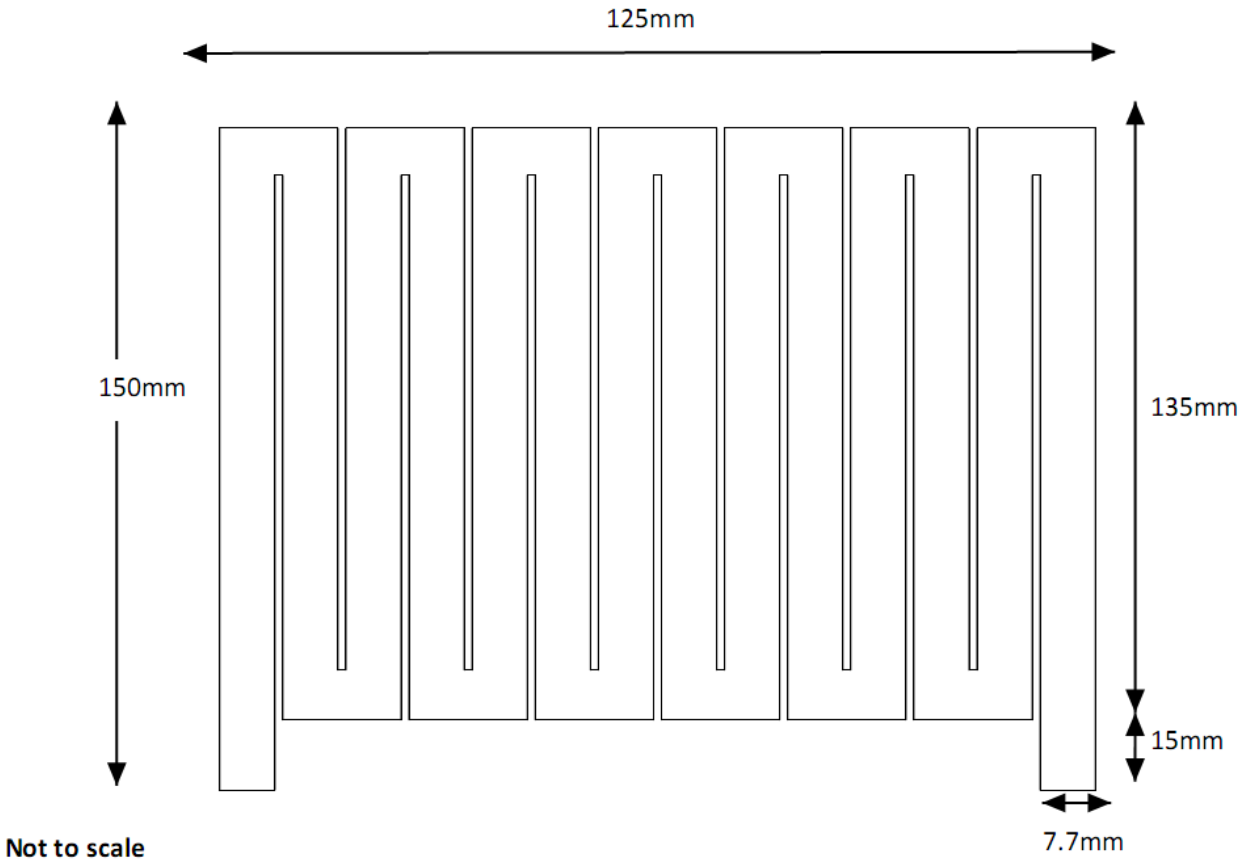

Figure C.1. Conceptual drawing of the custom nichrome heater by Dr. Majid Keyhani.

Table C.1. Thermo-physical properties of the materials used in sandwich setup

Property	Value
Stainless Steel	
Thermal Diffusivity (m^2/s)	3.95×10^{-6}
Thermal Conductivity (W/(mK))	14.9
Mica	
Thermal Conductivity (W/(mK))	0.71
Density (kg/m^3)	300
Specific Heat (J/(kgK))	0.5
Thermal Diffusivity (m^2/s)	4.73×10^{-3}
Alumina	
Thermal Conductivity (W/(mK))	26
Density (kg/m^3)	3750
Specific Heat (J/(kgK))	880
Thermal Diffusivity (m^2/s)	7.88×10^{-6}
Heater (nichrome)	
Thermal Diffusivity (m^2/s)	7.75×10^{-5}
Density (kg/m^3)	1420
Specific Heat (J/(kgK))	1.09
Heater Resistance (Ω)	2.123
Potting Compound (Cotronics 989F)	
Thermal Conductivity (W/(mK))	1.7

Table C.2. Measured thicknesses for the sandwich experiment.

Component	Thickness (mm)
Stainless steel slab	25.77
Mica	0.076
Alumina	0.38
Nichrome heater	0.125
Thermal paste	$\lesssim 0.03$

Table C.3. Depths and characteristics of thermocouple holes.

Sample	Slab 1				Slab 2	
Thermocouple Hole	S1B0	S1A1	S1A2	S1B3	S2A0	S2B2
Average Depth 'x' (mm)	12.951	6.568	6.586	12.899	6.474	12.893
Distance from Centerline 'y' (mm)	0.000	-6.689	12.322	18.600	0.000	-12.608
Resistance to Block (Ω)	2.3	5.9	1.1	1.3M	1.6	0.9

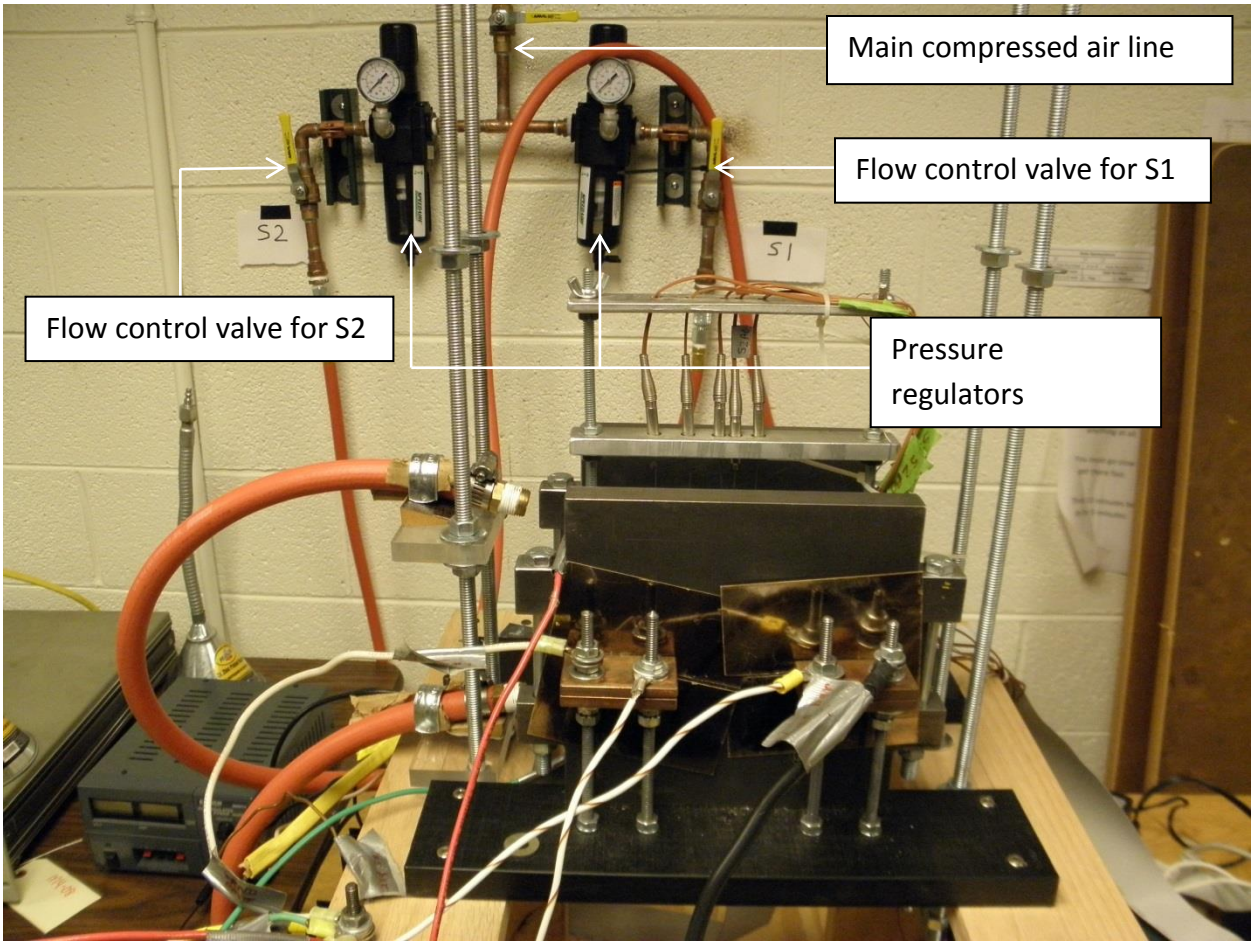

Figure C.2. Front view of the sandwich setup. The main compressed air line, pressure regulators, flow control valves and the flexible hosing are clearly seen.

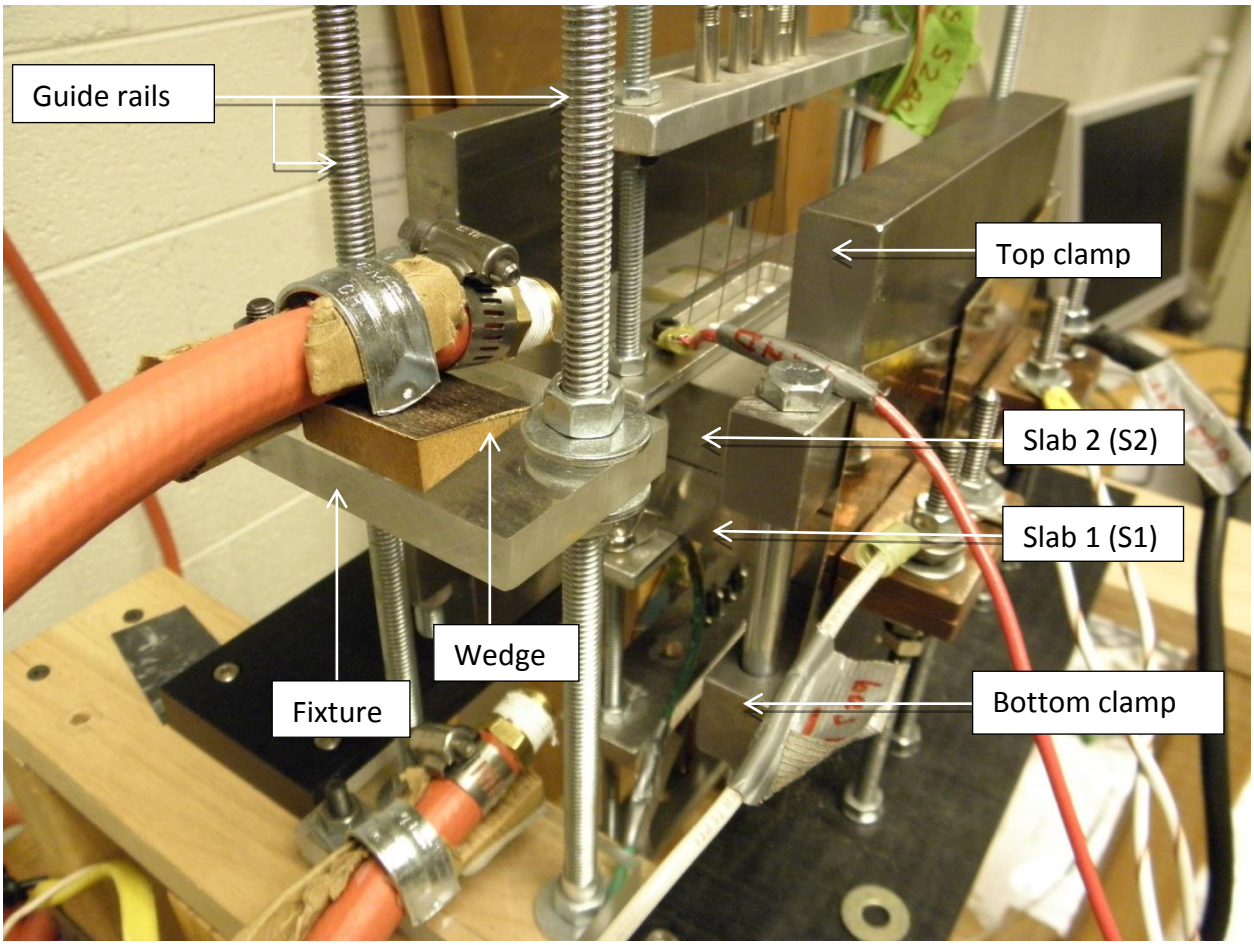

Figure C.3. Top-left skew view of the sandwich setup. The fixture that holds the free end of the hose is seen. The guide rails allow adjustable fixture height. The wedge is used to adjust the angle of air-flow. The two slabs are clamped tightly together to minimize contact resistance and facilitate thermal symmetry.

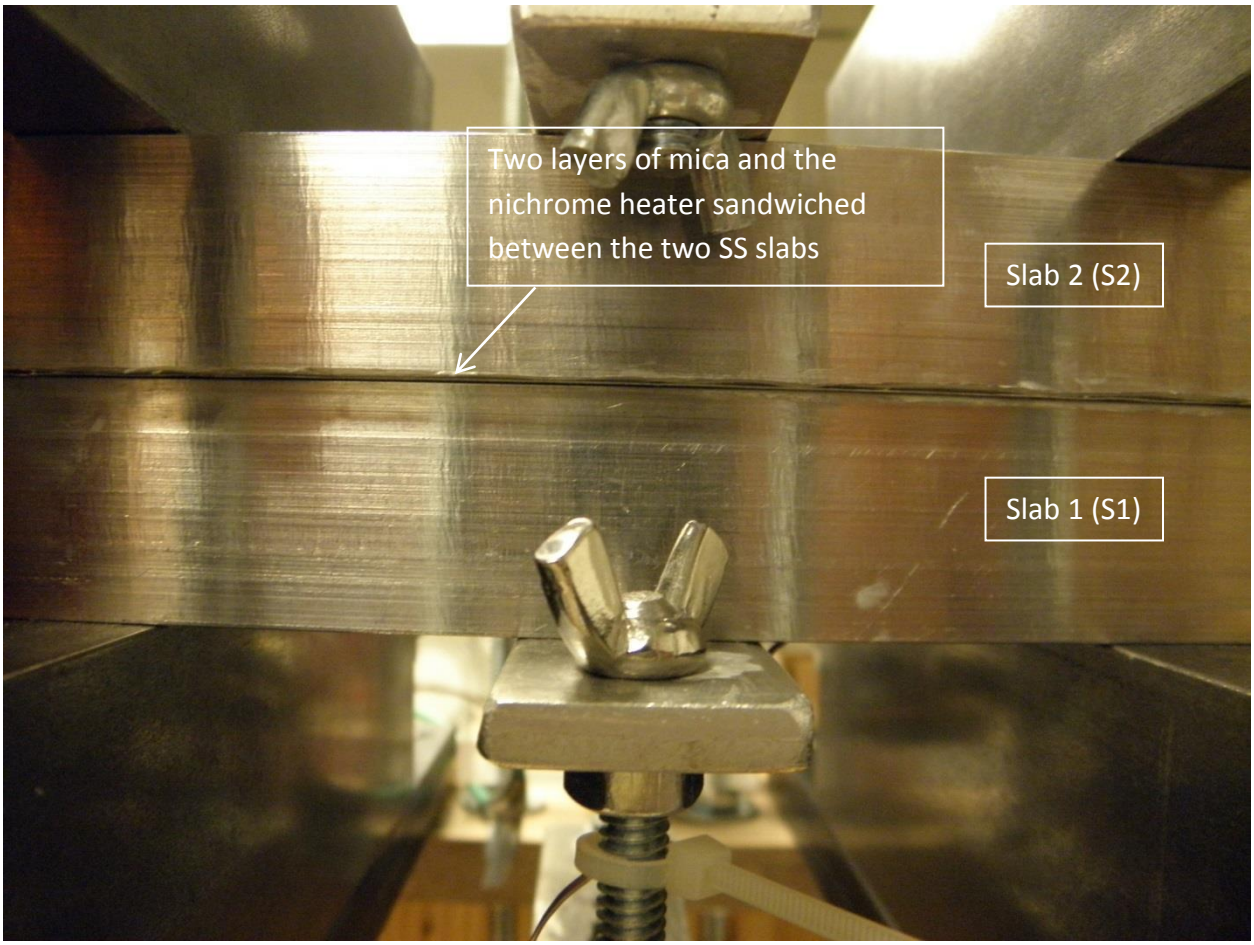

Figure C.4. Close-up view of the right side of the sandwich assembly.

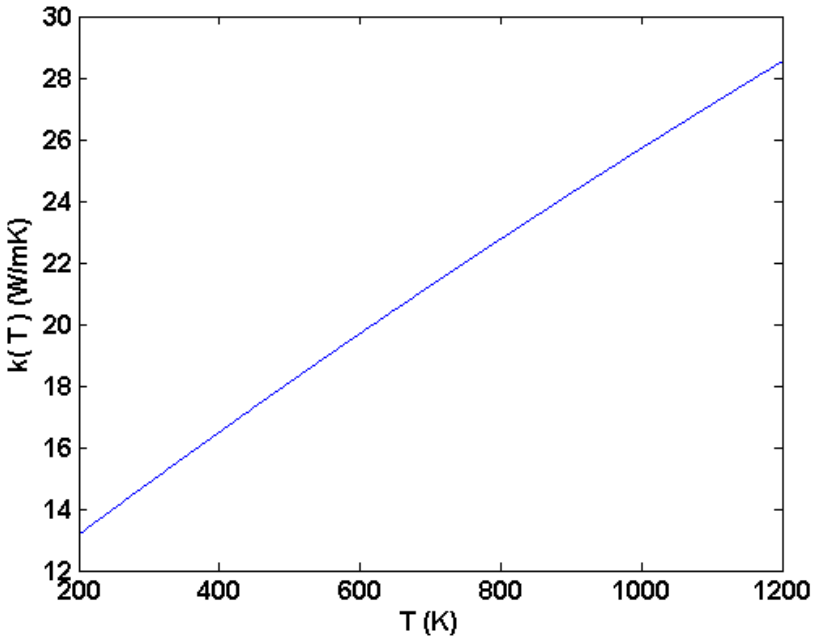

Figure C.5. Thermal conductivity k(T) of AISI 304 as a function of temperature [40].

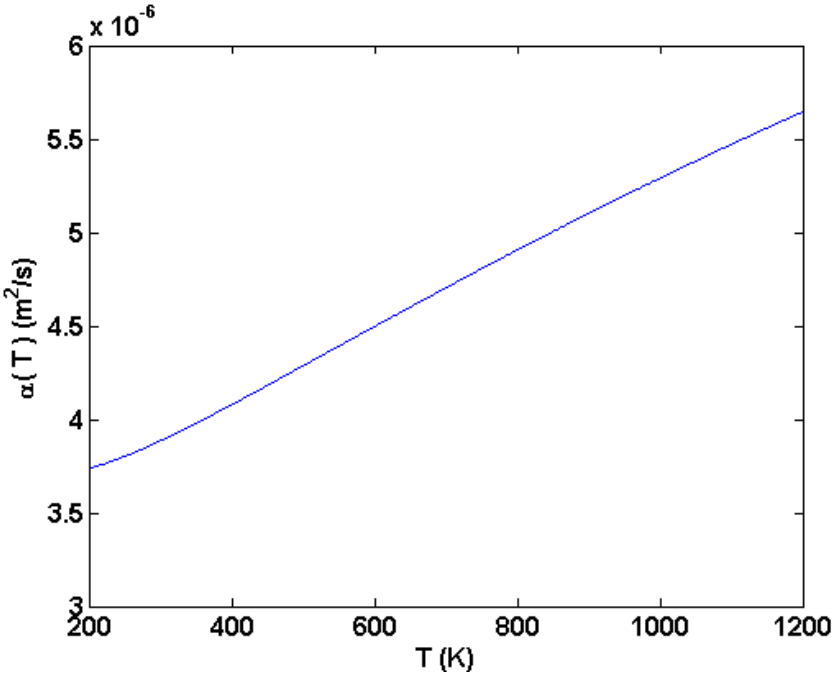

Figure C.6. Thermal diffusivity α(T) of AISI 304 as a function of temperature [40].

APPENDIX D. COMPARISON OF MEASURED DATA WITH FD MODEL

The comparison of the measured data with an FD model aims to serve two purposes. As mentioned in Chapter 4, the Mica Runs have been used for the single-layer analysis wherein the presence of the thin layer of mica is ignored. It remains to be verified if the heat flux generated by the heater and the actual net heat flux entering the stainless steel slabs are practically identical. This constitutes the first purpose for comparison. Additionally, to gain confidence in the measured thermocouple temperature data, a comparison between the thermocouple probe responses located at the center (S2A0 and S1B0) with the corresponding FD model generated temperatures at the same probe depths is made. This constitutes the second purpose of the FD model comparison.

Similar to the method mentioned in [7], a three-layer (half-heater, Mica (or Alumina) and stainless steel), one-dimensional finite difference (FD) model was used to solve the forward problem. The heater power was modeled as volumetric heat generation, with the power uniformly distributed over the volume of the heater. The effect of the thermal paste was neglected. Perfect contact was assumed between each layer. The measured transient heat flux was supplied to the FD model. The corresponding measured back-face temperature history (S2BF) was filtered using Frankel's Gaussian low-pass filter [27] using a cut-off frequency of 1 Hz. The filtered temperature was then supplied as the back boundary condition to the FD Model. This ensured accurate replication of the actual experimental heating conditions for effective comparison.

For the first purpose, the direct FD model calculated net heat flux incident on the stainless steel layer is compared with the measured heat flux. This comparison is made for two cases: 1) McRun1 (pulse heat flux) and 2) McRun3 (double-peak flight profile heat flux). The comparison of the McRun1 heat fluxes is shown in Figure D.1(a) and the McRun3 heat fluxes in Figure D.1(b). From Figure D.1 we can see very slight visible differences between the measured and FD Model heat fluxes for both McRun1 and McRun3. For McRun1, the mean error is less than 1% and the standard deviation of the error is about 2%. For the McRun3 case, the mean and standard deviation of the error are less than 1% of the peak heat flux value. Additionally the ratio of the first measured peak value to the first FD model peak value is 0.98 and for the second peak it is 0.99. Based on the relatively negligible differences obtained between the measured and FD Model heat fluxes for two different profiles, it can be safely inferred that the measured heat flux histories be used directly in the single-layer calibration analysis. The effect of the mica layer can be ignored.

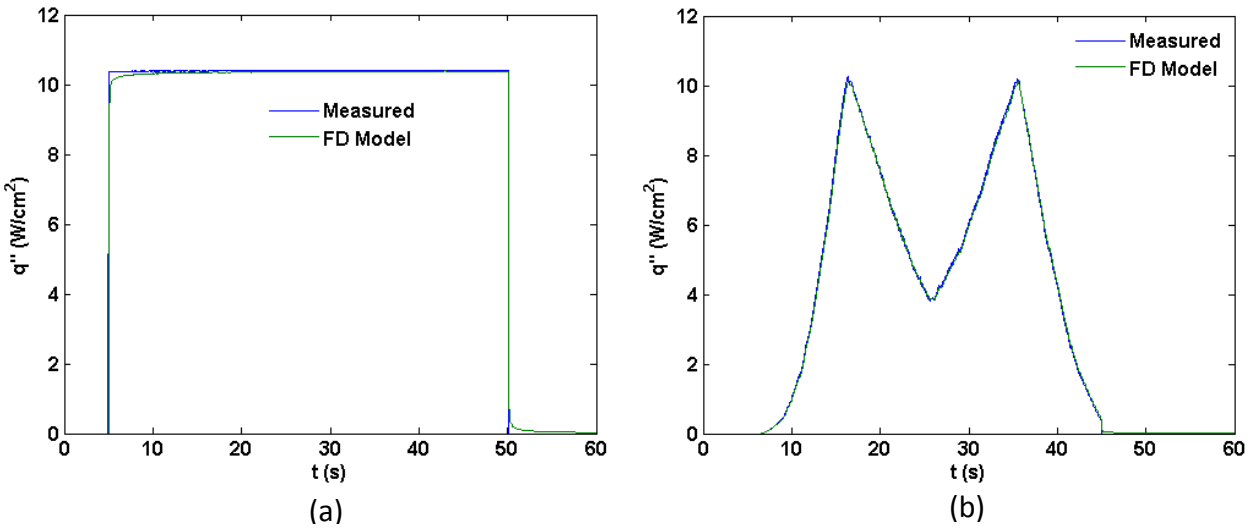

Figure D.1. Comparison of measured and FD Model heat flux histories for (a) McRun1 and (b) McRun3.

It is important to note that for the two-layer analysis, with Alumina as the electrical insulation layer, the two-layer calibration integral equation is derived such that the heat flux incident on the first (Alumina) layer is being sought. The presence of the additional Alumina layer is implicitly accounted for in the calibration run stage. Therefore, the measured heat flux incident on the first (Alumina) layer can be directly used in the two-layer calibration analysis.

For the second purpose, to gain confidence in the measured thermocouple temperature data, McRun1 and McRun4 (single-peak flight profile heat flux) will be selected as the representative Mica runs. For the Alumina runs, AlRun1 (pulse heat flux) and AlRun4 (double-peak flight profile heat flux) will be the selected candidates.

The comparisons of the measured and FD model generated temperatures for the Mica and Alumina cases are presented in Figures D.2-5. Figures D.2(a) to D.5(a) show the input heat fluxes to the FD model and Figures D.2(b) to D.5(b) show the raw and filtered back-face temperatures. As mentioned before, the filtered back-face temperature histories were supplied to the FD model as the back boundary condition. Figures D.2(c) to D.5(c) show the surface temperatures attained at the Mica (or Alumina) and the stainless steel surfaces. Finally, in Figures D.2(d) to D.5(d), the comparison of measured thermocouple temperature histories (S2A0 and S1B0) with the corresponding FD model generated temperatures is shown.

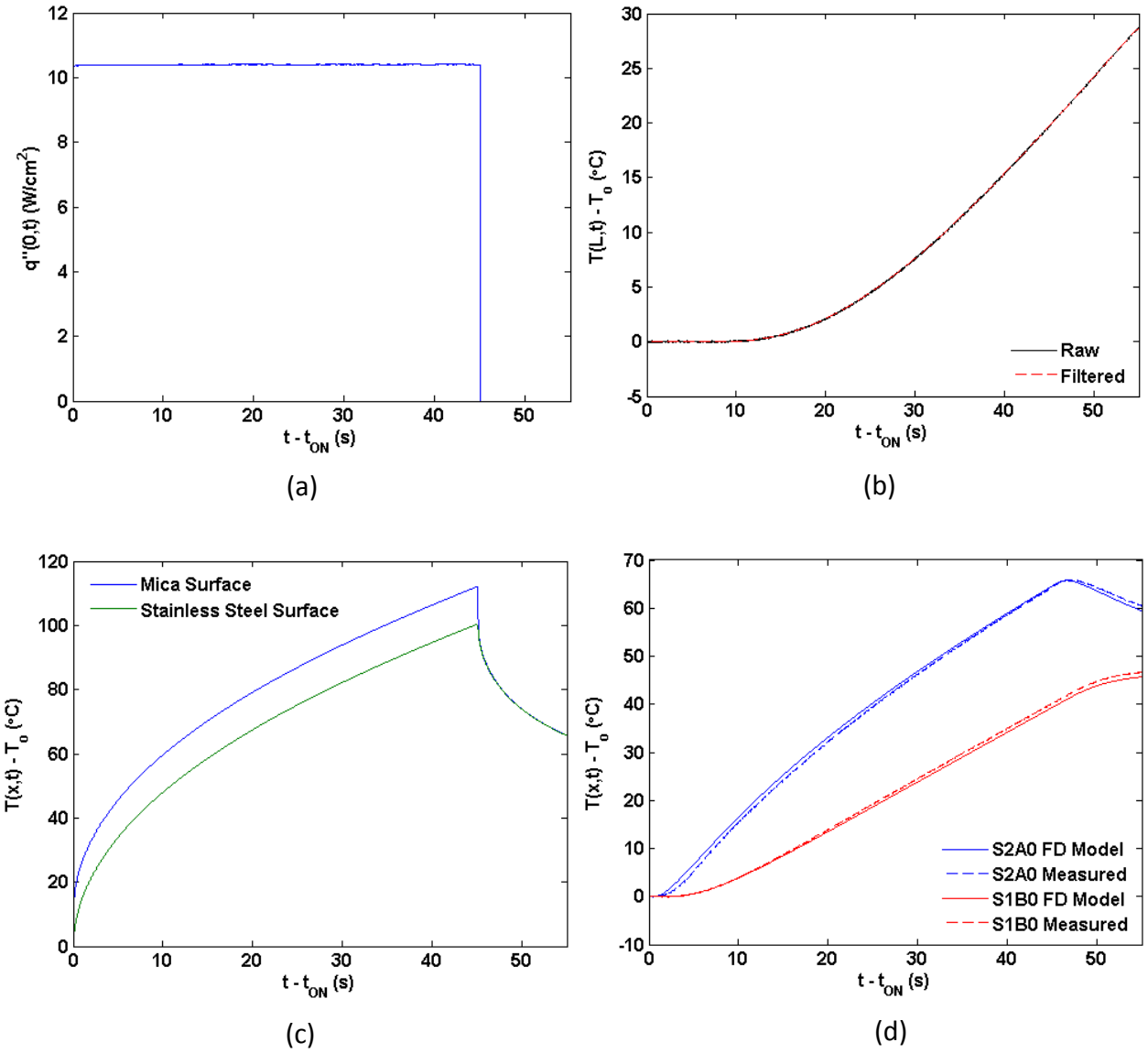

Figure D.2. McRun1 case – (a) heat flux input to the FD model (mean flux level = 10.41 W/cm^2), (b) raw and filtered back-face temperatures (cut-off frequency = 1 Hz), (c) FD model generated surface temperatures and (d) comparison of measured and FD model generated temperatures for the S2A0 (x = 6.47 mm) and S1B0 (x = 12.95 mm) locations. Initial temperature T_o = 22.1°C. Heat activation time t_{ON} = 5.01 s.

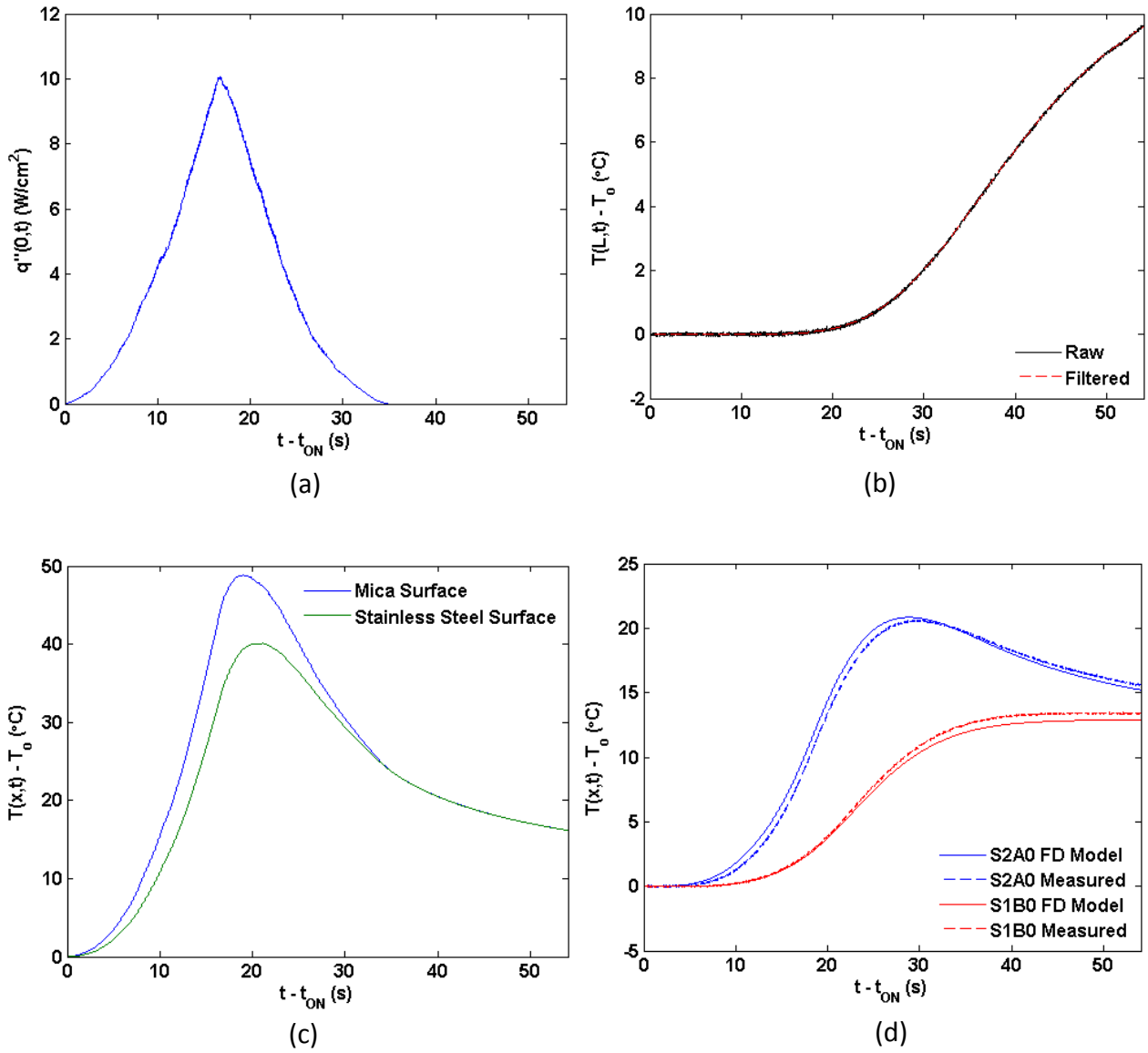

Figure D.3. McRun4 case – (a) heat flux input to the FD model (q''_{pk1}= 10.06 W/cm^2), (b) raw and filtered back-face temperatures (cut-off frequency = 1 Hz), (c) FD model generated surface temperatures and (d) comparison of measured and FD model generated temperatures for the S2A0 (x = 6.47 mm) and S1B0 (x = 12.95 mm) locations. Initial temperature T_o = 22.7°C. Heat activation time t_{ON} = 5.93 s.

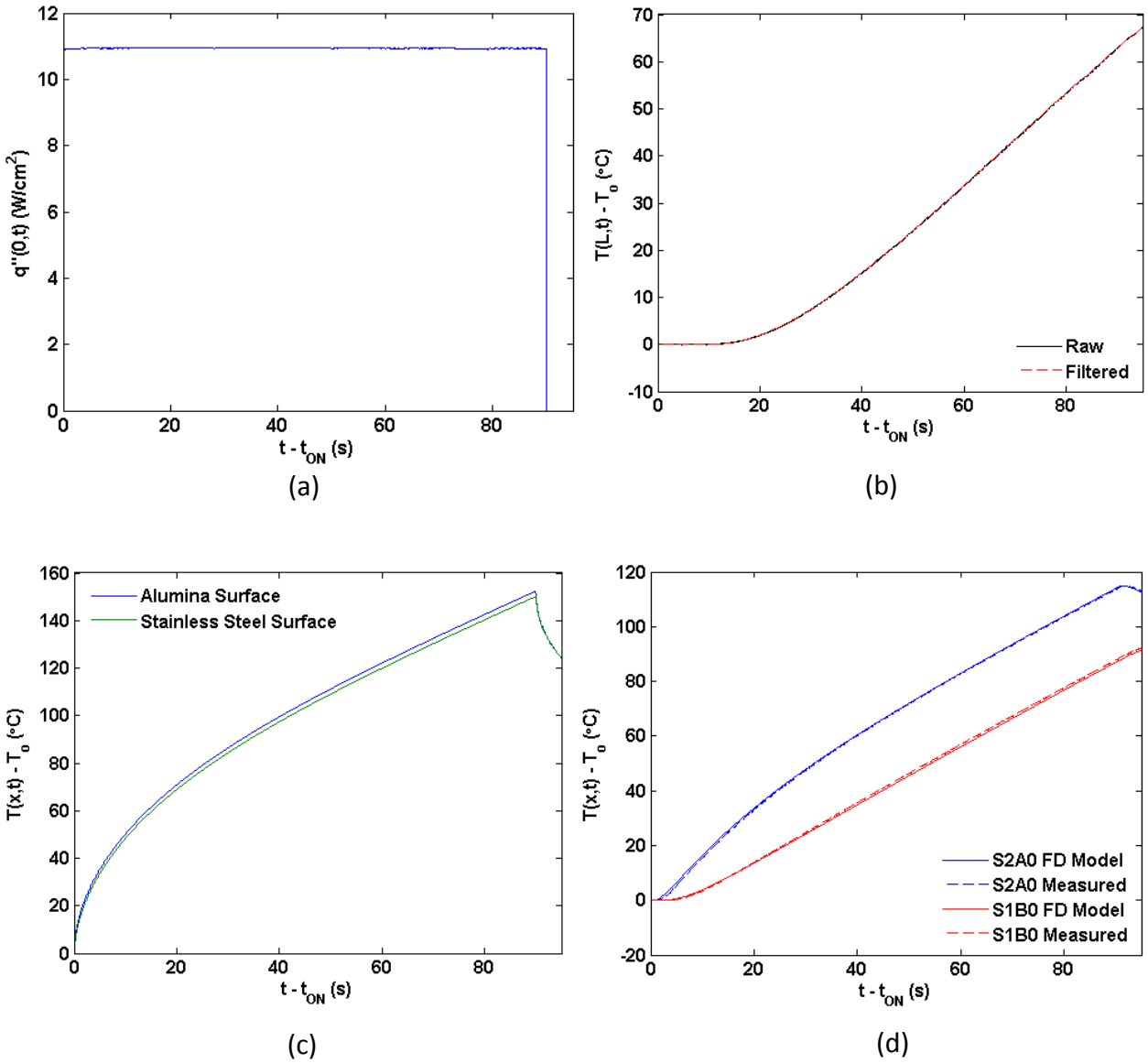

Figure D.4. AlRun1 case – (a) heat flux input to the FD model (mean flux level = 10.94 W/cm^2), (b) raw and filtered back-face temperatures (cut-off frequency = 1 Hz), (c) FD model generated surface temperatures and (d) comparison of measured and FD model generated temperatures for the S2A0 (x = 6.47 mm) and S1B0 (x = 12.95 mm) locations. Initial temperature T_o = 22.4°C. Heat activation time t_{ON} = 5.03 s.

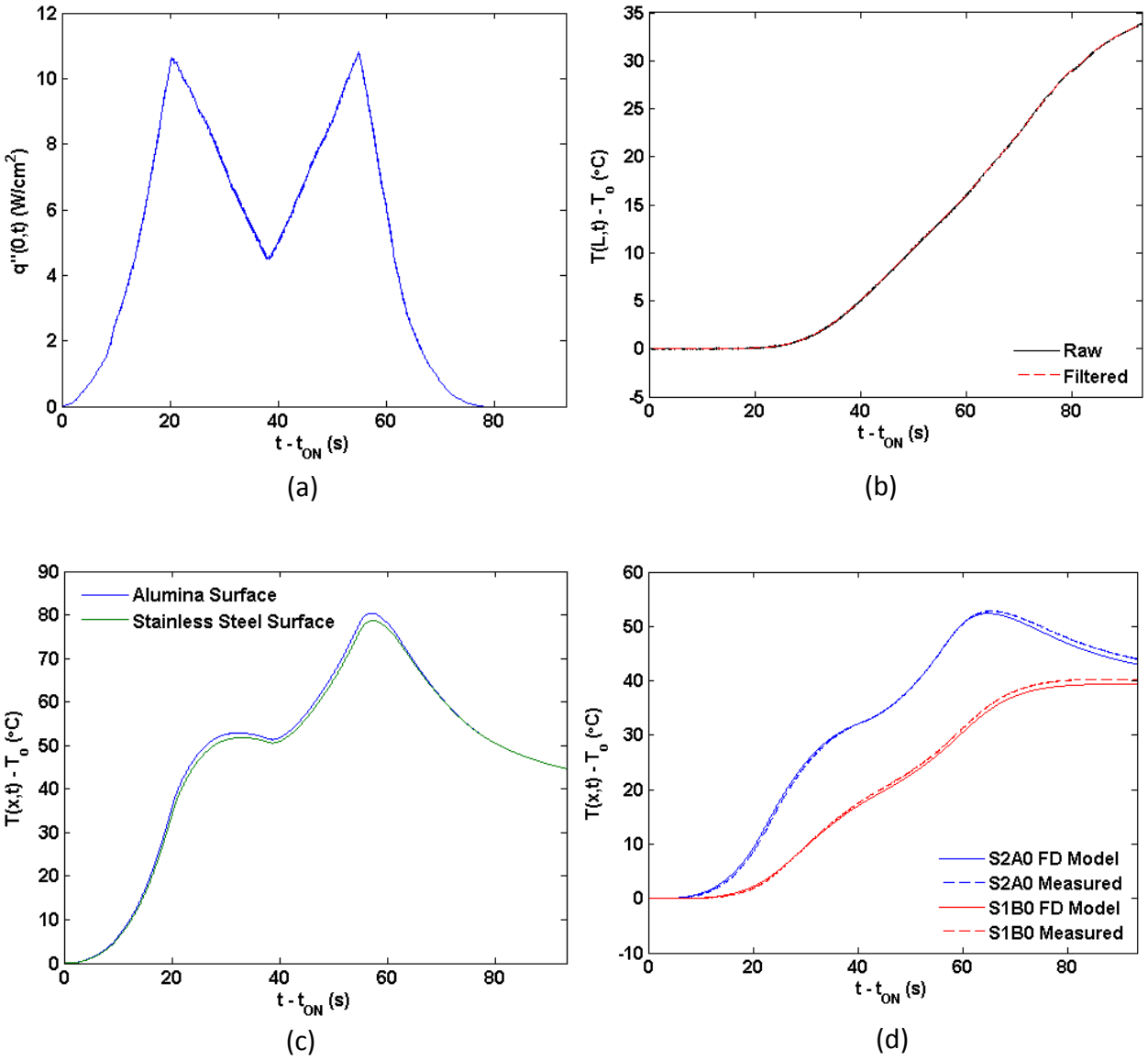

Figure D.5. AlRun4 case – (a) heat flux input to the FD model (q''_{pk1}= 10.62 W/cm^2 and q''_{pk2}= 10.8 W/cm^2), (b) raw and filtered back-face temperatures (cut-off frequency = 1 Hz), (c) FD model generated surface temperatures and (d) comparison of measured and FD model generated temperatures for the S2A0 (x = 6.47 mm) and S1B0 (x = 12.95 mm) locations. Initial temperature T_o = 22.4°C. Heat activation time t_{ON} = 6.7 s.

From Figures D.2(d) and D.4(d), for the pulse heat flux cases, remarkable closeness between the FD model and measured temperatures can be observed. As expected, a slight delay in the measured thermocouple temperatures at the S2A0 location during take-off can be seen. The measured temperatures at the S1B0 location are seen to be slightly higher than the FD model generated temperatures. This can be attributed to the uncertainty in determining the actual depth of the installed thermocouple. It can be possible that the actual depth is lesser than the measured value (x = 12.95 mm), leading to a higher temperature response. From Figures D.3(d) and D.5(d), for the flight profile heat flux cases, the delay in take-off and attenuation of the measured thermocouple temperatures at the S2A0 location is more pronounced. Also interesting to note is the measured temperatures are higher than the FD model generated temperatures during the cooling period. This is consistent with the first order thermocouple model [6] wherein the negative slope of the thermocouple temperature results in a negative valued derivative term which then brings down the measured temperature to the positional (FD model) temperature. For the S1B0 location, similar behavior to the pulse heat flux cases is observed.

Overall, the measured thermocouple temperatures are in excellent agreement with the FD model generated temperatures despite the numerous uncertainties in determining the actual probe depths, thermo-physical properties and heat loss from the side walls of the test slabs. The measured data can hence be inferred to be of a high quality and standard.

VITA

Abhay Sanjeev Pande was born in Pune, Maharashtra, India on May 14, 1987. He graduated from the Abhinava Vidyalaya English Medium High School in May, 2003. He pursued his junior college level education in the field of science at the Abasaheb Garware College of Science and Commerce and graduated in May, 2005. He chose the discipline of engineering for his undergraduate studies and graduated with a Bachelor of Engineering Degree in Mechanical Engineering from The University of Pune in June, 2009. During his time at University of Pune, he participated in the inaugural Baja SAE INDIA national event, involving the design, fabrication and racing of All Terrain Vehicles (ATVs). His college team won the second prize for innovation for their 'Push-rod Actuated Adjustable Suspension System'. He continued his education in engineering by pursuing a Master of Science degree at the University of Tennessee, Knoxville. While in grad-school, he worked under the guidance of Prof. Majid Keyhani and Prof. Jay Frankel in the field of inverse heat conduction. His research focused on the novel physics-based calibration methodology of solving the inverse heat conduction problem. He received his Master of Science degree in mechanical engineering in December, 2013.